The Dissertation Committee for Harsha Vardhana Padullaparti
certifies that this is the approved version of the following dissertation:

Edge-of-Grid Voltage Control in Distribution Networks

Committee:

Surya Santoso, Supervisor

Ross Baldick

Gary Hallock

Brian Korgel

Evdokia Nikolova

Edge-of-Grid Voltage Control in Distribution Networks

by

Harsha Vardhana Padullaparti

DISSERTATION
Presented to the Faculty of the Graduate School of
The University of Texas at Austin
in Partial Fulfillment
of the Requirements
for the Degree of

DOCTOR OF PHILOSOPHY

THE UNIVERSITY OF TEXAS AT AUSTIN
August 2018

Dedicated to my parents and teachers.

Acknowledgments

With great pleasure, I would like to thank everyone who have helped me in completion of this work. First and foremost, I wish to express my deep gratitude towards my supervisor Dr. Surya Santoso for his invaluable guidance, support, and providing me a great platform to grow academically. My sincere thanks are due to all my dissertation committee members Dr. Ross Baldick, Dr. Gary Hallock, Dr. Brian Korgel, and Dr. Evdokia Nikolova, for agreeing to serve on my committee and providing valuable inputs.

I am grateful to Electric Power Research Institute for providing the data and models of utility distribution circuits which are critical in carrying out my research. I wish to thank Center for Next Generation Photovoltaics for offering me the opportunity to disseminate my results, feedback on my progress, and support.

I have had a great opportunity to collaborate with my colleagues Dr. Min Lwin, Dr. Miguel Hernandez, Dr. Pisitpol, Dr. Anamika Dubey, Quan Nguyen, Suma Jothibasu, Kyungwoo Min, and Naveen Ganta. I learned a lot from them. I would like to thank Nandini for her encouragement.

Finally, I wish to thank my parents for their unconditional love and support. Special thanks to my Annayya (elder brother) for his mentorship.

Edge-of-Grid Voltage Control in Distribution Networks

Publication No. ____________________

Harsha Vardhana Padullaparti, Ph.D.
The University of Texas at Austin, 2018

Supervisor: Surya Santoso

As the electric power supply systems are undergoing major changes with the integration of renewables, the issues related to voltage regulation and system protection are arising. In this scenario, advanced voltage regulation technologies that provide voltage control at the grid-edge, that is at the low-voltage secondary side of the distribution circuit, have emerged as a potential solution to address the shortcomings of traditional voltage control practices in distribution systems. In this work, these technologies are modeled and algorithms are developed to strategically deploy them, tune their control parameters, and evaluate their voltage regulation performance. A two-stage optimization framework is proposed for optimal placement and real-time control of the low-voltage static var compensators to minimize the energy losses while maintaining the voltage regulation. Integration of high levels of distributed generation such as photovoltaic (PV) systems impacts the voltage regulation by causing steady-state voltage variations and transient voltage fluctuations. This work further develops a procedure to tune the control parameters of PV smart inverters to mitigate these voltage issues. Furthermore, the PV penetration levels in a distribution network can be increased without creating voltage problems by dynamic controlled reactive power absorption at several strategic buses. This concept is modeled and demonstrated in this work. Furthermore, the high levels of PV generation can interfere with the overcurrent protection schemes prevalent in distribution networks. An analytical approach is proposed in this work to estimate the distribution feeder PV accommodation limits with respect to overcurrent protection issues as the impact criteria, without needing to simulate numerous PV screening scenarios to assess the impact.

Table of Contents

List of Tables

List of Figures

Chapter 1

Introduction

Traditionally, distribution feeders are radial in nature with the distribution substation as the only source supplying the passive loads connected across the network. The conventional voltage regulation and system protection practices in distribution grids rely heavily on the unidirectional power flow assumption that is valid for radial passive distribution grids. With the integration of various distributed energy resources (DER) in the modern grids, there are multiple sources of power causing bidirectional power flows, leading to both voltage regulation and protection problems. This chapter presents the motivation and objectives of the research on the development of algorithms to address the voltage regulation and protection issues in modern grids. Further, the specific research approaches taken to address the objectives along with the technical contributions are also outlined.

1.1 Background and Motivation

As electric power delivery systems are undergoing remarkable changes lately in terms of introduction of new sources, loads and operation modes, system planners are experiencing many challenges. The integration of DER including photovoltaics (PV), energy storage systems (ESS), and electric vehicles cause issues related to voltage regulation, overloads, and protection. Detailed studies conducted on numerous distribution feeders with millions of unique scenarios to assess the impact of PV generation have concluded that the voltage and protection related issues are the most affected out of many issues examined [2]. Therefore, new methods and algorithms are needed to enhance the voltage regulation and system protection in the modern electric grids.

Voltage regulation is one of the fundamental responsibilities of a distribution utility. Voltage regulation refers to maintaining acceptable voltages at all points along the distribution feeder including secondary service circuit under all loading conditions. Most of the utilities in the U.S. follow ANSI voltage standards [3] for maintaining acceptable levels of service voltages. The service voltage is the point where the electrical systems of the supplier and the user are interconnected which is normally at the meter. According to ANSI standard, the service voltages should be within ±5% of their nominal voltage level which translates to 0.95 to 1.05 per unit (pu) voltage. Distribution utilities rely primarily on traditional voltage regulation equipment such as load tap changer (LTC), mid-line voltage regulators, and capacitors for voltage regulation. These devices are installed on the primary-side of the distribution circuit to perform voltage regulation by regulator tap changes and capacitor switching operations. However, the shortcomings of these equipment such as their sparse locations on the primary, limited number of operations per day due to their mechanical nature, and lack of direct control over secondary side voltages are significantly limiting their voltage regulation performance, especially when the voltage dynamics are introduced by the high penetration levels of DER. Furthermore, the advanced metering infrastructure (AMI) data indicates that the voltage drop across service transformers, typically assumed as minimal, can be of significant portion of the ANSI band depending on the loading condition [4]. Thus, despite the primary-side voltages as seen by the controllers of the voltage regulators and capacitor banks are well within limits, the secondary side network voltages may fall outside the ANSI limits.

The limitations of traditional voltage regulation practices have led to the emergence of many advanced voltage control technologies connected at the grid-edge [5]. Grid-edge refers to the secondary side of the distribution circuit. Universal power flow controller [6] and static var compensator [7] are the examples of such technologies commercially available today. These technologies can be collectively referred to as edge-of-grid voltage control devices.

In Fig. 1.1, the primary and secondary distribution circuits along with various traditional and grid-edge voltage control equipment available for voltage regulation are depicted. Primary distribution circuit refers to the medium-voltage distribution network with voltages ranging from 600 V up to 35 kV [8]. Service transformers step down the primary distribution voltage to service voltage level (commonly 120/240 V) in the low-voltage secondary circuit [8]. The customer loads are connected to the secondary network through service lines. The low-voltage distribution network after the secondary of the service transformer is a secondary circuit. It can also be referred to as grid-edge as it is closest to the end-use customers of the electric power. The means for the grid-edge voltage control considered in this work are edge-of-grid devices, i.e., UPFC, SVC devices, and the PV smart inverters.

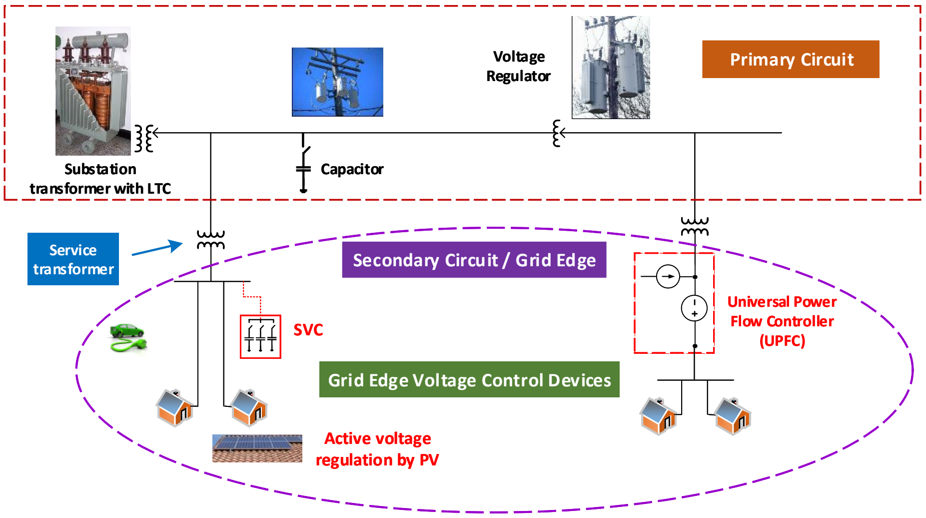

Figure 1.1: Voltage regulation equipment in a distribution circuit.

The amount of PV a distribution feeder can accommodate without violating the nominal system operating conditions is the feeder's PV hosting capacity or feeder's PV accommodation limit [9]. In case of ESS integration, it can be referred to as ESS accommodation limit of the circuit. Approaches for determination of a feeder's PV accommodation limits with system protection related issues as impact criteria using circuit simulations are reported in [10,11]. In recent years, there are several changes to the regulations for grid interconnection of distributed generation (DG). While previous regulations mandated disconnection of DG during abnormal system conditions, many new regulations require the DG to remain connected during the faults, referred to as ‘low voltage ride through’ (LVRT) or ‘fault ride through’ (FRT). Similar to DG, as part of grid support functions, the ESS also offers LVRT functionality [12]. Since protection studies are performed considering the worst case situation, it is reasonable to consider that the large-scale PV and ESS remain connected in the system during the fault conditions and assess the impact of their steady state current injection into the distribution network [11]. With the growing concerns to integrate higher amounts of PV into distribution systems along with possible adverse impact mitigating measures such as installing ESS, suitable methods are required for estimating the sizes of large-scale PV and ESS a feeder can accommodate without creating protection problems.

1.2 Objective

The objective of the research presented in this dissertation is to develop methods and algorithms to improve the voltage regulation at the grid-edge and enhance the system protection to help system planners to operate grids efficiently and reliably. It is described in further detail as below:

1.2.1 Voltage Regulation through Grid-Edge Voltage Control

The research objective focuses on investigating the feeder level benefits of grid-edge voltage control via low-voltage reactive power control devices and PV smart inverters. As these devices are relatively new, software models emulating their functionality for some of the devices are not available. The device models are developed and their operational characteristics are studied. The approaches for deployment of the edge-of-grid devices in real-world distribution circuits to accomplish various objectives are proposed and their effectiveness is validated through circuit simulations. Specifically, the objectives investigated are voltage regulation, voltage smoothing, minimizing energy losses, and increasing PV hosting capacity of distribution circuits. The existing literature lacks in providing inputs on selecting the locations for deployment of edge-of-grid devices that provide dynamic reactive power injection using local voltage measurements. Various algorithms are proposed to determine the effective locations for installing these devices in large-scale distribution networks. The PV smart inverters also provide a control handle to improve voltage regulation in distribution circuits. As the PV smart inverters are very versatile, numerous control settings are possible to implement on a PV smart inverter and the determination of appropriate control settings is a complex process. The goal in this work is to simplify of PV smart inverter control setting tuning process to achieve both voltage regulation and voltage smoothing. Furthermore, an edge-of-grid device namely low-voltage distribution static compensator (LV-DSTATCOM) is proposed to increase the PV penetration levels in distribution circuits. The proposed device functions similar to the other edge-of-grid devices available in the market but has the ability to absorb reactive power to limit the rising bus voltages due to high levels of PV generation.

1.2.2 Feeder Accommodation Limits based on Protection Criteria

The research objective focuses on development of a simplified process for estimating the PV and ESS accommodation limits of distribution feeders with protection issues as impact criteria. Before integrating DER such as PV or ESS, system studies need to be performed to assess associated impacts on the existing overcurrent protection schemes [13]. The impact is highly dependent on the type of DG being integrated. Influence of rotating machine-based DG (RBDG) such as synchronous machine-based DG and induction machine-based DG on feeder overcurrent protection schemes is reported in [14, 15]. As opposed to the RBDG, inverter-interfaced distributed generation (IIDG) such as PV systems do not make much fault current contribution. While the fault current contribution of PV systems can vary from 1.1 to 2.5 times the inverter rated current depending on the type of inverter, the rule of thumb in the industry for system studies is 2 times the inverter rated current [16, 17]. Such low PV fault currents may not interfere with the overcurrent protection schemes in case of small-scale PV systems with low penetration level. However, large-scale PV installations can inject high fault currents into the system and can lead to protection problems [18, 19]. The existing simulation-based approaches pose scalability challenges in terms of power flow solution convergence, complexity of analysis and visualization of results considering large number of protection devices in the circuit, huge time requirement to study all possible combinations of PV sizes, and fault locations [11]. Thus, the work aims at development of a scalable analysis-based method to conservatively estimate large-scale PV and

ESS accommodation limits of a distribution feeder without causing protection issues while providing the insights into parameters influencing these issues.

1.3 Research Approach and Contributions

The specific research approaches taken to address the above objectives are organized into three areas. The first and second approaches address the objective of grid-edge voltage control to achieve feeder level benefits and the third approach addresses the objective of estimation of feeder PV/ESS hosting capacity analytically using fault analysis. Each approach and the associated contributions are described below.

1.3.1 Grid-Edge Voltage Control using Distributed Reactive Power Injections

Voltage regulation in distribution circuits through primary side control assets such as LTC, voltage regulators, and fixed/switched capacitor banks do not provide fine and precise control over the load voltages. Considering the load connectivity on the low-voltage secondary circuit, grid-edge voltage control technologies installed on the secondary circuit to offer direct and precise load voltage control have emerged lately. Some of these devices, referred to as low-voltage static var compensators (LV-SVCs) dynamically inject reactive power into the distribution system based on their terminal voltage and a voltage setpoint by switching in required number of capacitor stages. They cannot absorb the reactive power. A comprehensive review of edge-of-grid devices is provided in [5]. With the availability of edge-of-grid devices, the distribution utilities face a new challenge in determining the required number of edge-of-grid devices and optimal locations to install them. An iterative placement algorithm based on undervoltage area criterion is proposed [20] to select effective locations to install the LV-SVCs operating on local voltage-based autonomous controllers with voltage regulation as the primary objective.

The reactive power supply from the edge-of-grid devices can improve the power factor, thereby reducing the active power losses. Additionally, the voltage control through these devices can help lower the switching operation of traditional primary voltage regulation equipment to improve their service life. Considering these abilities, a multi-objective optimization approach is proposed in [21] to determine the LV-SVC locations to minimize the energy losses and switching operations of the traditional voltage regulation equipment.

The edge-of-grid voltage control technologies offer two-way communication capabilities [22, 23] for data exchange and receiving control commands from a central location which is typically the substation. Such communication capabilities, in the presence of load data availability with advanced metering infrastructure (AMI) [24–26], can be utilized to apply a centralized control to adjust the reactive power outputs of LV-SVCs in real-time to optimize the performance the distribution network. Therefore, a two-stage optimization framework is proposed in [27] for placement and real-time control of the LV-SVCs to minimize the active power losses while maintaining voltage regulation. The number, locations, and the optimal real-time reactive power injections from the LV-SVCs are determined from three-phase unbalanced AC optimal power flow (ACOPF) results. The ACOPF is formulated as a multi-objective optimization with operating constraints written in rectangular coordinates. The resulting nonlinear nonconvex problem is solved using the predictor-corrector primal-dual interior point method (PCPDIPM).

The key contributions of the research carried out in this area are the demonstration of the effectiveness of edge-of-grid devices in voltage regulation [28] and development of algorithms for optimal placement and control [5, 20, 21, 27] of these technologies to improve voltage regulation, lower switching operations, and minimize energy losses in the utility distribution circuits.

1.3.2 Grid-Edge Voltage Control using Dynamic Reactive Power Absorption

The PV smart inverters form another control handle at the grid-edge to regulate the system voltages. Unlike the LV-SVCs which can only inject but not absorb the reactive power, the PV smart inverters can do both dynamically. As the present standards permit active voltage regulation by PV smart inverters [29], it is necessary to utilize them for this purpose. However, the determination of appropriate PV smart inverter settings is a complex process as numerous settings are possible to implement on a smart inverter and the feeder response to a given setting depends upon a wide variety of parameters such as the feeder characteristics, loading condition, PV size, and PV location [30]. As part of the work in this research area, a procedure to tune the PV smart inverter settings by grouping the PVs in the feeder neighborhoods experiencing undervoltages is proposed in [31] for voltage regulation. The performance of the tuned PV smart inverter settings is compared to that of the settings recommended in literature [30, 32] using voltage range and voltage variability indexes. The results show that, implementation of the tuned settings using the proposed method is very effective to mitigate steady-stage voltage variations and voltage fluctuations due to variable power injections of PV.

Voltage rise is one of the major concerns limiting the photovoltaic (PV) hosting capacity or the maximum amount of PV generation that a distribution circuit can accommodate. Motivated by the applications of edge-of-grid devices, another device referred to as low-voltage distribution static compensator (LV-DSTATCOM) is proposed in this work [33] to increase the PV hosting capacity of distribution circuits by mitigating the voltage rise. The LV-DSTATCOM is a shunt-connected device that can inject or absorb reactive power as needed to regulate the voltage at its terminals. The controlled reactive power absorption can help in reducing the overvoltages on the secondary-wire due to high levels of PV generation. Although the PV smart inverters can also help regulate the secondary circuit voltages through reactive power control, the utility typically does not have control over the PV locations and the PV reactive power output is limited by its active power generation. The study results show that, installation of a few LV-DSTATCOMs at suitable locations can significantly increase the PV hosting capacity of distribution circuits.

1.3.3 Estimation of Feeder PV/ESS Hosting Capacity based on Protection Criteria

The integration of high levels of DER such as PV and ESS can create protection issues due to their fault current contributions. As such, detailed protection studies need to be performed before integrating the DER. The protection studies require development of detailed distribution system models using distribution system simulation tools [34]. Then the developed model is validated by comparing power flow results with actual field measurements. Once the validated model is available, simulation studies are performed to assess the impact of DER integration on protection schemes with large number of scenarios. However, this process requires considerable time and effort [35]. Furthermore, the existing simulation-based approaches pose scalability challenges in terms of power flow solution convergence, complexity of analysis and visualization of results considering large number of protection devices in the circuit, huge time requirement to study all possible combinations of DER sizes, and fault locations [11]. In this work [36], a scalable analysis-based method to conservatively estimate large-scale PV and ESS accommodation limits of a distribution feeder without causing relay insensitivity and sympathetic tripping problems is proposed. The proposed approach simplifies the estimation process with reasonable approximations under conservative settings while providing the insights into the parameters influencing these protection issues. Thus, detailed protection studies are not needed when the PV and ESS penetration levels are below the limits determined by the proposed approach.

Chapter 2

Grid-Edge Voltage Control in Utility Distribution Circuits

The edge-of-grid voltage control technologies augment the traditional primary side voltage controls in improving the voltage regulation in distribution circuits. As some of these devices are under deployment in the field, the utilities face the challenge of selecting the effective locations to install them in the distribution circuits. Several methods have been reported in literature to determine the effective locations to deploy traditional voltage regulation equipment such as capacitor banks on the primary system [37–39]. However, such techniques are not suitable for selecting the effective locations for the edge-of-grid voltage control devices in large distribution circuits as the operational characteristics of these devices are very different compared to the traditional voltage regulation equipment. [1]In this chapter, the specifications, characteristics, and modeling of two edge-of-grid devices namely universal power flow

---

[1] Parts of this chapter appear in the published paper, 'H. V. Padullaparti, P. Chirapongsananurak, and S. Santoso,"Edge-of-Grid Voltage Control: Device Modeling, Strategic Placement, and Application Considerations," *IEEE Power and Energy Technology Systems Journal*, vol. 4, no. 4, pp. 106-114, Dec. 2017' and the accepted book chapter, 'H. V. Padullaparti, P. Chirapongsananurak, and S. Santoso, "Grid-Edge Voltage Control in Utility Distribution Circuits," *Advanced Power Engineering*, CRC Press'. The author of this dissertation contributed sections I through V in the paper and all the sections except IV in the book chapter as first author.

controller (UPFC) and static var compensator (SVC) are discussed in detail. Then an iterative placement algorithm based on undervoltage area criterion is proposed to determine the effective locations to install these devices to remove low voltage violations in an actual distribution circuit model of a utility.

2.1 Edge-of-Grid Voltage Control Device Specifications, Modeling, and Characteristics

The specifications, modeling, and voltage regulation characteristics of UPFC and SVC are discussed in this section.

2.1.1 UPFC Device Specifications

The universal power flow controller (UPFC) is a 50 kvar single-phase multi-function device that can provide voltage regulation and reactive power compensation [40, 41]. The device specifications are given in Table 2.1. The UPFC is designed to install on a service transformer secondary at 240 V voltage level. The structure of the UPFC is shown in Fig. 2.1. It has a series voltage injection transformer and a shunt current source. With this structure, the UPFC can be configured to operate in any of the three functional modes namely voltage regulation (mode 1), power factor correction (mode 2), and combined mode (mode 3) in which it can perform both voltage regulation and power factor correction simultaneously. In mode 1, the UPFC can boost or lower the voltage at its output up to 10% of its voltage rating, i.e., ±24 V with respect to its input node to maintain the output voltage at the voltage setpoint. This study focuses on the UPFC operation in voltage regulation mode only.

Table 2.1: Specifications of UPFC

Specification	**Details**
Rating	Single-phase, 60 Hz, 50 kVA
Load voltage regulation range	±10% with 0.5% accuracy
VAR compensation range	10% of rating (leading or lagging), i.e., up to 5 kvar
Operation modes	Mode 1: Voltage regulation Mode 2: Power factor correction Mode 3: Both voltage regulation and power factor correction

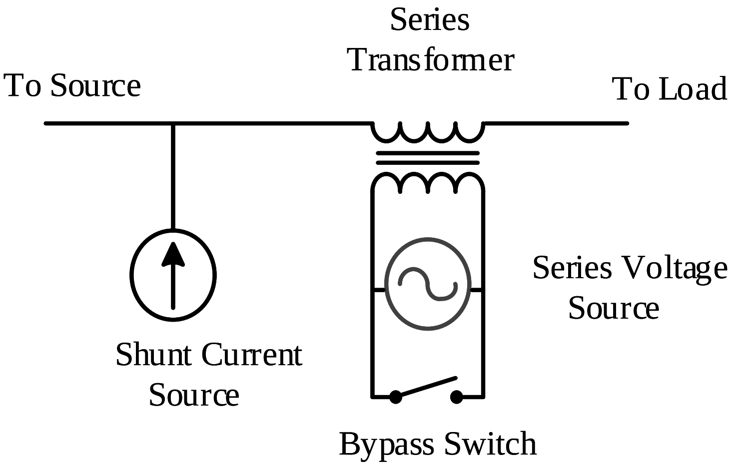

Figure 2.1: Structure of UPFC.

2.1.2 UPFC Modeling in OpenDSS

The steady state UPFC model available in OpenDSS is utilized for emulating the commercially available UPFC device in this study [42]. The mathematical model of the UPFC consistent with the formulation of the power flow problem in OpenDSS is shown in Fig. 2.2 [43]. The Thevenin equivalent of the series voltage source of UPFC is represented by the series impedance X_s and shunt current source I_s, where X_s is the impedance of the series transformer of the UPFC. The value of the current source I_s is given by [42]:

$$I_s = \frac{V_{diff} - (V_{out} - V_{in})}{jX_s} + I_s[z-1] \tag{2.1}$$

where V_{diff} is calculated as follows:

$$V_{diff} = (V_{ref} - |V_{in}|)e^{j\theta_{vin}} \tag{2.2}$$

where $I_s[z-1]$ is a shift register containing the value of the current source I_s calculated in the previous power flow solution iteration. Equations (2.1) and (2.2) are used to calculate the value of the current source iteratively until power flow convergence is reached. When the convergence is reached, the value of I_s will be equal to $I_s[z-1]$. The value of current source I_c is calculated as:

$$I_c = \frac{V_{out}}{I_s \times V_{in}} \tag{2.3}$$

Equation (2.3) allows to balance the power at input and output sides of the UPFC. The UPFC converts active power into reactive power to maintain the output voltage at reference voltage setting. As a result, (2.3) can be reformulated as:

$$I_c = -(\mathrm{real}(I_c) \times \mathrm{Losses} + \mathrm{imag}(I_s)) \tag{2.4}$$

where the ‘Losses’ corresponds to the losses of the device defined by a curve [42].

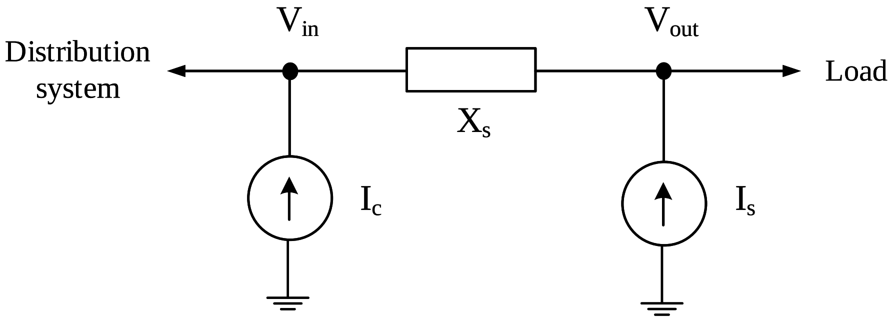

Figure 2.2: Mathematical model of UPFC.

2.1.3 Voltage Regulation Characteristics of UPFC

The voltage regulation characteristics of UPFC are studied by simulating a simple circuit shown in Fig. 2.3. The circuit has an ideal voltage source of 7.2 kV and a single-phase 7.2 kV/0.24 kV, 50 kVA service transformer. A load rated 15 kVA with 0.9 power factor lagging is connected to the service transformer secondary through a 100 ft service wire. An UPFC is connected to the service transformer secondary.

The UPFC is configured to regulate the output voltage at 1 pu in voltage regulation mode. The UPFC input voltage (V_{in}) is varied and the

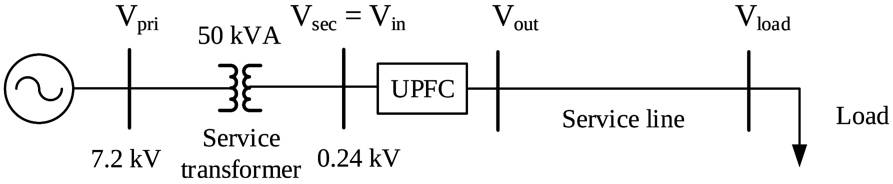

Figure 2.3: Study of UPFC characteristics using simple circuit.

load voltage without and with the UPFC device in service is plotted as shown in Fig. 2.4(a). It can be observed that when the UPFC is in service, the load voltage is regulated close to 1 pu throughout UPFC input voltage range from 0.9 pu to 1.1 pu. The UPFC injects voltage in series up to ±24 V to regulate the output voltage (V_{out}) to the specified value (V_{sp}). Note that the load voltage is slightly less than 1 pu due to the voltage drop in the service line. The series voltage injection by the UPFC ($V_{inj} = V_{out} - V_{in}$) as the input voltage is deviating from the specified voltage is depicted in Fig. 2.4(b). The UPFC injects positive voltage in series when the specified voltage V_{sp} is higher than the input voltage to regulate $V_{out} = V_{sp}$ and vice versa.

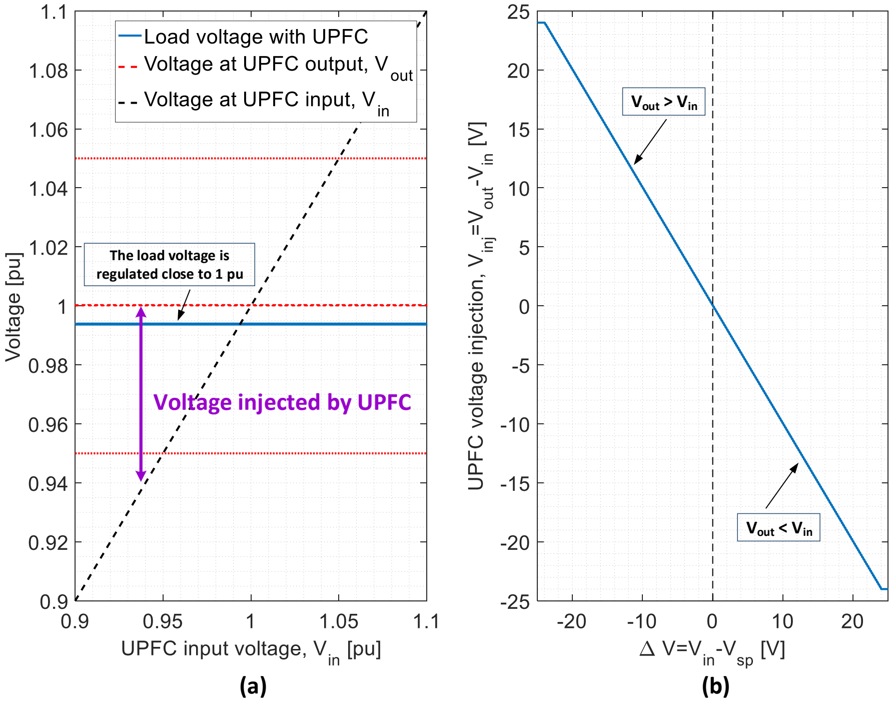

Figure 2.4: UPFC voltage regulation characteristics (a) Load voltage regulation (b) Voltage injection by UPFC.

2.1.4 SVC Device Specifications and Modeling in OpenDSS

The SVC is a single-phase shunt-connected device rated for 17.5 kvar. This device is designed to be installed on the secondary side of a distribution service transformer [7]. The structure of SVC is shown in Fig. 2.5. It consists of 4 capacitor units each supplying 4.375 kvar leading reactive power at 240 V. The SVCs provide required voltage boost at the installed location by bringing the required number of capacitor units into service. The specifications of SVC are given in Table 2.2. In this study, the SVC is modeled as a 4 stage single-phase capacitor bank of rating 17.5 kvar in OpenDSS with switch on setting equal to the specified voltage V_{sp} and switch off setting 3 V above V_{sp}.

Table 2.2: Specifications of SVC

Specification	**Details**
Rating	Single-phase, 60 Hz, 17.5 kvar
Capacitor stages	4 capacitor stages each rated for 4.375 kvar at 240 V
Voltage boost characteristic	Low threshold to switch in the capacitor stages; Start switching out the capacitor stages when terminal voltage is above 3 V of target voltage

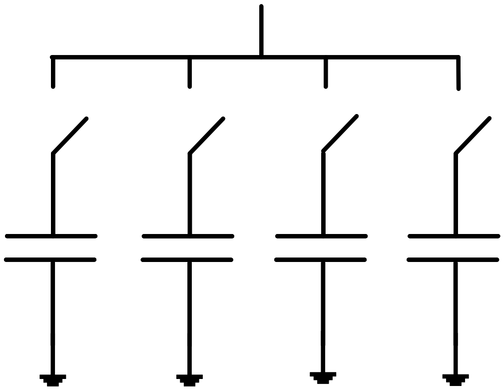

Figure 2.5: Structure of SVC.

2.1.5 Voltage Regulation Characteristics of SVC

The SVC voltage regulation characteristics are studied by simulating the SVC connected in shunt instead of UPFC in the same simple circuit shown in Fig. 2.6. The device characteristics as the service transformer secondary voltage V_{sec} (SVC terminal voltage) decreases are shown in Fig. 2.7. It can be observed that as the V_{sec_svc} is above the specified voltage of 1.0 pu (240 V), none of the capacitor stages are in service. As a result, both V_{sec_svc} and V_{sec_nosvc} align with each other. As the V_{sec_svc} voltage decreases below the specified voltage $V_{sp} = 1$ pu (240 V), the capacitor stages are switched in to maintain the voltage at V_{sp}. The voltage boost provided by the SVC is also evident from this figure.

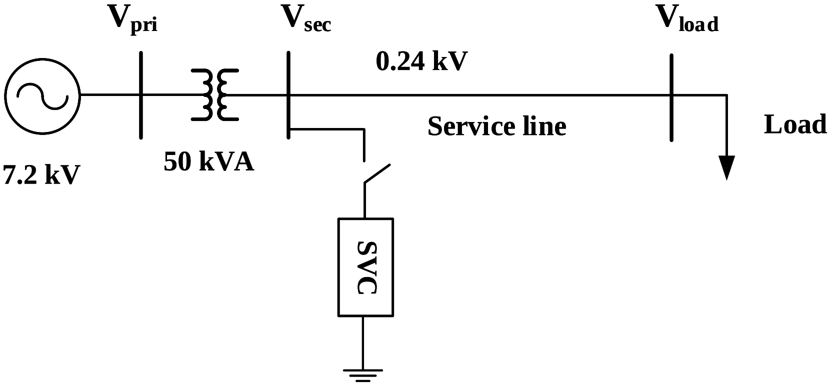

Figure 2.6: Study of SVC characteristics using simple circuit.

When the SVC terminal voltage is increasing, similar plot can be obtained as shown in to show that the capacitor stages switch off sequentially as the SVC terminal voltage goes above the upper threshold voltage of 1.0125 V (243 V) marked with the blue dashed line.

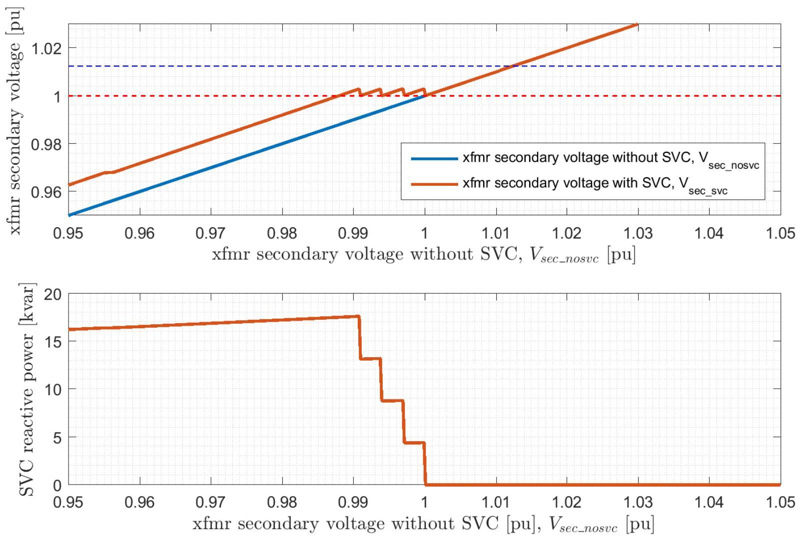

Figure 2.7: SVC voltage regulation characteristics when SVC terminal voltage decreases.

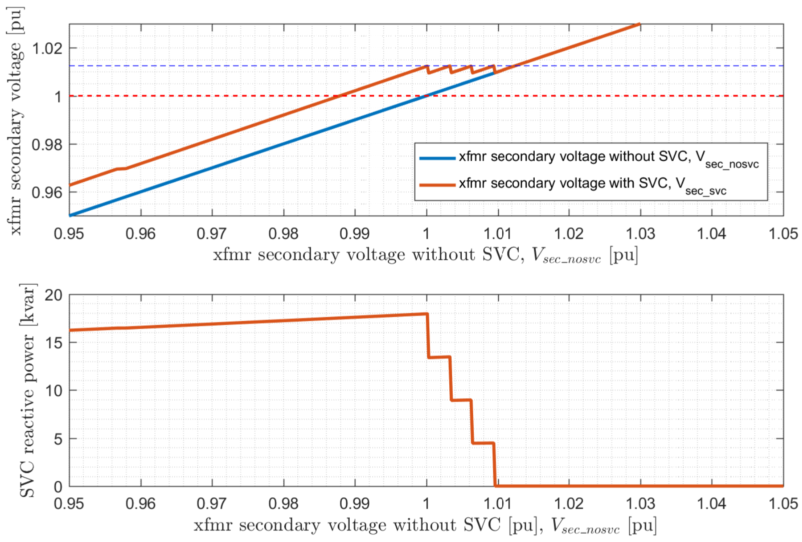

Figure 2.8: SVC voltage regulation characteristics when SVC terminal voltage increases.

2.2 Strategic Placement of Edge-of-grid Low-voltage Devices

In this section, the proposed iterative placement strategy for deployment of edge-of-grid voltage control devices in a real-world distribution circuit is discussed. The proposed method computes the undervoltage areas of load voltages from the peak day quasi-static time series (QSTS) simulation results to identify the effective locations for installation of the devices. Detailed distribution circuit model of a utility is used to study the proposed device placement method. The one-line diagram of the circuit used for this study is shown in Fig. 2.9. In this figure, the distribution line colors are contoured in accordance with their distances from the substation. This circuit has a 69/12.47 kV, 10.5 MVA substation transformer equipped with a load tap changer (LTC) control. Three single-phase mid-line voltage regulators are installed on each phase for voltage regulation. Additionally, there are seven switched capacitors installed along the feeder to provide both voltage regulation and power factor correction. The locations of this traditional voltage regulation equipment are marked in the one-line diagram in Fig. 2.9.

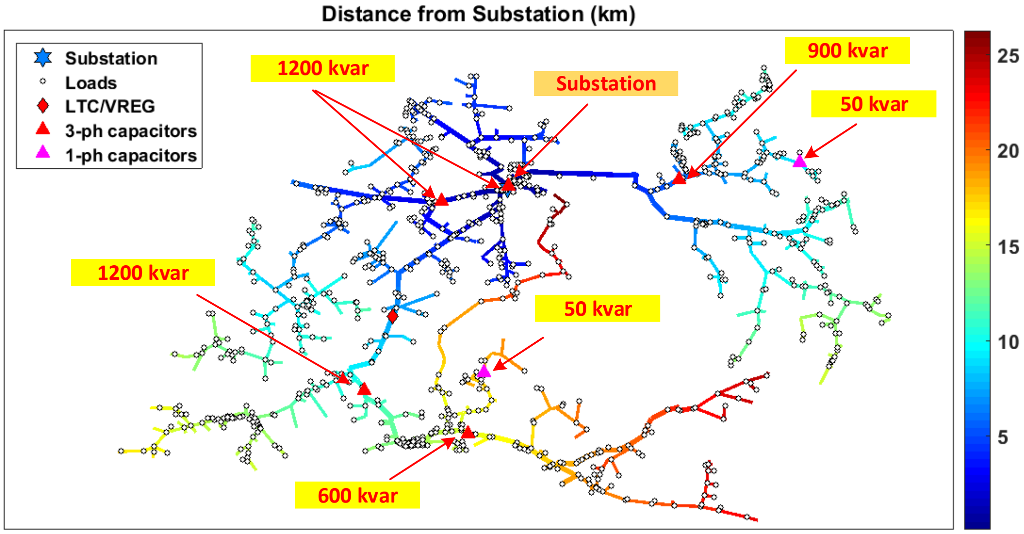

Figure 2.9: One-line diagram of the distribution circuit used in this study.

Three potential criteria, as illustrated in Fig. 2.10, can be considered for the device placement in response to undervoltages: lowest minimum voltage magnitude, longest undervoltage duration, and largest undervoltage area. As shown in this figure, the undervoltage area is simply the area bounded by the voltage profile curve and the voltage threshold line. The undervoltage area criterion provides a more robust indicator for siting a set of advanced voltage control technologies to mitigate long duration voltage deviations [44] and therefore it is used in this work for the device deployment.

An iterative placement method is proposed to deploy a set of 1 UPFC and 15 SVC devices in the distribution circuit. In the iterative placement method, QSTS for the peak load day is performed in each iteration and one device is placed on the service transformer secondary corresponding to the load

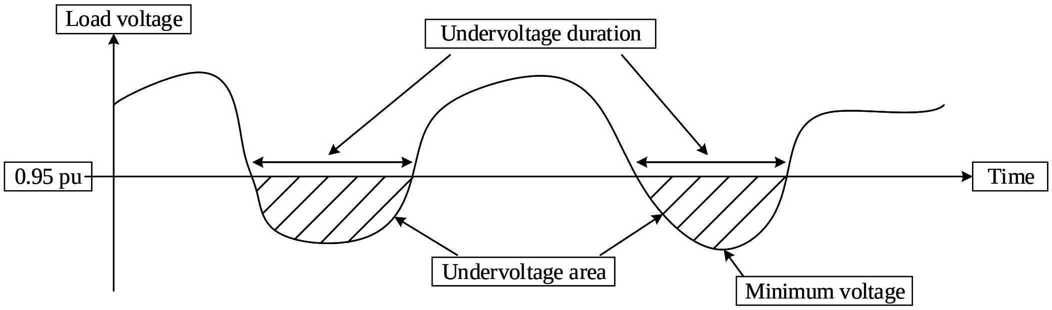

Figure 2.10: Illustration of potential device placement criteria.

having the highest undervoltage area. If the service transformer identified in this way has already a device installed, adjacent service transformer is selected for the device placement. The steps for the iterative placement are shown in Fig. 2.11.

Due to the practical space constraints in the field, only one device is allowed to install per service transformer secondary (per pole). Furthermore, because the UPFC is a series device only the service transformers with sizes equal to or below the device rating (50 kVA) are considered as candidates for installing UPFC to avoid overloading of the UPFC. Additionally, as the SVC devices are shunt-connected, the service transformers with size 20 kVA or above are the candidate locations to avoid overloading of the service transformer. These constraints are also considered in the device deployment.

For comparison, the scenario with all the traditional voltage regulation equipment is in service and the edge-of-grid voltage control devices (UPFC and SVCs) are out of service is considered as the base case scenario. The load demand profile observed at the substation on the summer peak day is shown in

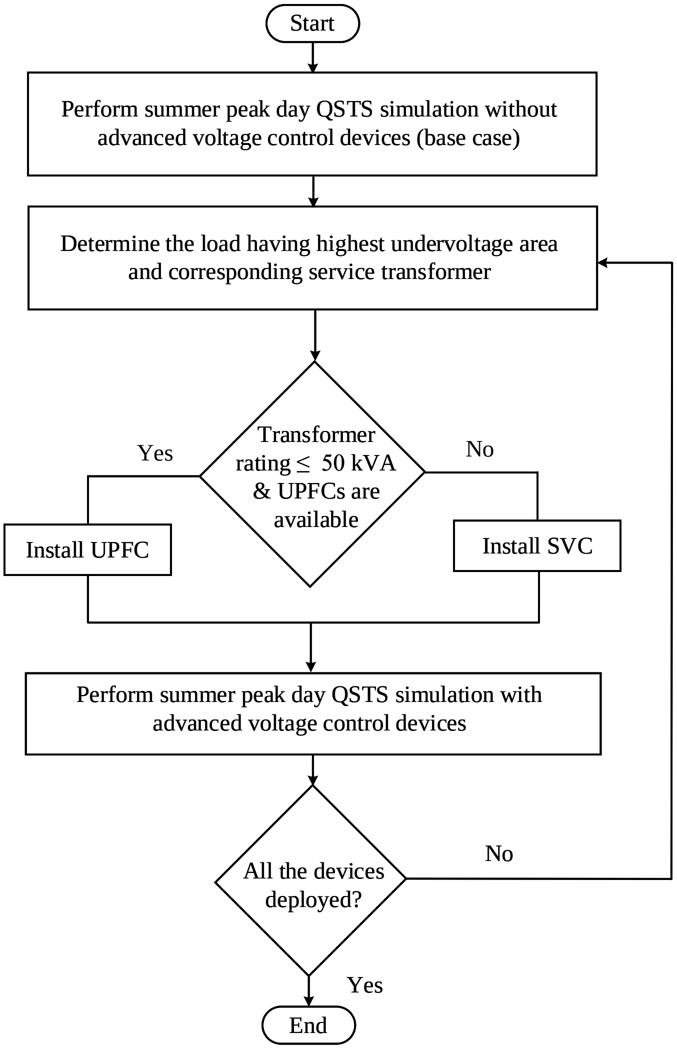

Figure 2.11: Steps for iterative placement method.

Fig. 2.12. A maximum demand of 5.55 MW is observed on the peak day. From the peak day QSTS simulation results of the base case, carried out at 1 min resolution, it is identified that there are 129 loads that experience undervoltage violations on that day. Heat map showing each service point's undervoltage area is shown in Fig. 2.13. In this map, each service point is represented by a single dot whose color represents the specific value of the respective metric computed based on the 24-hour simulation results. The map shows that the loads with undervoltages are distributed in three clusters (clusters 1, 2, 3). Loads in clusters 1 and 2 (marked with red circles) are on phase A, while the loads in cluster 3 (marked with a blue circle) are on phase C. Note that these three clusters are located farthest from the substation (see Fig. 2.9).

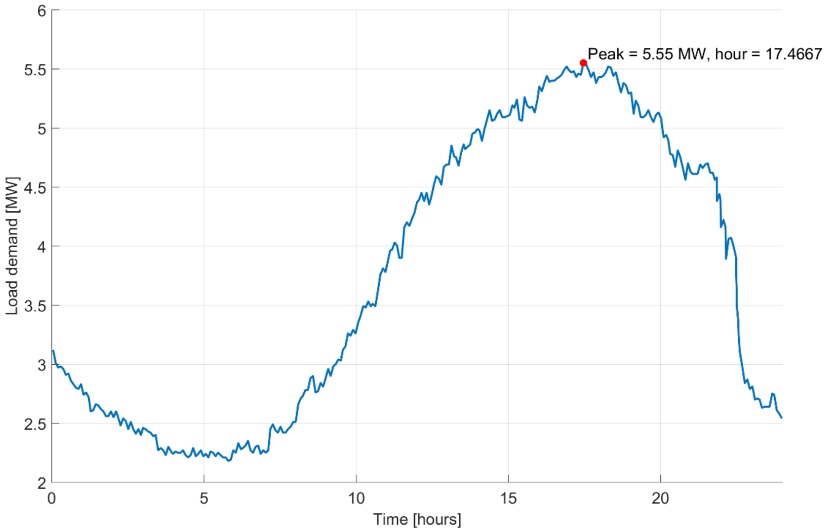

Figure 2.12: Load profile on summer peak day.

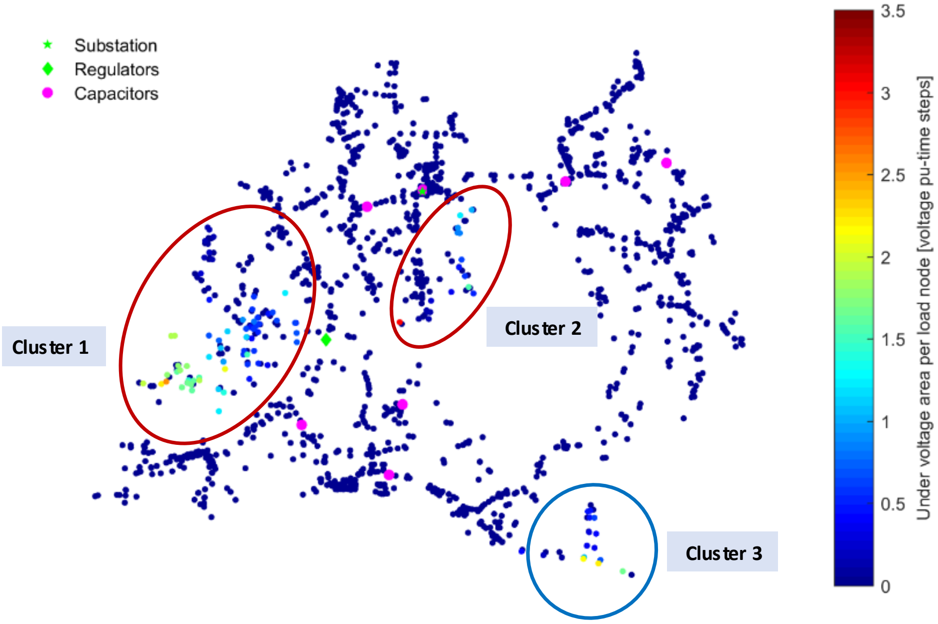

Figure 2.13: Heat map of the undervoltage area at each load and undervoltage clusters in the base case.

The feeder voltage profile obtained from the peak load snapshot simulation without and with the edge-of-grid voltage control devices is shown in Fig. 2.14. It is observed that the loads on the phases A and C experience undervoltage violations in the base case scenario. Nevertheless, after placing the edge-of-grid voltage control devices using the iterative placement approach, the undervoltage violations are eliminated as seen in Fig. 2.14b.

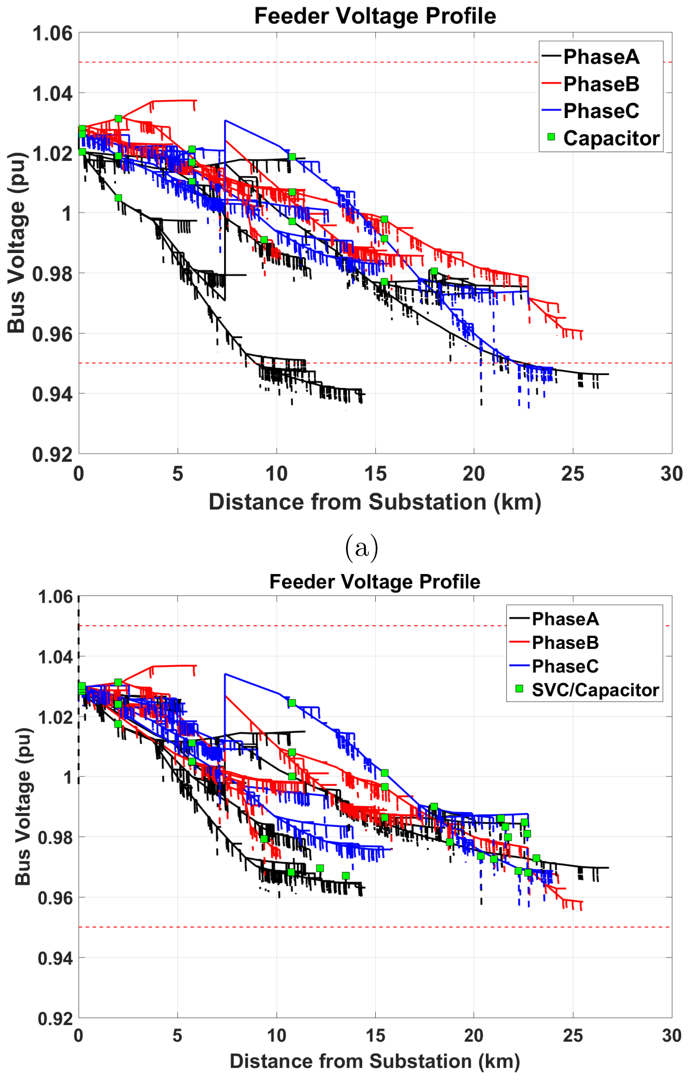

(a)

(b)

Figure 2.14: Feeder voltage profile at peak load (a) Base case (b) After deploying UPFC and SVC devices.

To further study the voltage violations, QSTS simulation of the circuit is performed for a period of 24 hours with 1 min resolution for the peak day. The QSTS simulation results after deploying the devices are shown in Fig. 2.15. For ease of visualizing all the load voltages at each time step, statistical summary of load voltages is shown in Fig. 2.15. In this figure, the upper plot depicts all the load voltages during the peak day. To generate these results, initially all the load voltages are obtained at each time step. Then a probability density function (PDF) is applied to the histogram of the load voltages. The 'kernel' distribution is assumed for the load voltages as it better fits the histogram of the load voltages. This process is repeated for all the time steps and a contour plot is generated for the load voltages as shown in Fig. 2.15. For each time step, the contour's color signifies the number of customer voltages experiencing a particular voltage magnitude. From the peak day QSTS results, it is observed that the undervoltage violations in the circuit are eliminated. Furthermore, the total reactive power support from the capacitor banks and the SVC devices are shown in the lower part of Fig. 2.15. From this figure, it is observed that during the period from 14 hours to 23 hours on the peak day, the SVC devices are providing an additional reactive power support close to 260 kvar which is the total kvar rating of 15 SVC devices. This shows that, with the proposed iterative placement approach, all the 15 SVC devices will be fully utilized in eliminating the undervoltage violations.

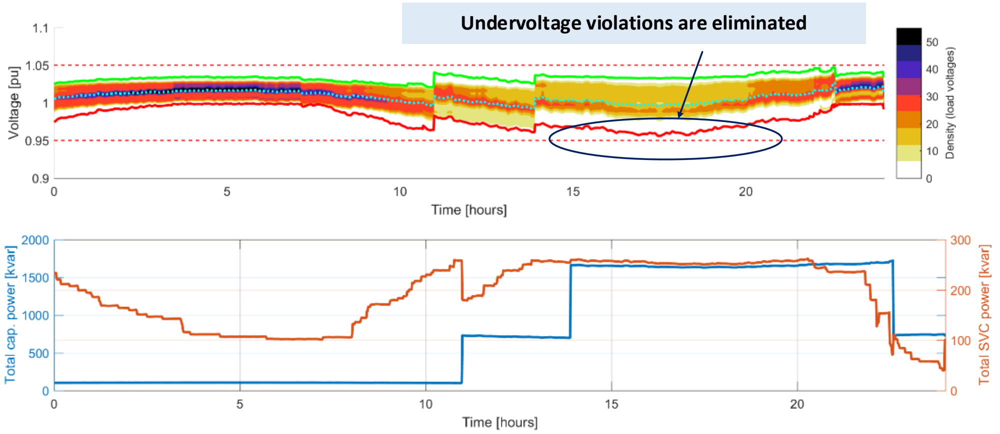

Figure 2.15: Peak day QSTS results after device deployment using iterative placement method.

2.3 Summary

In this work, the modeling and voltage regulation characteristics of two edge-of-grid voltage control technologies are discussed. An iterative placement approach based on undervoltage area criterion is proposed to determine the effective locations to install these devices in real-world distribution circuits for voltage regulation. In this approach, quasi-static time-series simulation (QSTS) is performed using the load profile information on the peak day to determine the loads experiencing the low voltages. An edge-of-grid device is placed at the service transformer secondary experiencing the highest undervoltage area in the first iteration. In the next iteration, the peak day QSTS is performed again with the edge-of-grid device in service. This process is repeated by placing one device in each iteration while keeping the devices placed in the preceding iterations in service, until there are no low voltage violations in the circuit. The study results show that the proposed approach is efficient in selecting the locations for installing these devices for voltage regulation in distribution circuits.

Chapter 3

Optimal Placement of Low-Voltage SVCs in Distribution Circuits

The edge-of-grid voltage control devices, in particular, the static var compensators (SVCs) inject reactive power into the distribution circuit by switching in required number of capacitor stages. The reactive power support provided by a set of these devices can alter the power flow in the circuit. [1]This chapter focuses on determining the optimal locations for SVCs in distribution circuits. In general, the SVCs act as additional reactive power sources that can improve the power factor and help lower the active power losses. Although, several methods have been reported in literature to deploy traditional voltage regulation equipment on the primary distribution circuit [37–39, 45], analysis for optimal allocation of edge-of-grid low-voltage devices considering the secondary circuit is lacking. The iterative placement method presented in Chapter 2 is an effective approach in eliminating the undervoltage violations. However, it does not take into account important parameters such as

---

[1] Parts of this chapter appear in the published paper, 'H. V. Padullaparti, Min Lwin, and S. Santoso, "Optimal Placement of Edge-of-Grid Low-voltage SVCs in Real-world Distribution Circuits," *IEEE Workshop on Power Electronics and Power Quality Applications*, Bogota, 2017, pp. 1-6'. The author of this dissertation contributed all the sections in this paper as first author.

traditional voltage regulation device switching operations and active power losses in determining the effective locations. It is important to consider these parameters also [46] in the SVC placement as the SVCs, with their voltage regulation capability and potential for reactive power compensation, can help minimize the number of traditional voltage regulation equipment operations and circuit losses as well.

In this chapter, the SVC placement problem is formulated as a multi-objective optimization problem to minimize undervoltage violations, number of SVCs, traditional voltage regulation equipment switching operations, and circuit losses. The optimization problem is then solved using the binary particle swarm optimization (BPSO) algorithm.

3.1 Distribution Circuit Details

The detailed distribution circuit model and the load profile information used for this study are same as that used in Chapter 2. The one-line diagram of the circuit, generated using GridPV tool [47], is shown in Fig. 3.1. This circuit has a 69/12.47 kV, 10.5 MVA substation transformer equipped with a load tap changer (LTC) control. Three single-phase mid-line voltage regulators are installed on each phase for voltage regulation. Additionally, there are seven switched capacitors installed along the feeder to provide both voltage regulation and power factor correction. The locations of these traditional voltage regulation equipment are marked in the one-line diagram in Fig. 3.1.

The scenario with all the traditional voltage equipment are in service and SVCs are out of service is considered as the base case scenario. From the peak day QSTS simulation results of the base case, it is identified that there are 129 loads that experience undervoltage violations on that day. Out of the 129 locations, 109 locations have corresponding service transformers with ratings $\geq$ 20 kVA. Note that as the SVCs are rated for 17.5 kvar, only the service transformers with ratings $\geq$ 20 kVA are suitable locations to install the SVCs. These 109 locations are segregated into 3 clusters highlighted by the red circles in Fig. 3.1. From the study reported in [44], it is found that the service transformers corresponding to loads having highest undervoltage area are good candidate locations for installing SVCs. The concept of undervoltage area is also discussed in [44]. There are 36 loads having undervoltage area higher than 1 pu-minute during the peak day. The corresponding service transformer secondaries are selected as candidate locations for installing SVCs which are marked by cyan asterisks in Fig. 3.1. The goal is to determine optimal SVC locations among these 36 candidate locations. Furthermore, due to the limitation of space on the service transformer poles in the field, only one SVC is allowed to be installed on each service transformer secondary.

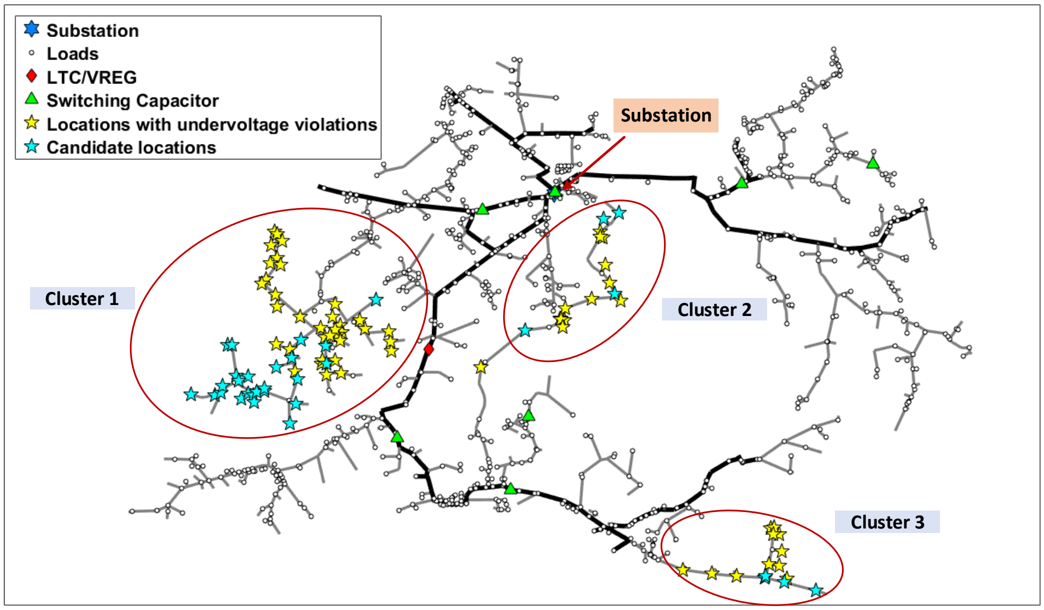

Figure 3.1: One-line diagram of the distribution circuit.

The feeder voltage profile at the peak load snapshot simulation along with the capacitor locations is shown in Fig. 5.2. It can be observed that many loads on phases A and C experience undervoltage violations, i.e., voltages lower than 0.95 pu at the peak load.

3.2 Optimal SVC Locations using Binary Particle Swarm Optimization (BPSO)

3.2.1 Binary Particle Swarm Optimization (BPSO)

The PSO is a population based search algorithm originally developed by Kennedy and Eberhart [48]. There are two original versions of this algorithm. One version introduced in 1995 [48] works on the real-valued space and deals

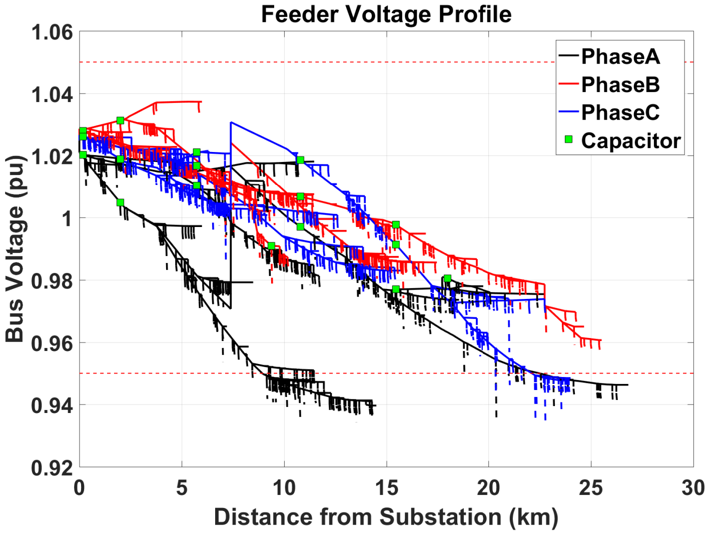

Figure 3.2: Feeder voltage profile at peak load.

with continuous variables. The other version namely BPSO, introduced in 1997 [49], was designed for solving binary problems wherein the decision vector is a bitstring consisting of 0s and 1s. In this work, determination of optimal SVC locations is formulated as a binary optimization problem and the BPSO is used as an optimizer.

A detailed description of the BPSO algorithm can be found in [49]. The steps involved in the functioning of BPSO are briefly described below:

1. Randomly initialize a population of particles in D-dimensional space in the first iteration. The number of decision variables determines the size of D. The i^{th} particle in the first iteration can be represented as $X_i^1 = (X_{i1}^1, X_{i2}^1, ..., X_{id}^1)$. Each particle is a potential solution to the binary optimization problem.

2. The objective function value f_{obj} for each particle is computed in each iteration k and stored in the vector f^k. The relative merits of particles are determined by their corresponding f_{obj} value. The individual particle's best position in each iteration k and the overall best position of all the particles up to k iterations are saved as pb^k and gb^k, respectively.

3. BPSO computes the population velocity in each iteration using (3.1):

$$v_{id}^{k+1} = \omega v_{id}^k + c_1 r_1 (pb_{id}^k - x_{id}^k) + c_2 r_2 (gb_{id}^k - x_{id}^k) \tag{3.1}$$

where $v_i^k = (v_{i1}^k, v_{i2}^k, ..., v_{id}^k)$ represents the velocity of particles in k^{th} iteration. Additionally, c_1, c_2 are positive constants and r_1, r_2 are random numbers, uniformly distributed between 0 and 1. The inertia weight parameter ω adjusts the velocity of the particles and creates a balanced local and global search. The pb_{id} and gb_{id} are integers in $\{0, 1\}$. The v_{id}, being a probability, is to be constrained to the interval $[0.0, 1.0]$.

4. Sigmoid limiting transformation $sigmoid(v_{id}^{k+1})$ defined as (3.2) is used to restrict v_{id}^{k+1} to the interval $[0.0, 1.0]$. Then the new particle position is computed using (3.3):

$$sigmoid(v_{id}^{k+1}) = \frac{1}{1 + e^{-v_{id}^{k+1}}} \tag{3.2}$$

$$x_{id}^{k+1} = \begin{cases} 1 & \text{if } sigmoid(v_{id}^{k+1}) > rand() \\ 0 & \text{otherwise} \end{cases} \tag{3.3}$$

where $rand()$ is a quasi-random number selected from a uniform distribution in $[0.0, 1.0]$.

5. The global best particle position obtained after a preset number of iterations is the optimal solution.

3.2.2 Problem Formulation

In this work, the determination of optimal SVC locations is formulated as a multi-objective optimization problem with the objective function defined in (3.4). Then the binary optimization problem is solved using the BPSO algorithm discussed in Section 3.2.1. In the BPSO, the length of each particle is equal to the number of candidate locations to install SVCs. Each bit in the particle represents the decision to install SVC or not at a candidate location with '1' representing installing an SVC at that location and '0' representing not installing an SVC. As the BPSO algorithm runs, for each set of SVC locations, a peak day QSTS simulation is run with the SVCs deployed at those locations. The objective function value f_{obj} is computed from the QSTS simulation results.

$$\begin{aligned} f_{obj} = W_{uv} \times \Sigma \text{ Undervoltage area} + W_{svc} \times \text{No. of SVCs} \\ + W_{do} \times \text{Device operations} + W_l \times \text{Losses} + \text{Penalty} \end{aligned} \tag{3.4}$$

There are five terms in the objective function. The first term represents the sum of undervoltage areas in the circuit for a given deployment of SVCs multiplied by a weight W_{uv}. The second term is the number of SVCs deployed scaled by weight W_{svc}. The product of the weight W_{do} and the number of traditional voltage regulation device operations, i.e., the sum of regulator tap changes and capacitor on/off status changes obtained from the peak day QSTS simulation are represented by the third term. The average energy losses per hour in kWh during the peak day multiplied by weight W_l is represented by the fourth term. A penalty can be added to the objective function when the number of SVCs exceeds a preset value. This is useful if the number of SVCs is to be restricted to some value. Minimizing the objective function (3.4) means determining minimum number of SVC locations that result in minimum undervoltage violations while keeping the traditional voltage regulation device operations and circuit losses as low as possible with the deployment of SVCs. The weights are useful in setting the relative importance of each term as well as to scale their magnitudes appropriately with respect to each other.

3.2.3 Results and Discussion

The parameters used for BPSO are given in Table 3.1. The selected BPSO weighing factors are checked for few BPSO runs and found to be working satisfactorily. The global best objective function value as the BPSO iterations progress, shown in Fig. 3.3, indicates that the minimum objective function value is reached at iteration 31. The weights in the objective function are chosen based on their relative importance and the magnitude of the terms obtained from the QSTS simulation results as described in Section 3.2.2. These weights are chosen to ensure the terms in the objective do not dominate each other for reasonable potential solutions.

The optimal SVC locations determined by BPSO for the selected objective function are marked by red asterisks in Fig. 3.4. It is observed that

Table 3.1: BPSO parameters

Parameter	**Value**
No. of particles	40
No. of iterations	50
BPSO weighing factors	$c_1 = 0.5, c_2 = 1.25$, and ω varies linearly from 0.9 to 0.4
Objective function weights	$W_{uv} = 2, W_{svc} = 1, W_{do} = 1, W_l = 0.001$
Penalty	A penalty of 50 is added if No. of SVCs > 15

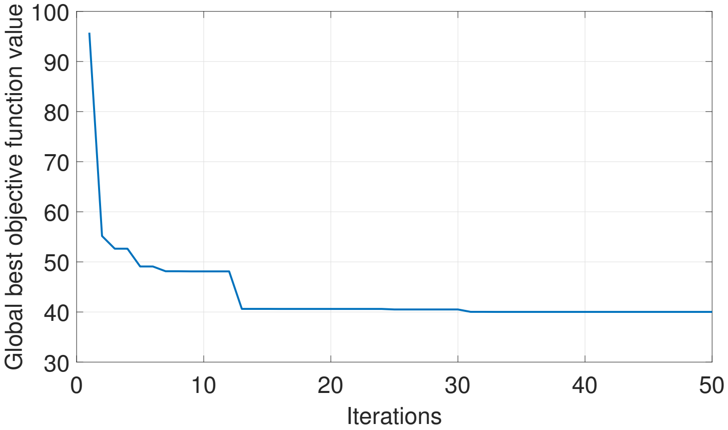

Figure 3.3: Global best objective function value against iterations.

required number of SVCs are placed in each cluster at appropriate locations to mitigate the undervoltage violations. There are five SVCs placed in cluster 1, four in cluster 2, and three in the cluster 3. The voltage profile at peak load snapshot after deploying the 12 SVCs, depicted in Fig. 3.5, shows that the undervoltage violations are almost eliminated with the optimal placement of the SVCs. However, one load experiences undervoltage of magnitude 0.9452 pu at the peak load snapshot (encircled in Fig. 3.5) which is not significant. Compared to the base case voltage profile shown in Fig. 5.2, there is a significant improvement in the voltage profile after the deployment of 12

SVCs at the optimal locations. It is observed that an SVC is already installed at the corresponding service transformer secondary of the load experiencing the undervoltage violation. The peak day QSTS simulation results with the SVCs deployed further confirmed that it is the only load that experiences undervoltage resulting in an undervoltage area of 0.0684 pu-m. The summary of peak day QSTS simulation results after deploying the 12 SVCs is shown in Table 4.2. The results show that the deployment of SVCs result in negligible total undervoltage area, reduced traditional voltage regulation device operations, lower energy losses and improved minimum voltage level during the peak day compared to the base case scenario.

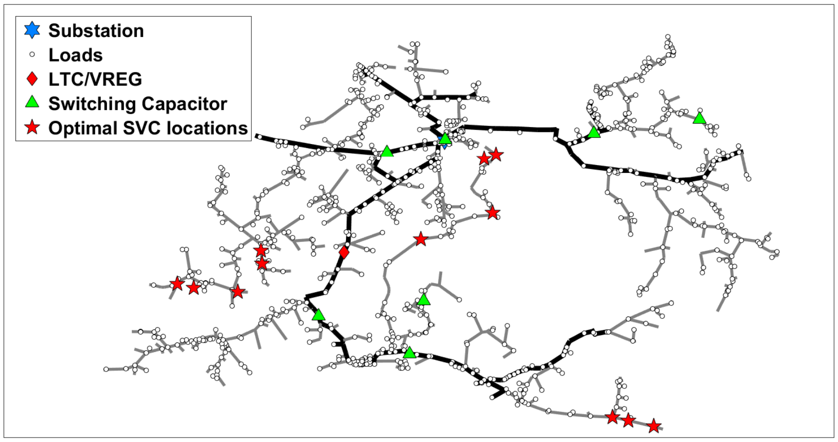

Figure 3.4: Optimal SVC locations in the distribution circuit.

The total reactive power support from capacitor banks in the base case scenario and from capacitors as well as SVCs after optimal deployment of the SVCs are shown in Fig. 3.6. From Fig. 3.6b, it is observed that during the period from 14 hours to 23 hours on the peak day, the SVCs are providing an additional reactive power support is close to 210 kvar which is the sum of the total kvar rating of 12 SVCs. This shows that, with the given optimal placement of SVCs, all the 12 SVCs will be fully utilized in mitigating the undervoltage violations while improving the other important parameters considered in the objective function.

Table 3.2: Summary of peak day QSTS simulation results

Parameter	Base case	SVCs deployed
Σ Undervoltage area [pu-m]	106.53	0.0684
No. of SVCs	0	12
Device operations	16	10
Energy losses [kWh]	1082.4	1066.4
Minimum voltage [pu]	0.9320	0.9452

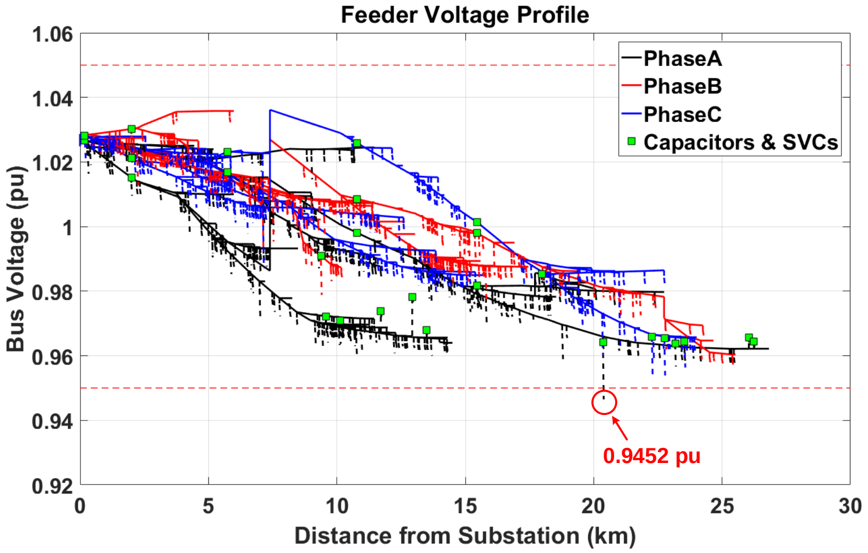

Figure 3.5: Feeder voltage profile at peak load with optimal SVC placement.

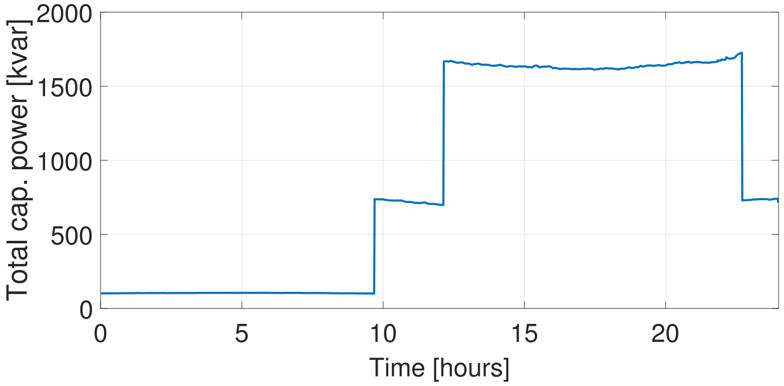

(a)

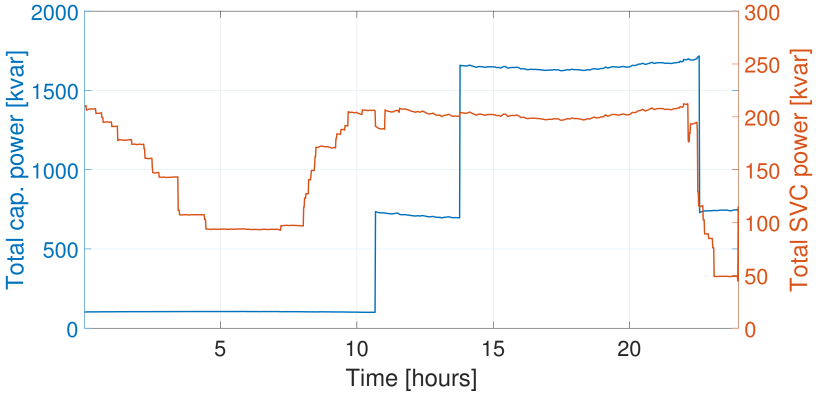

(b)

Figure 3.6: Reactive power support during peak day (a) Base case (b) After deployment of SVCs.

3.3 Summary

In this chapter, a new method to determine optimal locations to deploy edge-of-grid low-voltage SVCs in large distribution circuits is proposed. The goal is to mitigate undervoltage violations in the circuit using minimum number of SVCs while improving the traditional voltage regulation device operations and circuit losses. Undervoltage area criterion is used to limit the optimal solution search space and BPSO algorithm with QSTS simulations is used as optimizer. The findings show that the proposed method is effective in identifying the optimal locations for installation of SVCs in large distribution circuits while meeting multiple desired objectives.

Chapter 4

Optimal Placement and Real-Time Control of LV-SVCs to Minimize Energy Losses

The volt/var optimization utilizing the edge-of-grid static var compensators (SVCs) in distribution circuits using iterative placement and binary particle swarm optimization (BPSO) is discussed in Chapters 2 and 3. While the iterative placement algorithm considers undervoltage violations as the primary objective to identify the effective SVC locations, the multi-objective optimization using the BPSO algorithm seeks to minimize the undervoltage violations, traditional voltage regulation equipment switching operations, active power losses by installing minimum number of SVCs. Both the algorithms, however, consider the operation of the SVCs using local autonomous voltage-based controllers, i.e., the reactive power output from the SVCs depends upon their terminal voltage and voltage setpoint. Nevertheless, the edge-of-grid devices offer two-way communication capabilities [22, 23] for data exchange and receiving control commands from a central location which is typically the substation. Such communication capabilities, in the presence of load data availability with advanced metering infrastructure (AMI) [24–26], can be utilized to apply a centralized control to adjust the reactive power outputs of SVCs in real-time to optimize the performance the distribution network.

In this chapter, a two-stage optimization framework is proposed for placement and real-time control of low-voltage static var compensators (LV-SVCs) in unbalanced distribution circuits to achieve feeder level benefits namely loss minimization and voltage regulation. The LV-SVC considered in this work is similar to the SVC discussed in Chapter 2. However, the rating of LV-SVC is considered as 20 kvar with 20 capacitor stages of 1 kvar each. The loads are modeled as constant power loads. The number, locations, and the optimal real-time reactive power injections from the LV-SVCs are determined from a proposed three-phase unbalanced AC optimal power flow (ACOPF). The ACOPF is formulated as a multi-objective optimization with operating constraints written in rectangular coordinates. The resulting nonlinear nonconvex problem is solved using the predictor-corrector primal-dual interior point method (PCPDIPM). The proposed approach is scalable for application to large distribution circuits, treats the constraints of physical space limitations effectively, and can takes advantage of communication capabilities of LV-SVCs for centralized optimal control. The benefits of centralized control of LV-SVCs as compared to their operation with local autonomous voltage-based controls is demonstrated.

4.1 Distribution Circuit Details

The effectiveness of the proposed optimization framework for siting and dispatch of LV-SVCs is demonstrated on a large-scale distribution circuit namely Circuit 5. The details of this circuit are presented in this section.

The one-line diagram of the Circuit 5, plotted using Sandia GridPV tool [47], is shown in Fig. 4.1. This circuit has a 115/12.47 kV, 10 MVA substation transformer with a peak load demand of 8.12 MVA. Four switched capacitors are available in this circuit. The line voltage regulators are not available. The circuit model includes low-voltage secondary system where the loads are connected and are interfaced to the primary system through service transformers. The source voltage is set to 1.035 pu and the switched capacitors are disabled to create voltage violations in this circuit for this study. In Fig. 4.1, the colors of the lines are in accordance with the corresponding line voltage magnitude observed at the peak load. At the peak load, low voltages are observed in the feeder neighborhoods FN1 and FN2. To simulate the daily load variation, all the loads are set to vary according to the typical load profile shown in Fig. 4.2.

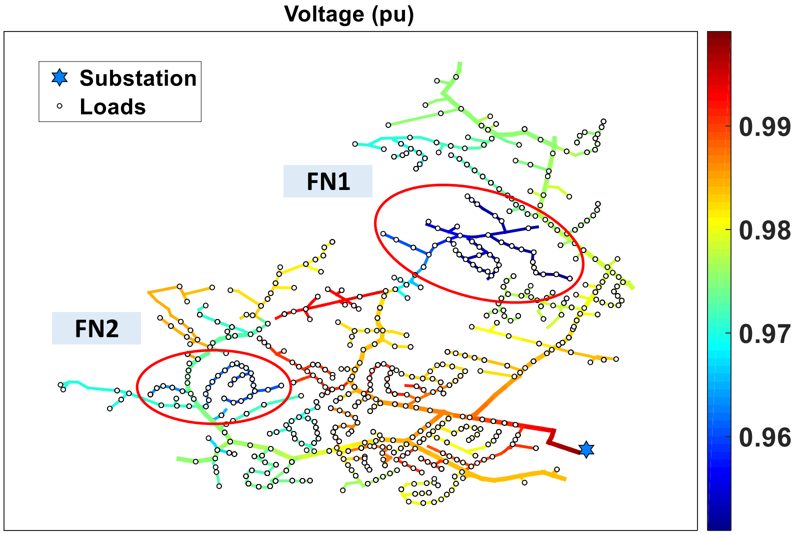

Figure 4.1: One-line diagram of Circuit 5.

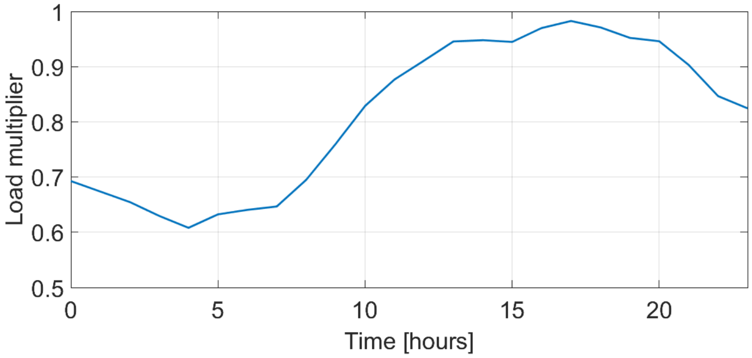

Figure 4.2: Typical daily load profile.

4.2 LV-SVC Characteristics

The voltage regulation characteristics of low-voltage SVC (LV-SVC) operating on local voltage-based controller are studied in this section. The LV-SVCs are assumed to be rated for 20 kvar with 20 capacitor stages of 1 kvar each in this study. When switched in, each capacitor stage injects 1 kvar into the circuit. The number of capacitor stages required to be switched in at a given time step depends upon the LV-SVC terminal voltage and its voltage setpoint at that time step. The LV-SVC characteristics can be plotted by connecting an LV-SVC to the service transformer secondary node in a simple circuit as discussed in Section 2.1.5. The resulting voltage regulation characteristics of the LV-SVC is shown in Fig. 4.3. As the node voltage becomes lower than the voltage setpoint of 0.95 pu, the LV-SVC injects the required amount of reactive power up to 20 kvar to regulate the node voltage at 0.95 pu. The reactive power injection in 1 kvar stages can also be observed in the second graph of Fig. 4.3.

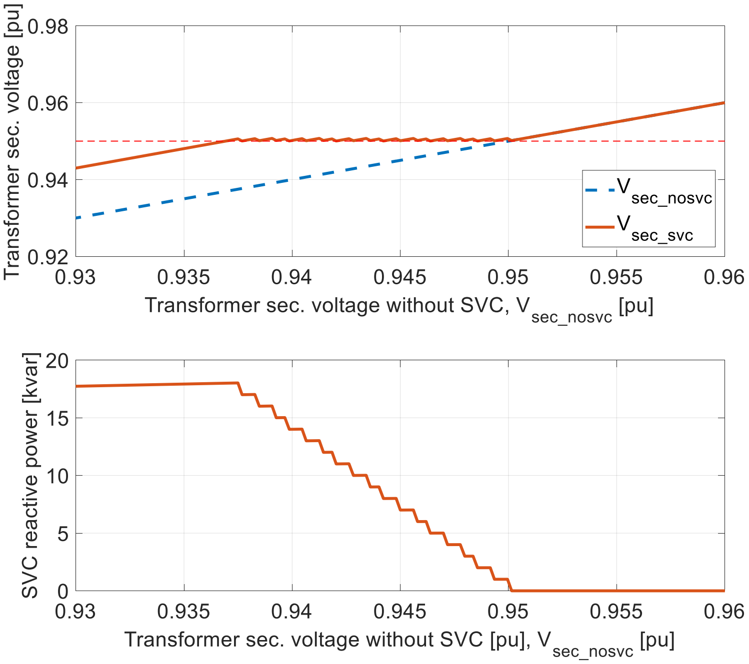

Figure 4.3: Voltage regulation characteristics of an LV-SVC.

4.3 The Proposed Three-phase Unbalanced AC OPF Formulation and Solution

This section proposes a generalized optimization formulation to determine the optimal reactive power dispatch of capacitors. The formulation, which is written in rectangular coordinates, includes a multi-objective function and operational constraints that ensure the desired performance. The optimization problem is solved using the Predictor-Corrector Primal-Dual Interior Point method (PCPDIPM).

4.3.1 State and Decision/Control Variables

The state variables $\boldsymbol{x}$ consist of the real part $\boldsymbol{V_r}$ and imaginary part $\boldsymbol{V_i}$ of voltages in the rectangular coordinates at all nodes of $\mathcal{N}$, which is defined as a set of all nodes except those at the substation bus. The decision variables $\boldsymbol{u}$ consist of the reactive power $\boldsymbol{Q}^{svc}$ generated by switched capacitors. The decision vector is thus given as follows:

$$\boldsymbol{X} = [\boldsymbol{x}^T | \boldsymbol{u}^T] = [\boldsymbol{V_r}^T, \boldsymbol{V_i}^T | \boldsymbol{Q}^{svcT}]^T. \tag{4.1}$$

4.3.2 System-wide Optimization Objectives

- LV-SVC Installation Cost: The cost of installing the LV-SVCs is assumed to linearly vary according to the total reactive power supplied from all the LV-SVCs:

  $$\min\ f_1(\boldsymbol{X}) = \sum_{k \in \mathcal{N}^{svc}} Q_k^{svc}. \tag{4.2}$$

  where α_1 is the weight coefficient representing LV-SVC installation cost while $\mathcal{N}^{svc}$ is the set of all nodes connected to the switched capacitors.

- Loss Minimization: Within a time step, the total measured load is assumed to be constant. Therefore, minimizing the system loss is equal to minimizing the sum of active power supplied by the three-phase substation (P_{abc}^{sub}).

  $$\min\ f_2(\boldsymbol{X}) = \alpha_2 \sum_{k=a,b,c} P_k^{sub}. \tag{4.3}$$

  where α_2 is the cost associated with the energy loss.

4.3.3 Operational Constraints

Power Balance Constraints The first constraint involves the active and reactive power balance at every node $k \in \mathcal{N}$:

$$g_k^P(\boldsymbol{X}) = P_k + P_k^l = 0, \tag{4.4a}$$

$$g_k^Q(\boldsymbol{X}) = Q_k + Q_k^l - Q_k^{svc} = 0, \tag{4.4b}$$

where P_k^l and Q_k^l are the load active power and load reactive power at node k, respectively. The active and reactive power P_k and Q_k injected into the system from node k in (4.4) are given by:

$$P_k = \boldsymbol{G_{k:}}(V_{r,k}\boldsymbol{V_r} + V_{i,k}\boldsymbol{V_i}) + \boldsymbol{B_{k:}}(V_{i,k}\boldsymbol{V_r} - V_{r,k}\boldsymbol{V_i}), \tag{4.5a}$$

$$Q_k = \boldsymbol{G_{k:}}(V_{i,k}\boldsymbol{V_r} - V_{r,k}\boldsymbol{V_i}) - \boldsymbol{B_{k:}}(V_{r,k}\boldsymbol{V_r} + V_{i,k}\boldsymbol{V_i}), \tag{4.5b}$$

where $V_{r,k}$ and $V_{i,k}$ are active and imaginary parts of the voltage at node k while $\boldsymbol{G_{k:}}$ and $\boldsymbol{B_{k:}}$ are the conductance and susceptance vectors obtained from the k^{th} row of the admittance matrix.

Voltage Constraints

$$\underline{V}^2 \leq (V_{r,k})^2 + (V_{i,k})^2 \leq \bar{V}^2, \forall k \in \mathcal{N}^l, \tag{4.6}$$

where $\underline{V}$ and $\bar{V}$ are the lower and upper bounds of the load voltage and $\mathcal{N}^l$ is the set of nodes connected to the loads.

LV-SVC Constraints

$$Q_k^{svc} \in \mathcal{C}_k, \forall k \in \mathcal{N}^{svc}, \tag{4.7}$$

where $\mathcal{C}_k$ is the set of discrete power values of the switched capacitor at node k while $\mathcal{N}^{svc}$ is the set of all nodes connected to the switched capacitors. However, Q_k^{svc} in this paper is first treated as a continuous variable in the conventional PCPDIPM. When the solution is about to converge, a quadratic penalty function is added to the objective function to force the discrete variables converge to their discrete values [50]. Therefore, (4.7) can be rewritten as follows:

$$0 \leq Q_k^{svc} \leq \bar{Q}_k^{svc} = \max(\mathcal{C}_k), \forall k \in \mathcal{N}^{svc}. \tag{4.8}$$

4.3.4 General Form of the OPF Formulation

Considering the objectives and all constraints described above, the OPF formulation in unbalanced distribution systems is given in the following general form:

$$\begin{aligned} &min \quad f(\boldsymbol{X}) && \text{(4.9a)}\\ &s.t. \quad \boldsymbol{g(X)} = \boldsymbol{0}, && \text{(4.9b)}\\ &\qquad \underline{\boldsymbol{h}} \leq \boldsymbol{h(X)} \leq \bar{\boldsymbol{h}}, && \text{(4.9c)}\\ &\qquad \underline{\boldsymbol{X}} \leq \hat{\mathrm{I}}\boldsymbol{X} \leq \bar{\boldsymbol{X}}, && \text{(4.9d)} \end{aligned}$$

In the above formulation, $\boldsymbol{g(X)}$ in (4.9b) is constructed from the power balance equations (4.4). The functional constraint of variables in (4.6) is represented by

$\boldsymbol{h}(\boldsymbol{X})$ in (4.9c). In (4.9d), $\hat{\mathrm{I}}\boldsymbol{X}$ is a sub-vector of $\boldsymbol{X}$ that contains the variables that are imposed by box constraint (4.8). Due to the nonconvex feasible set resulting from (4.6), the optimization problem (4.9) is nonconvex. PCPDIPM is implemented in this paper to solve the formulated nonlinear nonconvex optimization problem. The details of PCPDIPM are described in [51,52]. The technique to induce the convergence of discrete variables is adopted from [50].

4.4 The Proposed Two-stage Optimization for Determination of the Locations and Real-Time Reactive Power Injections from LV-SVCs

The iterative placement algorithm assumes that unlimited number of LV-SVCs can be installed at the transformer secondary node. If the load voltage violations are not removed even after installing an LV-SVC at the corresponding transformer secondary, it is likely that another LV-SVC is placed at the same location in some other iteration during the placement process. In practice, due to space limitation on the service transformer pole, not more than one LV-SVC can be installed on each service transformer secondary. The BPSO algorithm inherently takes this constraint into account by associating only one bit for each LV-SVC location. In the proposed framework, this limitation can be realized by setting an upper bound of 20 kvar on the reactive power injection at each secondary node for each time step.

In the proposed approach, the optimization of LV-SVC locations and their reactive power dispatch are performed in two stages as depicted in

Fig. 4.4. In both stages, the optimization problems share similar decision variables and operating constraints, as discussed in Section 4.3. In the first stage, the objective is to minimize the investment cost per day of the LV-SVCs, as shown in (4.2) to maintain the voltage regulation. Based on the optimal dispatch of LV-SVCs, which is the solution of the first stage, the optimal locations of LV-SVCs are determined. These locations are the input to the second stage, in which the ACOPF is run again to determine the real-time secondary-side reactive power injections in the circuit by LV-SVCs.

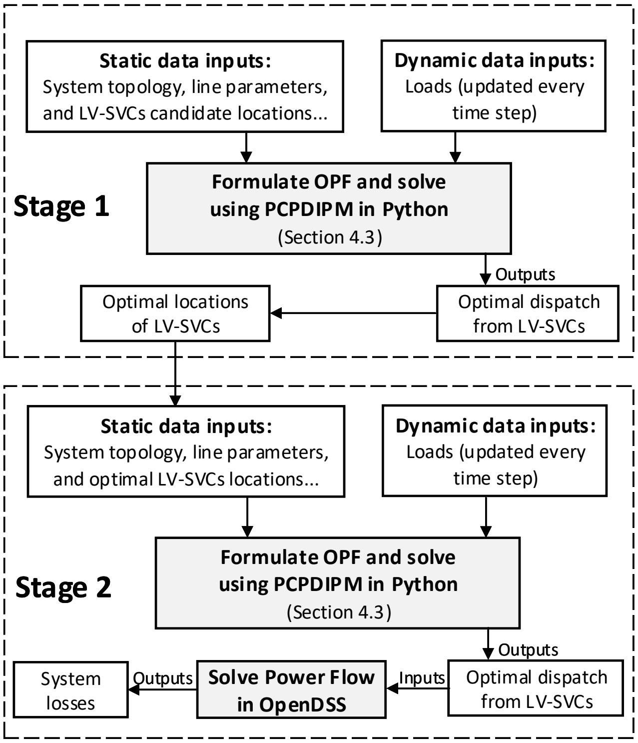

Figure 4.4: Two-stage optimization procedure. For verifying the accuracy of the OPF solutions, optimal dispatch from LV-SVCs is input to OpenDSS simulator [1]. OpenDSS computes system voltages and losses. These outputs are then compared to those determined by the proposed formulation in Section 4.3.

As opposed to the first stage, the objective of the AC OPF problem in the second stage is to minimize the active power losses, as shown in (4.3). The cost of the LV-SVCs is not considered in the objective function in the second stage as these devices, once placed will not incur any additional cost to inject reactive power. The two-stage optimization is performed on Circuit 5 and the results are discussed in the next section.

4.5 Simulation Results of Circuit 5

The scalability and applicability of the proposed two-stage optimization framework for optimal placement and centralized control of LV-SVCs are validated on a large distribution circuit namely Circuit 5. In this section, the circuit's performance with the centralized control of LV-SVCs is compared with that when the LV-SVCs are operated using local autonomous voltage-based controllers.

4.5.1 Placement using BPSO Algorithm

Initially, the LV-SVCs operating with local controllers are installed using the BPSO algorithm discussed in Section 3.2.1. The parameters used for running the BPSO are given in Table 4.1. The cost of energy losses is considered as $W_l = 0.1$ \$/kWh. Assuming a cost of \$2000 for one LV-SVC rated for 20 kvar with an expected service life of 15 years, the associated cost coefficient is determined as $W_{svc} = \$0.365$ per LV-SVC per day. A high value is selected for the weight W_{uv} to obtain a solution with less low voltage violations in the circuit. The BPSO algorithm resulted in placing 24 LV-SVCs. The results of daily QSTS simulation with the LV-SVCs in the circuit are discussed in Section 4.5.3.

Table 4.1: BPSO parameters

Parameter	**Value**
No. of particles	40
No. of iterations	50
BPSO weighing factors	$c_1 = 0.5, c_2 = 1.25$, and ω varies linearly from 0.9 to 0.4
Objective function weights	$W_{uv} = 1000,\ W_{svc} = 0.1,\ W_l = 0.365$

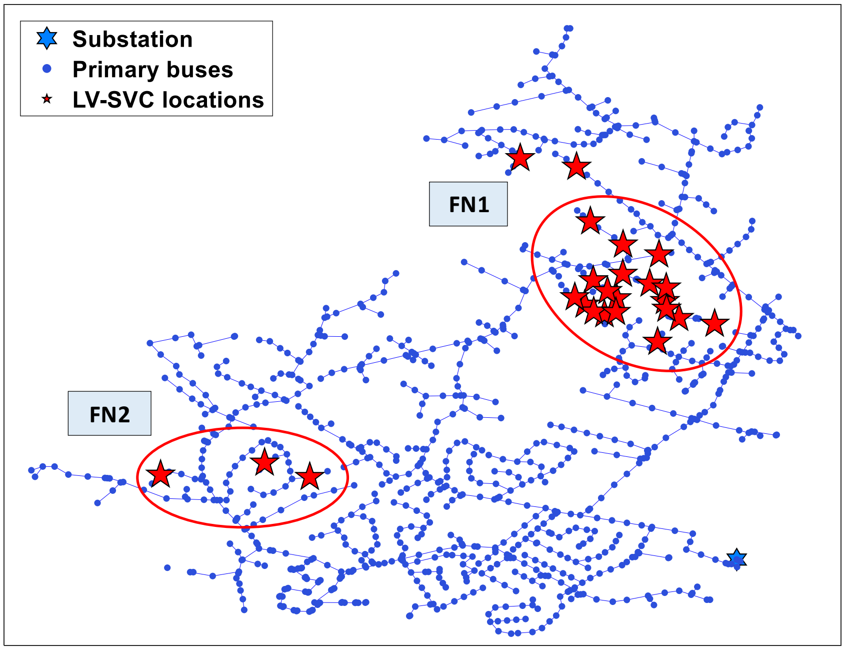

Figure 4.5: Locations of LV-SVCs using BPSO algorithm.

4.5.2 Optimal Placement and Centralized Control using ACOPF

In the proposed approach, the optimal locations and reactive power injections by the LV-SVCs are determined in two stages. In the first stage, the optimal locations of LV-SVCs are identified by running the ACOPF with the reactive power injection at all the secondary nodes as decision variables and objective function as given in (4.2). There are 591 secondary nodes corresponding to 591 service transformers in Circuit 5. The ACOPF is run for 24 time steps considering the variations in the load demand at each hour of the simulated day. Assuming a service life of 15 years, the coefficient α_1 is computed as 0.00765 \$/kvar/hour for the ACOPF in this stage. The total reactive power injection by the LV-SVCs (in kvar-h) installed at different nodes over the simulated peak day obtained from the ACOPF results is shown in Fig. 4.6. There are 27 secondary nodes in total where reactive power injection is needed to minimize the active power losses in the circuit while maintaining the load voltages within limits.

In the second stage optimization, the optimal outputs of the 27 LV-SVCs at each time step are determined by running the ACOPF again. Note that only the cost associated with the active power losses is minimized in determining the reactive power injections in this stage. The cost of energy loss is considered as $\alpha_2 = 0.1\$/\text{kWh}$. The geographic locations of the LV-SVCs in the circuit are highlighted with stars in Fig. 4.7. The color of the stars represents the amount of reactive power supplied by the LV-SVC installed at that location during the simulated day. It is observed that most of the reactive

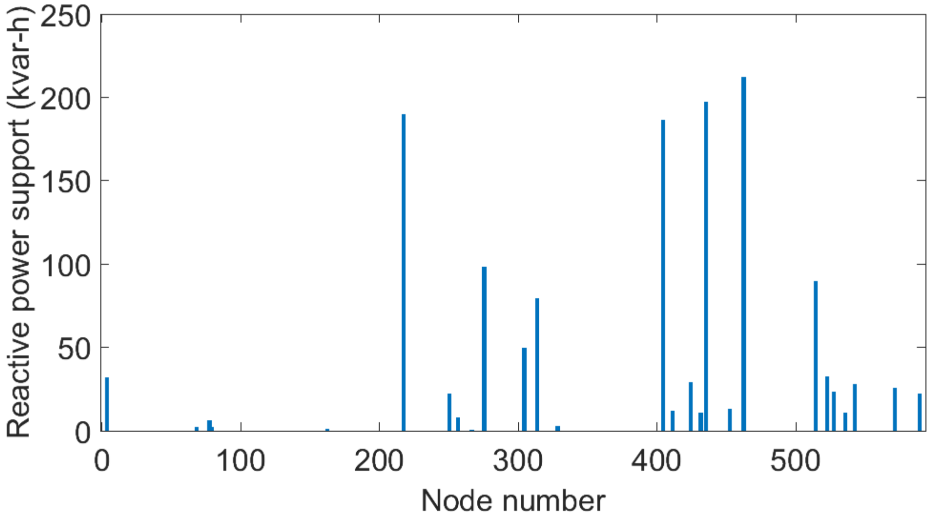

Figure 4.6: Reactive power injection obtained from first-stage optimization.

power injection is needed in the feeder neighborhood FN1. As noted in [31], this is the feeder neighborhood experiencing lower supply voltages compared to the other parts of the circuit. As a result, more capacitive reactive power support is needed in FN1 in a more distributed way compared to FN2. There are three additional LV-SVCs required in the circuit apart from those installed in FN1 and FN2 as highlighted in Fig. 4.7.

The active and reactive power demands at the substation and the total reactive power injection by all the LV-SVCs during the simulated day are shown in Fig. 4.8. During the initial few hours of the day, reactive power is not drawn from the LV-SVCs. As the load level increases, more reactive power is needed after hour 4 which is provided by these devices. Maximum reactive power of 423 kvar is supplied by all the LV-SVCs at the peak loading condition at hour 17.

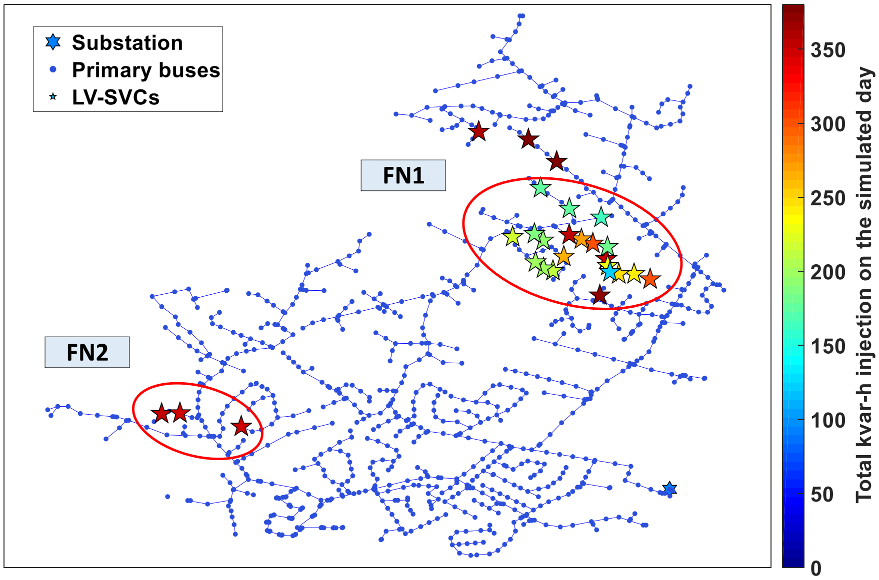

Figure 4.7: Optimal locations and reactive power injections of LV-SVCs.

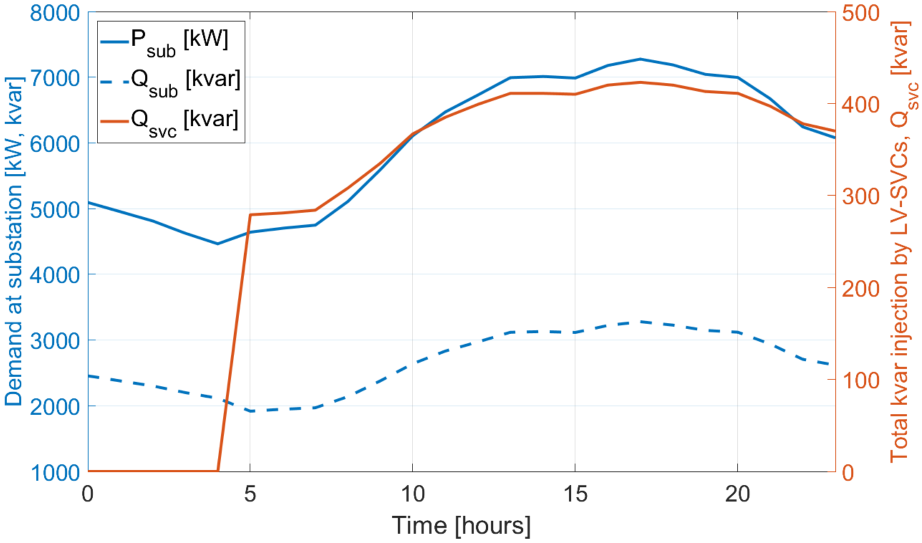

Figure 4.8: Active and reactive power demands at substation and total reactive power injection by LV-SVCs during simulated day.

4.5.3 Comparison of Results

The minimum load voltage and the active power losses in the circuit on the simulated day are compared for the following five scenarios:

1) Base case: No LV-SVCs are present in the circuit.

2) BPSO placement with a voltage setpoint, Vsp=0.95 pu: The LV-SVCs are placed using the BPSO, the LV-SVCs are set to regulate their node voltages at 0.95 pu using local autonomous controllers.

3) BPSO placement, Vsp=1.0 pu: The LV-SVCs in the previous scenario are set to regulate the node voltage at 1.0 pu.

4) BPSO placement, Vsp=1.05 pu: The LV-SVCs in the previous scenario are set to regulate the node voltage at 1.05 pu.

5) ACOPF placement and dispatch: The LV-SVCs are placed and dispatched using the proposed two-stage optimization approach.

The minimum load voltage in the circuit for all these scenarios is shown in Fig. 4.9. It is below the lower ANSI limit of 0.95 pu in the base case for several hours during the simulated day which is not acceptable. This voltage is maintained at or above 0.95 pu throughout the day in all the other scenarios. The maximum voltage in the circuit in all the scenarios is found to be approximately the same and is below the 1.05 pu upper ANSI limit. The voltage regulation is accomplished in all the scenarios other than the base case due to the reactive power injection by the LV-SVCs. Furthermore, the minimum load voltage is well above the 0.95 pu when higher voltage setpoints are used for the LV-SVCs. The results show that when the voltage regulation is the primary objective, both the BPSO placement and ACOPF placement work well.

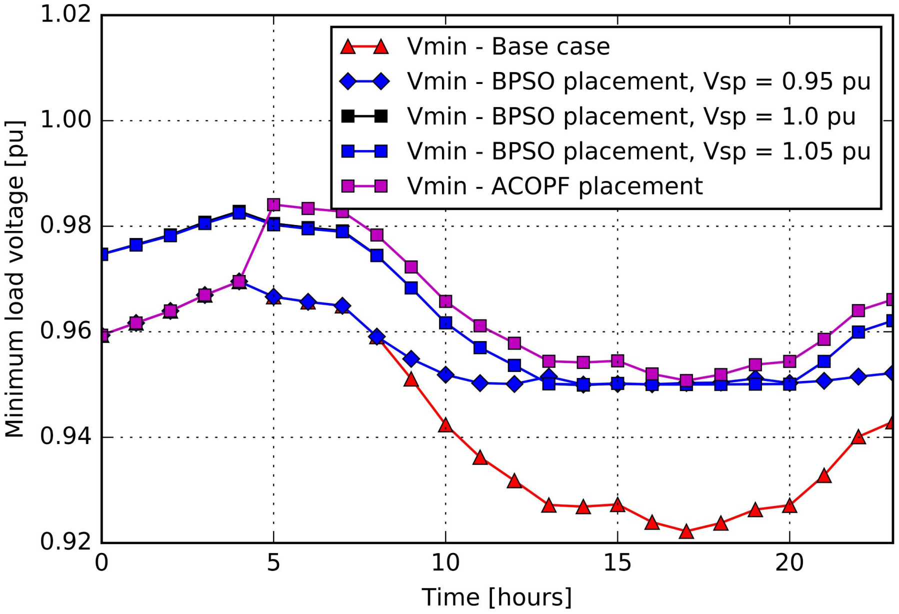

Figure 4.9: Minimum load voltage during the simulated day in different scenarios.

The active power loss in the circuit in each scenario during the simulated day is shown in Fig. 4.10. The active power loss is higher in the base case due to the lack of reactive power sources in the circuit in this scenario. The total energy loss on the simulated day in the base case is 4,883 kWh as shown in Table 4.2. When the LV-SVCs are supplying reactive power using the local voltage-based control with voltage setpoints 0.95 pu, 1.0 pu, and 1.05 pu, the active power loss is reduced by 1.5%, 2.63%, and 2.46% respectively compared to the base case due to the supply of reactive power to the loads experiencing low voltages. The total energy loss is the lowest at 4,736 kWh when the centralized optimal control is used for the LV-SVCs as the reactive power injections in this scenario are optimized to minimize the losses while maintaining the voltage regulation. This is 3.07% reduction compared to the base case.

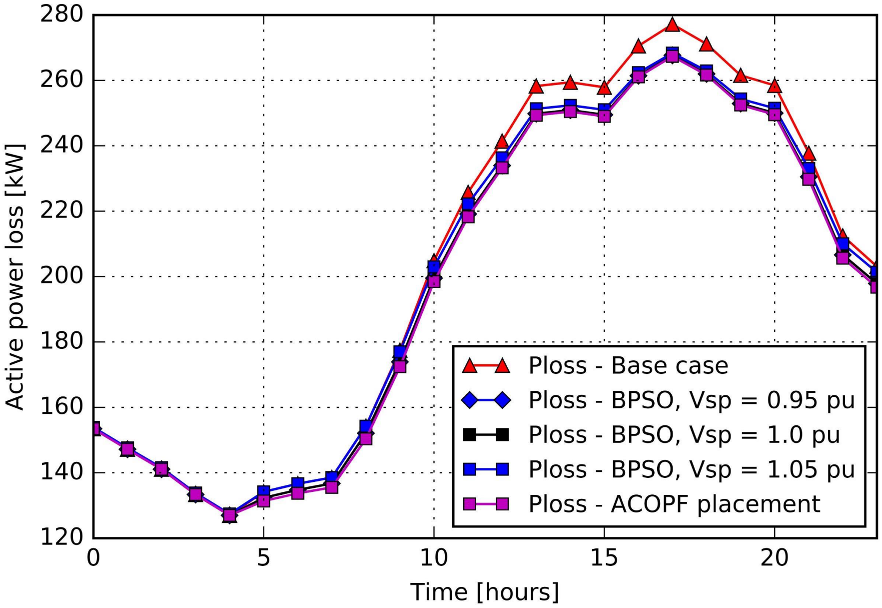

Figure 4.10: Active power loss in the circuit during the simulated day.

In the approach described in Section 4.3, the LV-SVC placement was done to perform voltage regulation while minimizing the device installation cost in the first stage. The installed LV-SVCs are then utilized to minimize the active power losses as well while maintaining the voltage regulation in the second stage optimization. However, the energy losses can be further minimized by considering the active power losses in the objective function in the

Table 4.2: Summary of QSTS results

Scenario	**No. of SVCs**	**Voltage violations**	**Energy loss**	**Reduction**
Base case	0	Yes	4,883 kWh	-
BPSO placement, Vsp = 0.95 pu	24	No	4,802 kWh	1.5%
BPSO placement, Vsp = 1.0 pu	24	No	4,754 kWh	2.63%
BPSO placement, Vsp = 1.05 pu	24	No	4,762 kWh	2.46%
ACOPF placement & control	27	No	4,736 kWh	3.07%

first stage itself. When both the objectives (4.2) and (4.3) are considered in the first stage optimization, the results show that 74 LV-SVCs are required in the circuit to further minimize the power losses. In the second stage optimization, the optimal reactive power injections from the 74 LV-SVCs are computed at each time step for the centralized control. The active power losses in the circuit obtained from the daily QSTS results when the centralized control is applied on the 74 LV-SVCs, when they are operated with the local voltage-based controllers with the voltage setpoints of 0.95 pu, 1.0 pu, and 1.05 pu are shown in Fig. 4.11. The summary of QSTS results is given in Table 4.3. It is observed that the energy losses are lowered when the LV-SVCs are operated with higher voltage setpoints in local control mode. As the voltage setpoints of the LV-SVCs are increased, they supply more reactive power in order to maintain the higher node voltages. This additional reactive power compensates for the load reactive power requirement. Furthermore, as the node voltage is increased, the loads (modeled as constant power) draw less current, leading to lower losses in the associated lines upstream. The reductions in the energy loss compared to the base case are 1.37%, 6.7%, and 6.35%, when voltage setpoints are 0.95 pu, 1.0 pu, and 1.05 pu, respectively. The higher voltage setpoints lead to the injection of higher amount of reactive power for a given measured voltage, resulting in lower active power losses. The energy losses are observed to be the lowest at 4,540 kWh with the centralized optimal control which is 7% reduction compared to the base case. This reduction is marginal compared to the case when the 74 LV-SVCs are operated on local control mode with 1.0 pu voltage setpoint. Therefore, when the centralized control is not available, the LV-SVCs can be operated on local control mode with higher voltage setpoints to obtain lower energy losses. The voltage violations are not present in any of these scenarios, except the base case as shown in Fig. 4.12.

Table 4.3: Summary of QSTS results

Scenario	**No. of SVCs**	**Voltage violations**	**Energy loss**	**Reduction**
Base case	0	Yes	4,883 kWh	-
ACOPF placement with local control, Vsp = 0.95 pu	74	No	4,815 kWh	1.37%
Local control, Vsp = 1.0 pu	74	No	4,554 kWh	6.7%
Local control, Vsp s= 1.05 pu	74	No	4,572 kWh	6.35%
ACOPF placement & centralized control	74	No	4,540 kWh	7%

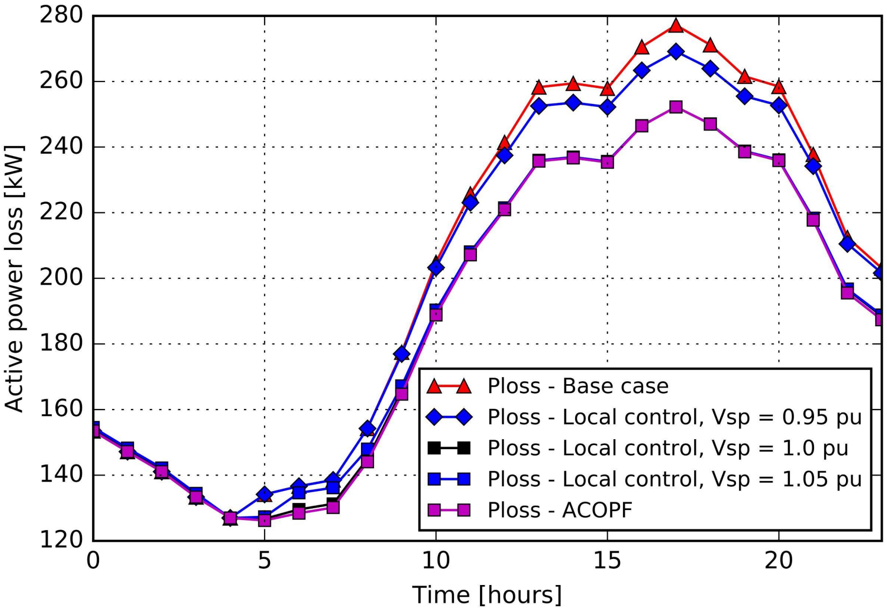

Figure 4.11: Active power loss during the simulated day when 74 LV-SVCs are installed.

4.5.4 Convergence of the PCPDIPM

The PCPDIPM algorithm used to solve the problem formulated in Section 4.3 is implemented in Python on an Intel Core i7-6700 with 32GB RAM. The algorithm converges in both stages and in all time steps. In the first stage, the running time is approximately 1.8 minutes for one time step. In the second stage, in which the number of locations of LV-SVCs are significantly lower, the running time is approximately 1.1 minutes for one time step. Besides the benefits described in Section 4.5.3, such rapid and robust convergence indicates that the proposed formulation and solution approach are also suitable for real-time applications.

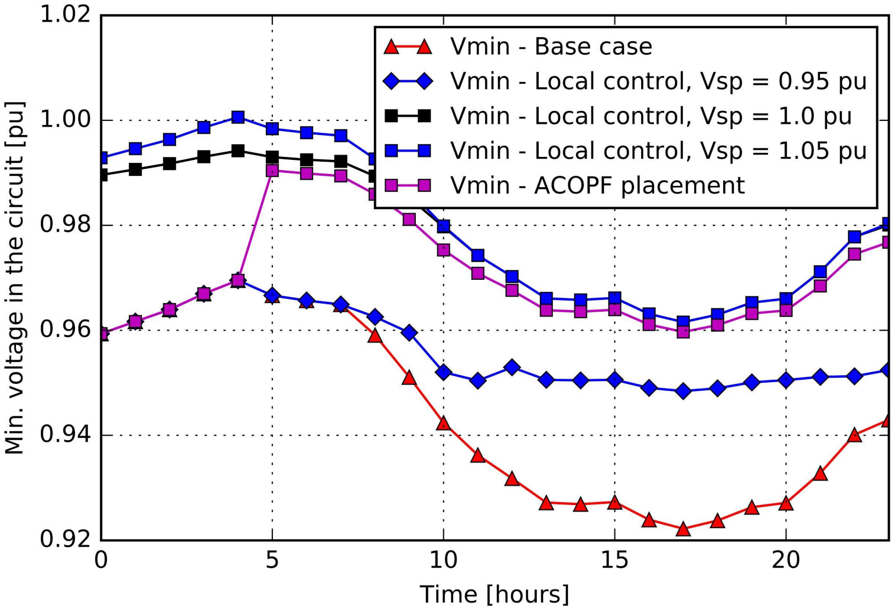

Figure 4.12: Minimum load voltage during the simulated day in different scenarios.

4.6 Summary

In this chapter, a two-stage optimization framework for optimal placement and centralized control of low-voltage SVCs in distribution circuits is proposed. The proposed approach leverages the data available from AMI, communication capabilities of LV-SVCs, allows incorporation of physical constraints of space limitations on the transformer poles, and is scalable for application to large unbalanced distribution networks. The proposed approach provides global optimal locations for the LV-SVCs considering voltage regulation and active power loss in a reasonable computational time. Additionally, we can also apply a centralized control on the LV-SVCs to control their real-time outputs optimally to minimize the active power losses. The advantages of optimal placement and centralized control of LV-SVCs is studied by comparing it with the performance achieved by local voltage-based control of LV-SVCs with varied voltage setpoints installed using BPSO technique in Circuit 5. The results show that, when the voltage regulation is the only objective, both BPSO and ACOPF-based placement algorithms are effective in selecting the best locations for the LV-SVCs. However, the energy losses can be lowered significantly when the centralized optimal control is implemented on the LV-SVCs. Furthermore, from the voltage setpoint analysis, it is found that higher voltage setpoints such as Vsp = 1 pu can be used and the SVCs can be operated on distributed control to obtain power loss reduction similar to when a centralized optimal control is applied on them.

Chapter 5

PV Smart Inverter Control Tuning for Voltage Regulation at Grid-Edge

Interconnections of small- and large-scale solar photovoltaic (PV) systems to the distribution system are growing at a rapid pace. Their penetration levels are often limited by the distribution utilities because of the adverse impacts on various distribution operating parameters, specifically steady-state and transient voltage rise. Inverters used for the solar PV can be used to absorb or inject reactive power to mitigate the impacts of their real power injection on the distribution system voltages. Such active voltage regulation by the PV was not allowed by the standards in the past [13]. However, the recent amendment of IEEE 1547 standard [29] permits the voltage regulation by PV using controlled var injection. As a result, the PV smart inverters form another control handle to improve the voltage regulation at grid-edge.

[1]This chapter focuses on tuning the control settings of PV smart inverters for voltage regulation and smoothing. The PV smart inverters can have beneficial effect on the distribution grid only when appropriate control

---

[1] Parts of this chapter appear in the published paper, 'H. V. Padullaparti, N. Ganta, and S. Santoso, "Voltage Regulation at Grid Edge: Tuning of PV Smart Inverter Control," *IEEE Power and Energy Society T&D Conference & Exposition*, Denver, CO, Apr. 2018'. The author of this dissertation contributed all the sections in this paper as first author.

settings are implemented. Studies have shown that when wrong settings are chosen, the PV smart inverters can actually worsen grid performance beyond that seen if the PV is operating at unity power factor [54]. However, the determination of appropriate PV smart inverter settings is a complex process as numerous settings are possible to implement on a smart inverter and the feeder response to a given setting depends upon a wide variety of parameters such as the feeder characteristics, loading condition, PV size, and PV location [30]. In this chapter, a procedure to tune the PV smart inverter settings by grouping the PVs in the feeder neighborhoods experiencing undervoltages is proposed for voltage regulation. The performance of the tuned PV smart inverter settings is compared to that of the settings recommended in [30,32] using voltage range and voltage variability indices. The results show that, implementation of the tuned settings is very effective leading to the reduction of voltage range by 64% and variability index by 82.5% compared to the unity power factor inverter setting in the studied circuit.

5.1 Distribution Circuit Details

One of the standard distribution test circuit models developed by EPRI namely ‘Circuit 5’ is used in this study. The one-line diagram of the circuit, generated using Sandia GridPV tool [47], is shown in Fig. 5.1. This circuit has a 115/12.47 kV, 10 MVA substation transformer with a peak load demand of 8.12 MVA. Four three-phase switched capacitors are installed along the feeder as highlighted in Fig. 5.1 for both voltage regulation and power factor correction. Mid-line voltage regulators are not available in this circuit.

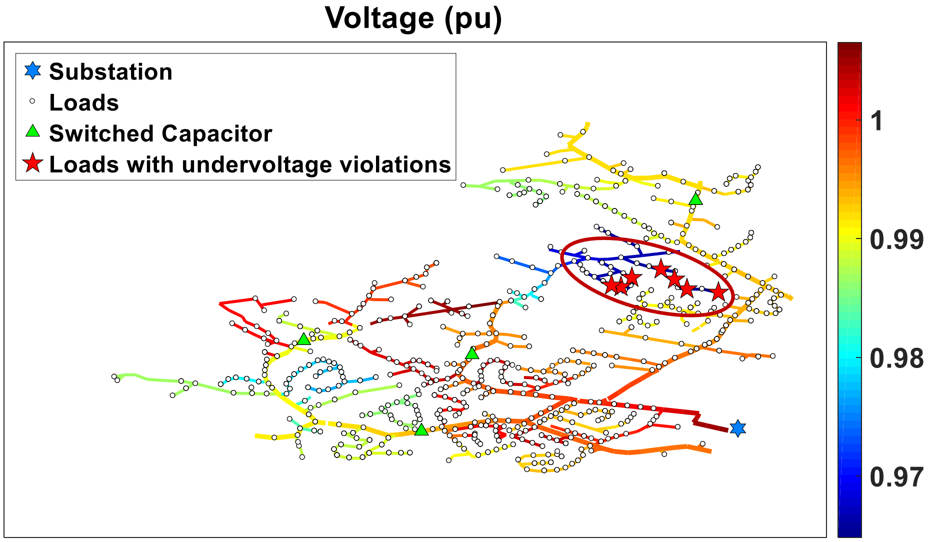

Figure 5.1: One-line diagram of the distribution circuit.

The feeder voltage profile at the peak load snapshot simulation with a source voltage of 1.025 pu is shown in Fig. 5.2. In this figure, the primary bus voltages are represented by solid lines and the secondary node voltages are represented by dashed lines. All the capacitors are in service in this condition. It is observed that many loads on phase B experience undervoltage violations, i.e., voltages lower than 0.95 pu at the peak load snapshot. There are 24 loads in total that experience undervoltage violations. The primary buses of these loads are marked with red stars in Fig. 5.1 and the feeder neighborhood within which these loads are connected is encircled. Note that there are only 7 primary 12.47 kV buses associated with these 24 loads. From these 7 buses, the 24 loads are connected on the 120V/240 V secondary network via service lines and service transformers. In Fig. 5.1, the colors of the distribution lines are contoured in accordance with the voltage experienced by that line at the peak load snapshot.

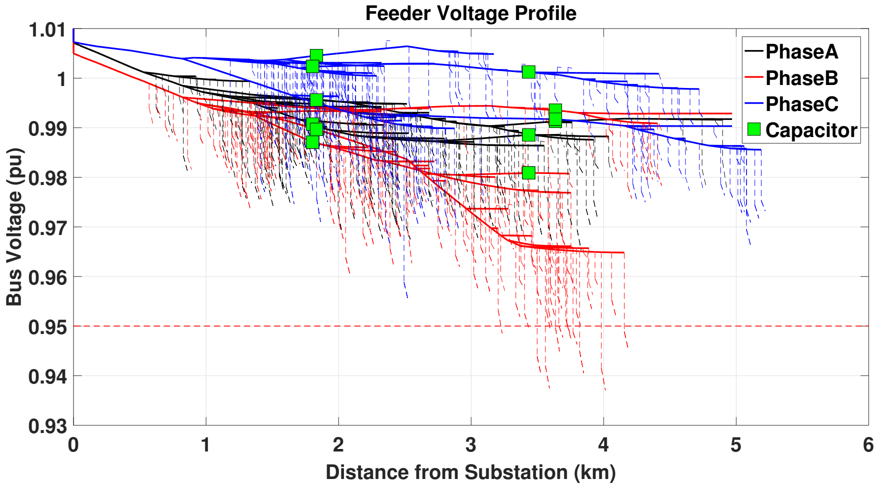

Figure 5.2: Feeder voltage profile at peak load.

5.2 Analysis of the Voltage Impact of PV within a Feeder Neighborhood

To demonstrate the benefits of employing PV smart inverters, 24 PVs are installed at the load locations experiencing undervoltage violations. The PV sizes are same as that of the loads connected at these 24 locations, with an aggregated size of 184 kW. Note that the loads with undervoltage violations and consequently, the locations of PV systems are segregated within the feeder neighborhood encircled in Fig. 5.1.

The analysis presented in this section shows that the impact of reactive power injection by PVs located within a given feeder neighborhood does not vary much for reasonable sizes of PV systems. Thus, customized settings for each individual PV is not required. A common setting can be supplied to all the PVs within a feeder neighborhood which then can be tuned to obtain effective voltage regulation performance.

To analyze the impact of PV on system voltage, consider a PV system connected to the secondary circuit of a distribution grid. The Thevenin equivalent circuit at the point of interconnection (POI) of the PV on the secondary is shown in Fig. 5.3. In this figure, the voltage source, equivalent system resistance and reactance are represented by V_s, R, and X, respectively. The values of these parameters at the PV locations in a given circuit can be obtained from the short-circuit simulation study.

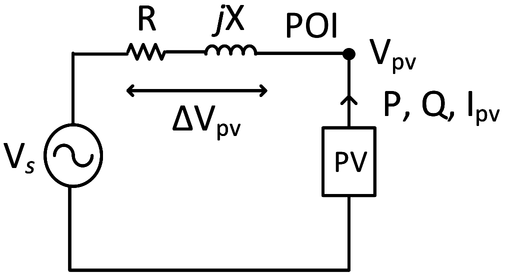

Figure 5.3: Thevenin equivalent circuit at the POI of the PV system.

The PV injects active power (P) and reactive power (Q) at the POI. The associated voltage change across the Thevenin impedance (ΔV_{pv}) can be calculated as:

$$I_{pv} = \frac{P - jQ}{V_{pv}^*} \tag{5.1}$$

$$\Delta V_{pv} = \frac{1}{V_{pv}^*}[(RP + XQ) + j(XP - RQ)] \tag{5.2}$$

Since the reactive part of the voltage rise is negligible compared to the real part, the reactive term of (5.2) can be neglected [55]. Additionally, since the voltage phase shift at the POI with respect to the source voltage is negligible [55], the voltage at the POI can be approximated to be the same as its compliment. Thus, (5.2) can be revised as

$$\Delta V_{pv} = \frac{RP + XQ}{V_{pv}}; \quad \Delta V_{pu} = \frac{\Delta V_{pv}}{V_{base}} \tag{5.3}$$

where ΔV_{pu} is the voltage rise expressed in per unit and V_{base} is the nominal bus voltage.

The key influencing factors that determine the voltage impact due to power injections from the PV are highlighted in (5.3). They are the distribution system impedance at POI (R, X) and the PV parameters (P, Q). In general, the distribution system impedances at the buses within a given feeder neighborhood do not vary much. The impedance is lowest at the substation and increases as we move farther away from the substation along the feeder. Fig. 5.4 shows the variation of system resistance and reactance in a distribution circuit. In this figure, the line colors are contoured according to the short-circuit resistance (R) and reactance (X). It is evident that, within a given feeder neighborhood, the resistance and reactance parameters have similar values. As such, all the PVs which are close to one another, in particular, those installed in the encircled region in Fig. 5.1, observe a similar impedance from the system that affects the voltage change due to PV (ΔV_{pv}).

The ΔV_{pv} also depends upon the real and reactive power injections from the PV which in turn depend upon the PV size. The sizes of residential PV

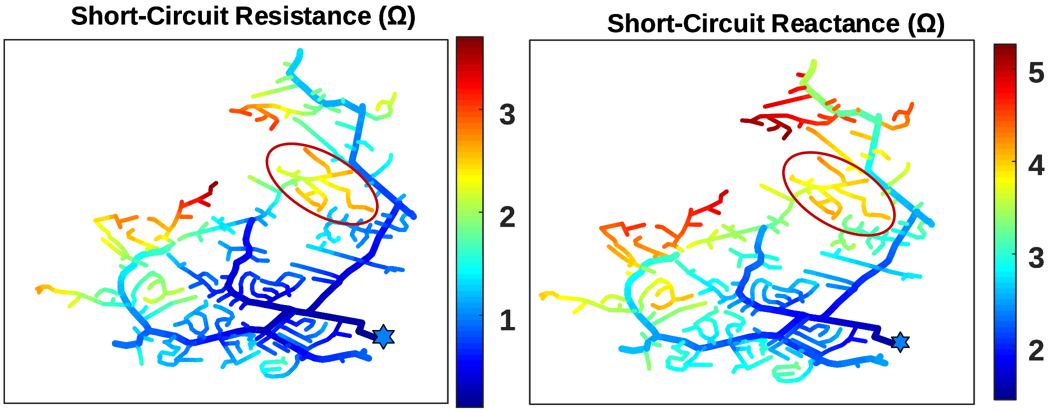

Figure 5.4: Variation of system impedance.

systems can vary from 2 kW to 10 kW [56]. The size distribution of the 24 PV systems, which range between 4.84 kW and 9.71 kW, is shown in Fig. 5.5. Additionally, from the short-circuit study results of Circuit 5, it is observed that the equivalent system resistance at the POI ranges between 44.06 Ω and 56.05 Ω whereas the equivalent system reactance ranges between 36.83 Ω and 50.73 Ω.

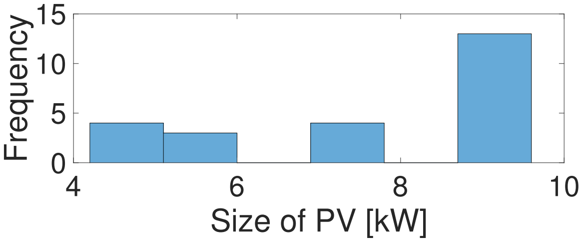

Figure 5.5: PV size distribution.

The quantitative analysis of extremes of the voltage change due to the PV real power injections at the lowest and highest system equivalent impedances with a base system voltage of 7.2 kV_{LN} is given below.

$$\Delta V_{pu,min\_P} \cong \frac{44.06\ (\Omega) \times 4.84\ (kW)}{7.2\ (kV) \times 7.2\ (kV)} = 0.0041 \text{ pu}$$

$$\Delta V_{pu,max\_P} \cong \frac{56.05\ (\Omega) \times 9.71\ (kW)}{7.2\ (kV) \times 7.2\ (kV)} = 0.0106 \text{ pu}$$

where $\Delta V_{pu,min\_P}$ and $\Delta V_{pu,max\_P}$ are the anticipated voltage changes due to minimum and maximum real power injections from the PV.

Similarly, considering the PV smart inverter kVA rating as 1.1 times its maximum real power rating, the anticipated extremes of voltage change due to the PV reactive power injection can be calculated as $\Delta V_{pu,min\_Q} = 0.0038$ pu and $\Delta V_{pu,max\_Q} = 0.0104$ pu. It can be observed that the impact of power injections on voltage for the residential PV did not vary much within the selected feeder neighborhood. As such, customized smart inverter settings for such systems is not required. A common setting can be applied to all of them. Along the same lines, it can be shown that even for commercial PV installations with sizes up to several tens of kW installed in a given feeder neighborhood, customized smart inverter settings are not required as the associated impact does not vary much among them.

$$\Delta V_{pu,min\_Q} \cong \frac{36.83\ (\Omega) \times 5.32\ (kvar)}{7.2\ (kV) \times 7.2\ (kV)} = 0.0038 \text{ pu}$$

$$\Delta V_{pu,max\_Q} \cong \frac{50.73\ (\Omega) \times 10.68\ (kvar)}{7.2\ (kV) \times 7.2\ (kV)} = 0.0104 \text{ pu}$$

5.3 PV Smart Inverter Control Modes and Performance Metrics

Two smart inverter control modes namely volt-var control (VVC) and dynamic reactive current control (DRCC) useful for performing voltage regulation are considered in this work for smart inverter control tuning.

5.3.1 Volt-var Control (VVC) Mode

The volt-var control (VVC) mode facilitates the smart inverter of a PV to inject reactive power in response to its terminal voltage and a preset volt-var control curve. The volt-var curve proposed in [30,32] to be the default setting for PV smart inverters is shown in Fig. 5.6. In some cases, it may be useful to employ a hysteresis in the volt-var settings. Hysteresis helps maintain the reactive power output from the PV smart inverter for a band of voltage levels. The key parameters in defining a VVC curve that could result in best possible voltage regulation performance are (a) Slope of the curve (b) Hysteresis (c) Deadband.

5.3.2 Dynamic Reactive Current Control (DRCC)

The DRCC mode is useful in mitigating the fluctuations in the system voltage [30]. The functionality in this mode is different compared to the VVC mode, in that the controlling parameter is the change in voltage rather than the voltage level itself. Unlike the VVC mode, the reference voltage in this mode is not fixed, but is a moving average of PV voltage measurements for a preset window length. The key parameters of smart inverter settings in this

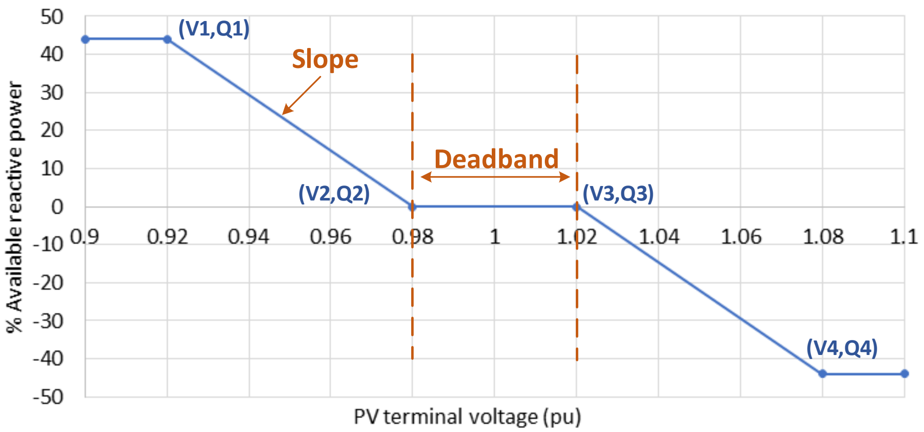

Figure 5.6: Default volt-var control (VVC) curve.

mode are (a) Curve slope (b) Average window length (AWL) (c) Deadband.

The DRCC mode is useful in mitigating the fluctuations in the system voltages. The PV smart inverter operation in DRCC control mode can be described using Fig. 5.7. The functionality in this mode is different compared to the VVC mode, in that the controlling parameter is the change in voltage rather than the voltage level. Unlike the VVC mode, the reference voltage in this mode is not fixed, but is a moving average of PV voltage measurements for a preset window length. The key parameters of smart inverter settings in this mode are (a) Curve slope (b) Average window length (AWL) (c) Deadband.

5.3.3 Performance Metrics: Voltage Range and Variability Index

To quantify the effectiveness of a given PV smart inverter control setting, two metrics namely voltage range and voltage variability index are used in this study. The voltage range at a PV terminal is the difference between

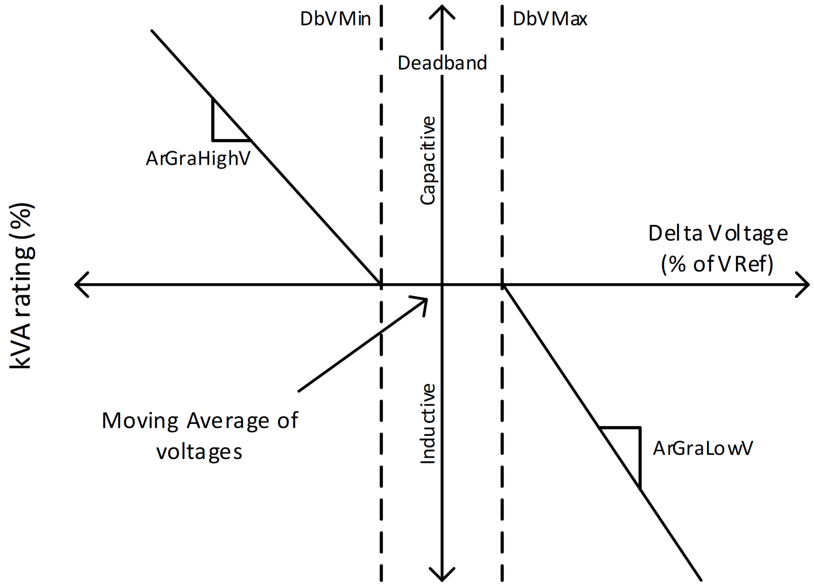

Figure 5.7: Illustration of DRCC control mode.

the maximum and minimum voltages observed at the PV terminal during the selected quasi-static time series (QSTS) simulation period (peak day in this study). This metric is useful in quantifying the improvement in the steady-state voltage variation. Thus, it is used to assess the effectiveness of volt-var control settings.

$$\text{Voltage range} = V_{max} - V_{min} \tag{5.4}$$

To quantify the level of voltage smoothing, i.e., reduction of voltage fluctuations for a given DRCC setting, variability index (VI) is used. The variability index, calculated using (5.5), is a modification of solar variability index used to classify solar generation [57].

$$\text{Variability index, VI} = \sum_{k=2}^{n} |V_k - V_{k-1}| \tag{5.5}$$

where 'n' is the total number of voltage samples, V_k is the PV terminal voltage at k^{th} sample.

5.4 PV Smart Inverter Control Tuning and Results

In this section, the PV smart inverter control tuning procedure in both VVC and DRCC modes is presented. The performance of the resulting settings is compared with that of the settings recommended in literature.

5.4.1 Tuning of Volt-Var control (VVC) settings

A PV profile having moderate power output variabilities, as shown in Fig. 5.8, is assumed for all the 24 PVs in the circuit for the QSTS simulation. Furthermore, all the PVs are considered to be equipped with smart inverters. Five VVC curves with different slope settings are defined as shown in Fig. 5.9a. For each of these curves, the hysteresis (hyst) setting is varied from -0.01 pu to -0.05 pu in steps of -0.01 pu. The VVC curve 5 with various hysteresis settings is shown in Fig. 5.9b. Note that the PVs do not inject any reactive power in the deadband region. As such, the deadband does not influence the voltage range. Thus, the deadband is not used in the tuning of the VVC settings. Peak day QSTS with 1-minute resolution is performed for each variation of VVC curve slope and hysteresis settings and the resulting voltage range is plotted as shown in Fig. 5.10. As the voltage observed at all the 24 PV locations is approximately the same, the voltage range measured at one PV location is used for plotting. The results show that, VVC settings with aggressive slope and zero hysteresis settings result in low voltage ranges. Thus, the VVC curve 5 with zero hysteresis, as given in Table 5.1, is the recommended setting for the residential PVs in the selected feeder neighborhood in Circuit 5.

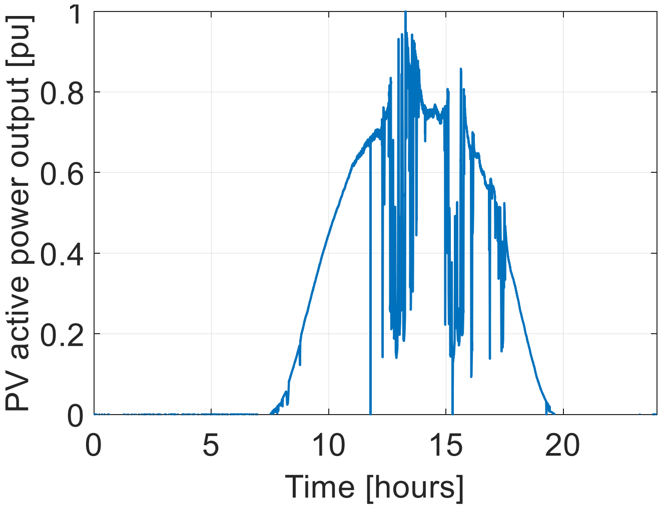

Figure 5.8: Selected PV profile.

Table 5.1: Tuned VVC Curve Settings

VVC Curve	V_1	Q_1	V_2	Q_2	V_3	Q_3	V_4	Q_4
VVC Curve 5	0.8	1	0.975	1	1.025	-1	1.2	-1

5.4.2 Tuning of DRCC settings

The DRCC settings can be tuned on the basis of the resulting voltage variability index (VI) from the peak day QSTS simulation. For this pro-

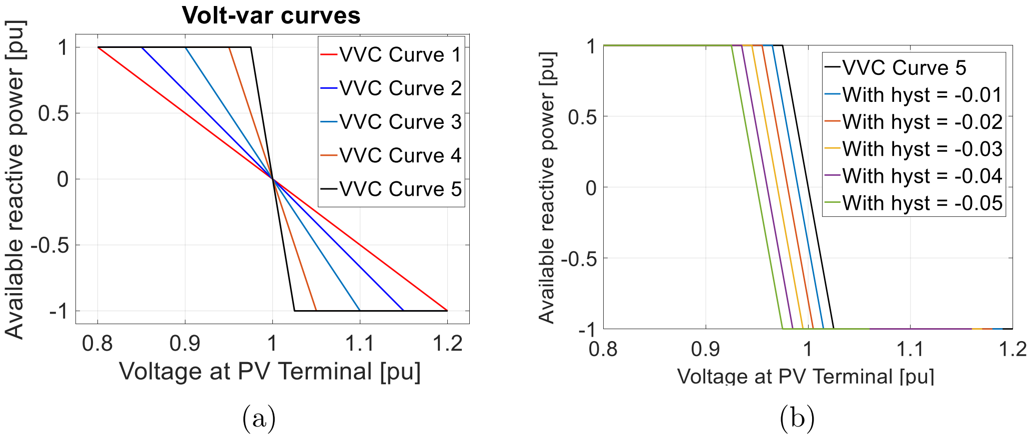

(a) (b)

Figure 5.9: (a) Volt-var control curves with varied slopes (b) VVC Curve 5 with varied hysteresis settings.

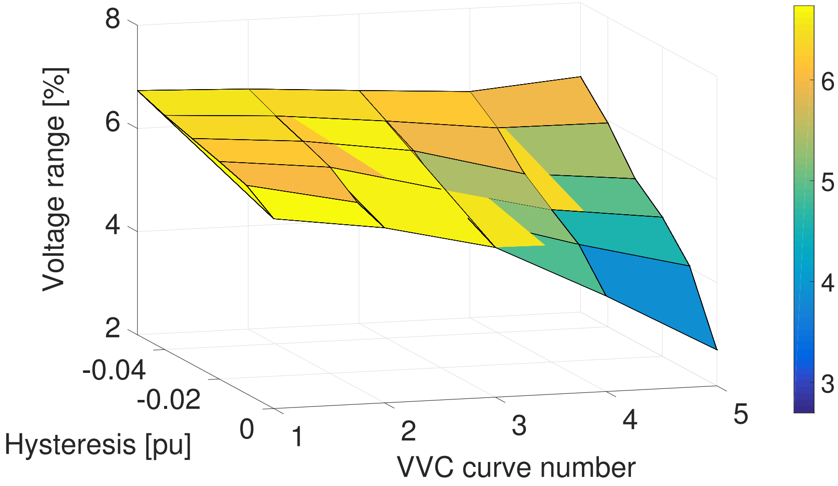

Figure 5.10: Voltage range for varied VVC settings.

cess, the DRCC curves with varied slope settings and average window lengths (AWL) are defined initially. These settings are then assigned to all the 24 PVs and peak day QSTS is performed for each DRCC setting. The resulting VI is plotted as shown in Fig. 5.11. The results show that, the VI becomes lower as the DRCC curve slope and the average window lengths are increased. The sensitivity of the VI to the DRCC curve slope is higher than that to the AWL. Based on the results, the DRCC curve slope of 80 with moderate AWL of 60 minutes, as given in Table 5.2, is the recommended setting for the 24 PVs in the DRCC mode.

Table 5.2: Tuned DRCC Curve Settings

Parameter	**Setting**
Slope	80 (1% of voltage deviation from average value will result in 80% change in the reactive power injection)
Average window length	60 minutes

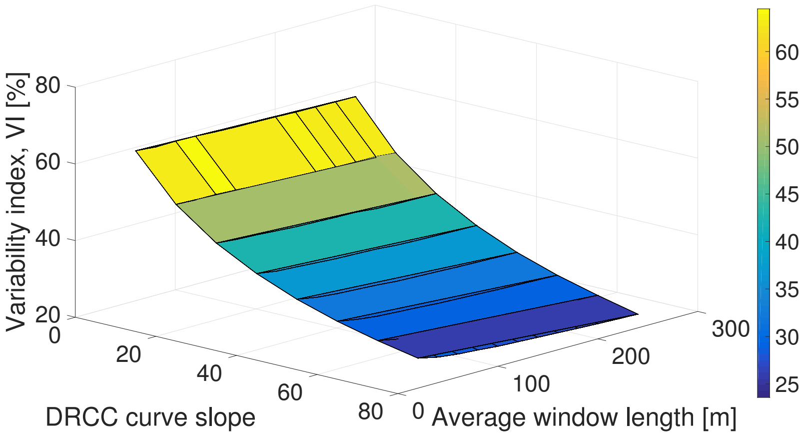

Figure 5.11: Variability index for varied DRCC settings.

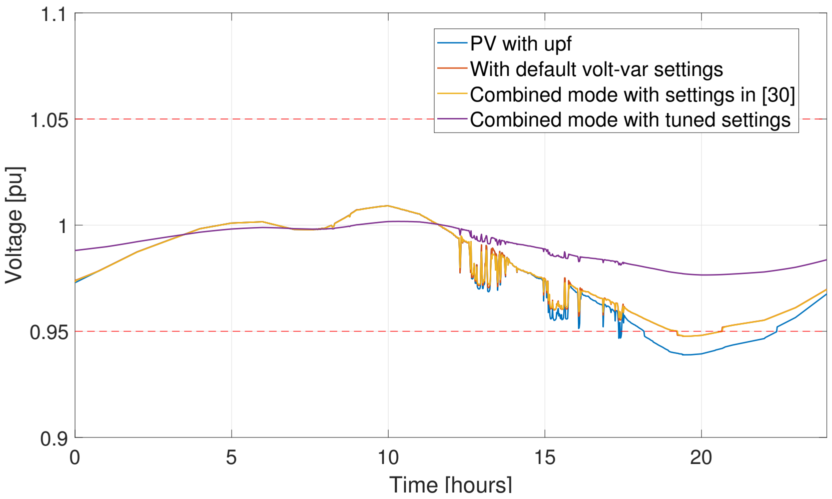

Figure 5.12: Voltage at the selected PV terminal during peak day.

5.4.3 Performance study

To study the voltage regulation performance of the tuned smart inverter settings, four scenarios are considered. In scenario 1, all the PVs are assumed to inject power at unity power factor. In scenarios 2 and 3, the default volt-var settings and the combined mode settings proposed in [30], respectively are used. In the combined mode, the PV smart inverters perform both VVC and DRCC functions simultaneously to reduce voltage range and voltage variability. In scenario 4, the combined volt-var and DRCC mode with the tuned settings given in Tables 5.1 and 5.2 are used. The voltage at the selected PV location obtained from the peak day QSTS is shown in Fig. 5.12. The voltage range and the voltage variability indices computed for these PV voltage plots are given in Table 5.3. From Fig. 5.12 and Table 5.3, it is clear that the voltage profile is very much improved in terms of low voltage range and variability index, when the PVs are operating in the combined mode with the tuned smart inverter settings (scenario 4). In particular, the tuned smart inverter settings used in scenario 4 reduced the voltage range by 64% and the variability index by 82.5% compared to the unity power factor inverter setting in scenario 1. Furthermore, from the feeder voltage profile at the peak load snapshot when the PVs configured with the settings of scenario 4, shown in Fig. 5.12, it is evident that there are no undervoltage violations in the circuit. This is further confirmed from the peak day QSTS simulation results.

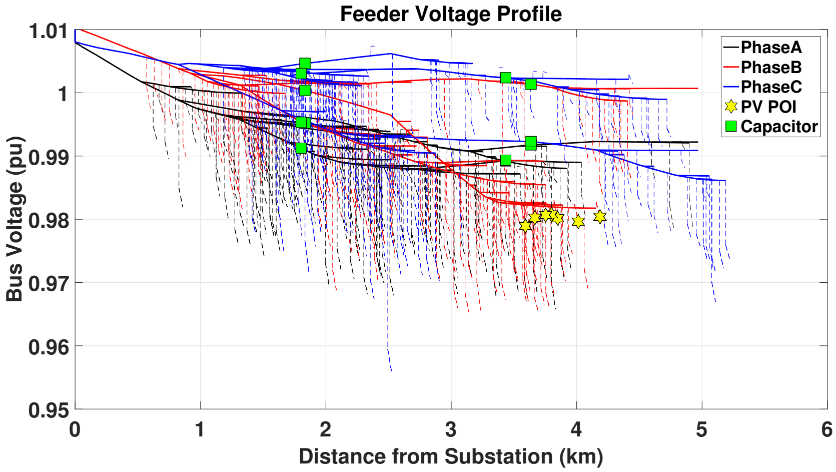

Figure 5.13: Voltage profile at peak load snapshot with PVs using tuned settings.

Table 5.3: Performance Comparison

Scenario	**Voltage range**	**Variability index (VI)**
1. Unity power factor	7.02 %	76.32 %
2. Default volt-var	6.15 %	65.7 %
3. Combined mode with settings in [30]	6.14 %	56.16 %
4. Combined mode with tuned settings	2.52 %	13.36 %

5.5 Summary

In this chapter, a procedure to tune the PV smart inverter settings by grouping them to enhance voltage regulation at grid-edge is proposed. Analysis supporting the grouping of the PVs installed within the feeder neighborhoods experiencing undervoltage violations is presented. The enhanced performance of the PV smart inverters configured with the proposed tuned settings compared to the settings available in literature is demonstrated. The results show that, with the use of tuned settings, voltage range is reduced by 64% and variability index is by 82.5% compared to unity power factor inverter setting in the studied circuit.

Chapter 6

Increasing Feeder PV Hosting Capacity by Regulating Secondary Circuit Voltages

High amounts of residential photovoltaic (PV) systems are being integrated in distribution grids. Some of the states in the U.S. such as California, Hawaii and Arizona have experienced significantly high PV penetrations. Studies and observations in these areas have shown that quite often increased penetration of PV generation results in high voltage levels across distribution system, also known as overvoltage condition [58, 59]. Given that ANSI C84.1 standard recommends a maximum operating voltage of 1.05 per unit (pu) across the distribution circuit, it results that overvoltage condition is often the limiting factor in the maximum PV penetration levels.

Motivated by the applications of edge-of-grid voltage control devices in performing voltage regulation, [1]this chapter proposes the application of low-voltage distribution static compensators (LV-DSTATCOMs) in increasing the PV hosting capacity of distribution circuits. The LV-DSTATCOM is a

---

[1] Parts of this chapter appear in the accepted paper, 'H. V. Padullaparti, S. Jothibasu, S. Santoso, and G. Todeschini, "Increasing Feeder PV Hosting Capacity by Regulating Secondary Circuit Voltages," accepted in *IEEE Power and Energy Society General Meeting*, Portland, OR, Aug. 2018'. The author of this dissertation contributed sections I and III through VI in this paper as first author.

shunt-connected device that can inject or absorb reactive power as needed to regulate the voltage at its terminals. The controlled reactive power absorption can help in reducing the overvoltages on the secondary-wire due to high levels of PV generation. As opposed to the PV smart inverters that primarily supply active power, the LV-DSTATCOMs are dedicated devices to supply or absorb reactive as needed. Additionally, like the case of the other edge-of-grid devices, the utility can select their locations to install for effective voltage regulation. Such flexibility is not available in case of residential PV as the customers decide the residential PV locations. In this chapter, the effectiveness of LV-DSTATCOMs in increasing the PV hosting capacity of distribution circuits is addressed. One of the test distribution circuits developed by EPRI, namely Circuit 24, is used for this study [60]. The circuit's PV hosting capacity is determined using a stochastic analysis framework. The LV-DSTATCOMs are deployed at strategic locations using an iterative placement technique. The results show that the LV-DSTATCOMs are very effective in increasing the PV hosting capacity of distribution circuits. In particular, installation of 23 devices removed overvoltage violations from 1517 loads to increase the PV hosting capacity of the studied circuit from 15% to 100% of the median day time peak load of 16.88 MW. Furthermore, the sensitivity analysis shows that a reduced number of LV-DSTATCOMs are needed to achieve the desired PV hosting capacity level when the devices of higher rating are operated with a lower voltage setpoint.

6.1 PV Hosting Analysis Framework

A stochastic analysis framework is used to evaluate the impacts of PV systems on the distribution circuits. The framework developed in [61, 62] simulates and examines a large variation of PV deployment scenarios. The analysis estimates the PV penetration level (in kW) likely to cause overvoltage in the distribution circuit. The steps used to implement the framework are described in the next sections.

6.1.1 Create PV Deployment Scenarios

In order to reasonably represent the effects of customer-owned small-scale PV systems, multiple PV deployment scenarios are simulated by associating random variations to both locations and sizes of the PVs connected to the customer loads. The location of customers with PV systems are randomly selected from the pool of customers in the distribution circuit. The size of the PV system at each customer location is chosen from a probability density function obtained from installed PV capacities in California [63].

For a PV deployment scenario, 50 customer penetration levels are simulated by increasing customer penetration from 0% to 100% with 2% steps. The customer penetration defines the percentage of customers equipped with PV systems. A 100% customer penetration indicates that all customers have PV installed and the size of the PV is based on the random allocation from the probability density function. In this paper, 100 such PV deployment scenarios are simulated, resulting in a total of 5000 deployment scenarios. The methodology to systematically simulate PV deployment scenarios is depicted in Fig. 6.1. Note that each scenario is unique in the order that PVs are deployed.

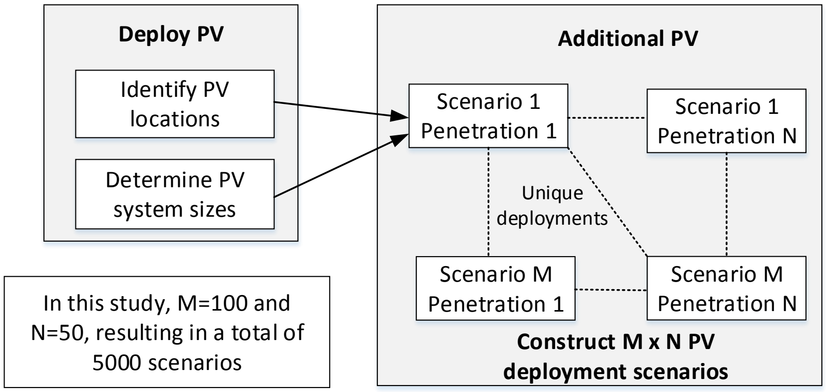

Figure 6.1: The stochastic analysis framework.

6.1.2 Quantify Feeder Impacts

First, a base case model of the selected distribution feeder is developed. The existing PV systems, if any, are incorporated in the distribution circuit. Loads are modified such that total load demand at the substation is 10 percentile of minimum load measured between 10 am to 2 pm throughout a year. The load value is chosen in order to perform a conservative study in which PV generation is at its peak (10 am to 2 pm) while load is at its minimum. A three-phase load flow analysis is then conducted, and the voltage variations are evaluated for the base case model. The status of the LTC transformers and existing capacitors are fixed, and the corresponding state of the distribution circuit is referred to as the base case in this study.

The load flow analysis is then carried out for each PV deployment scenario for a representative minimum load value. From the load flow results for each scenario, steady state voltage at all load terminals are analyzed. If any load terminal voltage exceeds 1.05 p.u., this is recorded as a violation.

The PV hosting capacity of a distribution feeder is defined as the maximum amount of PV generation that can be integrated without violating overvoltage criteria. From the load flow analysis of all scenarios, the hosting capacity corresponding to the first violation scenario is calculated.

6.2 PV Hosting Capacity of Circuit 24

Circuit 24, selected for this study, is an actual 34.5 kV distribution circuit where the longest feeder is 8 miles long [60]. The total primary circuit length is 74 miles to serve 3885 customers (87% residential load). The absolute peak and minimum load demands are 28.67 MW and 6.11 MW, respectively. The representative minimum load value of the circuit is 10.93 MW, which is 10 percentile of the load demand of the circuit between 10 am to 2 pm throughout a year. The median daylight time peak load of the circuit is evaluated to be 16.88 MW.

The PV hosting capacity of the selected feeder is calculated using the stochastic analysis framework described in Section 6.1. The results are presented in Fig. 6.2. In this analysis, the maximum PV capacity corresponding to 100% customer penetration is 17.43 MW. The overall hosting capacity of the feeder is 2.6 MW, corresponding to 15.5% of the median day time peak load. Even though the voltage class of the feeder is high, the overall hosting capacity of the feeder is low. The reason for the low hosting capacity may be due to the length of the feeders. The presence of single voltage regulation equipment (LTC transformer) at the feeder head is not sufficient to maintain the voltage level across the circuit within acceptable limits.

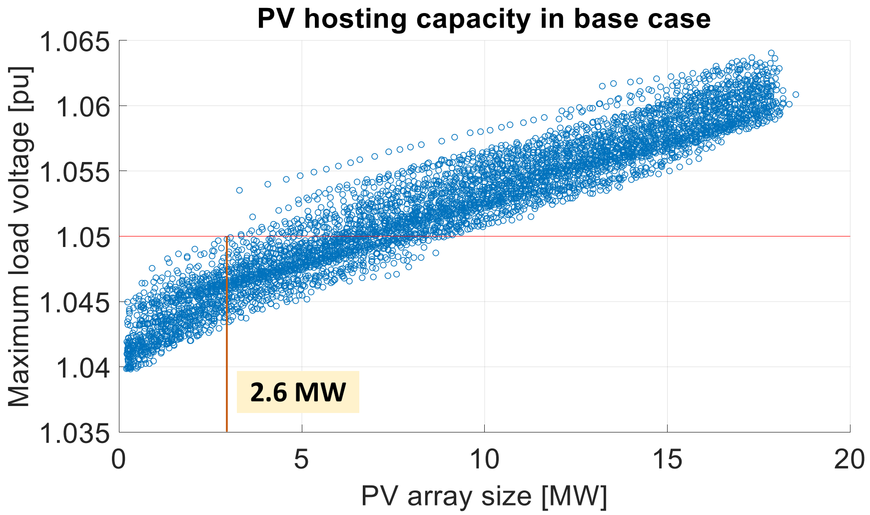

Figure 6.2: Maximum voltage recorded on Circuit 24 for 5000 scenarios with varying levels of PV penetration

The geographical distribution of the loads experiencing overvoltages is shown in Fig. 6.3. In this figure, the color of the primary buses represents the number of scenarios in which the load connected on the associated secondary node has experienced an overvoltage violation. The loads associated with the primary buses in blue color do not experience overvoltage violations. On the other hand, the loads experiencing overvoltage violations with PV integration are highlighted with different colors. There are 1517 loads experiencing overvoltage violations, and 266 primary buses are associated to these loads. These primary buses are grouped in five clusters as shown in Fig. 6.3. This paper will demonstrate that installing low-voltage DSTATCOM in those clusters will help increasing PV hosting capacity by reducing the number of voltage violations

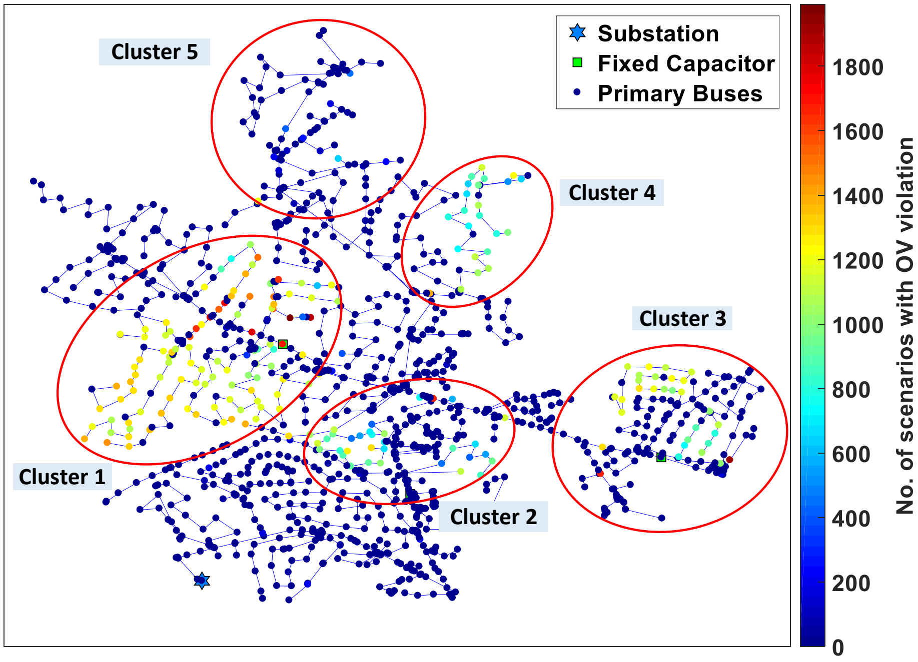

Figure 6.3: Distribution of overvoltage violations in Circuit 24.

6.3 Characteristics of an LV-DSTATCOM

The LV-DSTATCOM is emulated using the voltage controlled generator model available in OpenDSS. The device voltage regulation characteristics can be plotted by connecting a generator object (LV-DSTATCOM) to the service transformer secondary node in a small test circuit as done in Section 2.1.5. The device, rated for 10 kvar, is set to regulate the service transformer secondary node voltage in the test circuit at 1 pu (240 V) while varying the node voltage. This is to study the ability of the device to regulate the voltage at its terminals. The node voltage without and with the LV-DSTATCOM is plotted as shown in the first graph of Fig. 6.4. The reactive power injection/absorption by the device is shown in the second graph of Fig. 6.4. It can be observed that, as the node voltage deviates from the voltage setpoint of 1 pu, the device injects or absorbs the required amount of reactive power up to the maximum power rating to regulate the node voltage at 1 pu. If the node voltage rises above 1 pu, reactive power is absorbed (device behaves like an inductor) to reduce the voltage, and if the node voltage becomes lower than 1 pu, reactive power is injected (like a capacitor) to boost up the voltage.

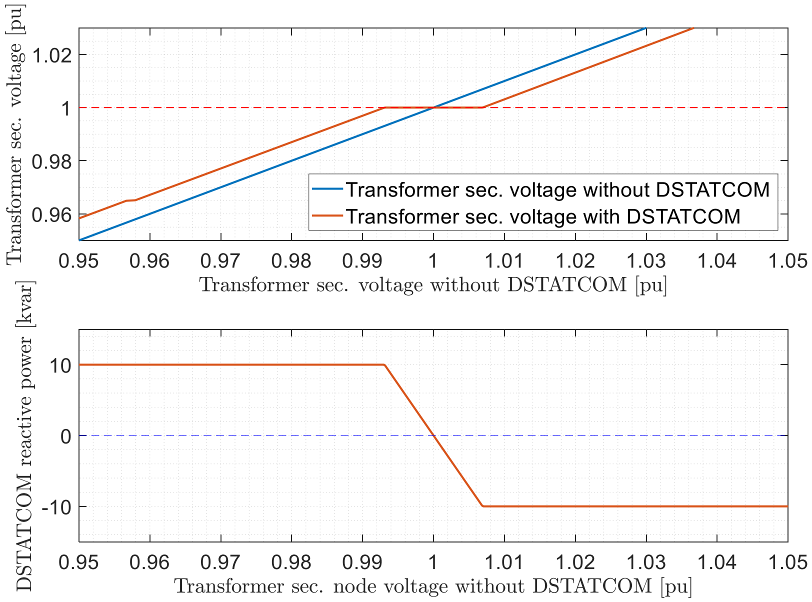

Figure 6.4: Voltage regulation characteristics of a LV-DSTATCOM.

6.4 Device Placement and Increase of PV Hosting Capacity

In this section, the iterative placement technique used for determining the locations of LV-DSTATCOMs is described and the resulting increase in PV hosting capacity is discussed.

6.4.1 Iterative Device Placement Method

As the LV-DSTATCOMs regulate the node voltage by reactive power control, their reactive power injection/absorption helps regulate the voltages at other secondary nodes in the proximity. Therefore, the selection of the most appropriate locations for the device placement helps achieving the desired PV hosting improvements with a low number of devices. In this work, an iterative placement method, similar to the technique described in Section 2.2 is used. The steps involved in the iterative device placement method are shown in Fig. 6.5. PV hosting analysis of the selected distribution circuit is performed for the base case in the first iteration and the load node experiencing overvoltage in the highest number of scenarios is determined. Then an LV-DSTATCOM is placed at the transformer secondary corresponding to that load. In the next iteration, the PV hosting analysis is performed again with the LV-DSTATCOM in service. This process is repeated by placing one device in each iteration while keeping the devices placed in the preceding iterations in service, until there are no overvoltages in the circuit up to the desired PV penetration level.

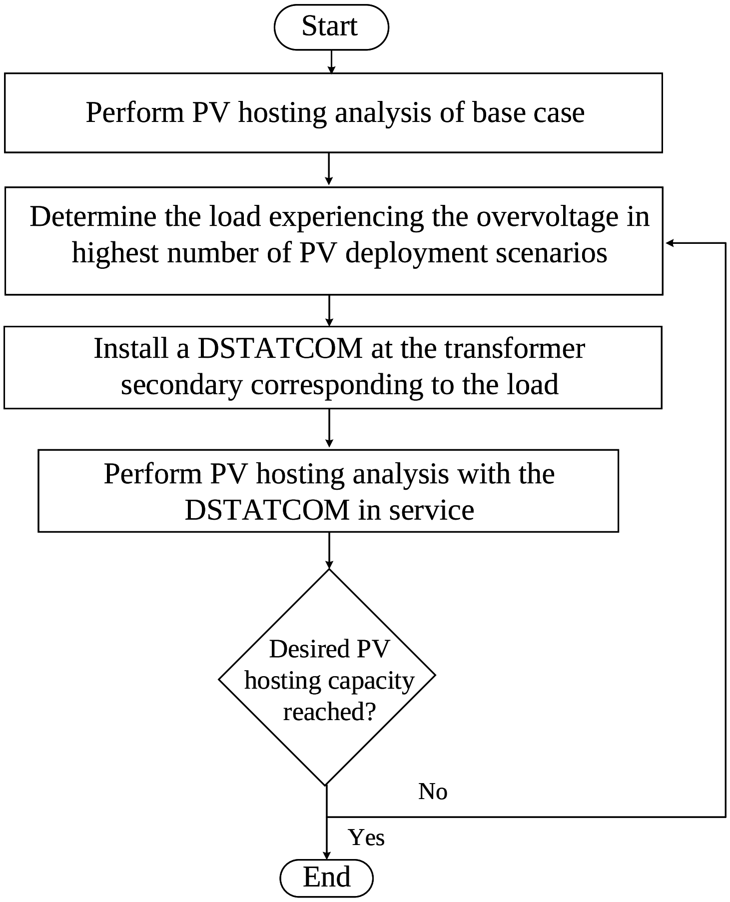

Figure 6.5: Iterative device placement method.

6.4.2 PV Hosting Capacity Results after Deploying LV-DSTATCOMs

The effective locations for the LV-DSTATCOMs in Circuit 24 are shown in Fig. 6.6. Forty devices are placed to increase the PV penetration level to 100% of the median day time peak load without any overvoltage violations at the load terminals. The devices are rated for 10 kvar each, and are configured to regulate the voltage at 240 V (1 pu) at their connection point. Numerous devices are installed in cluster 1 as many loads in this region are experiencing overvoltages in a very high number of PV deployment scenarios. Few devices are placed in clusters 2, 3, and 5. No device is required in cluster 4 as the reactive power support provided by the LV-DSTATCOMs already deployed can regulate the load voltages in this cluster.

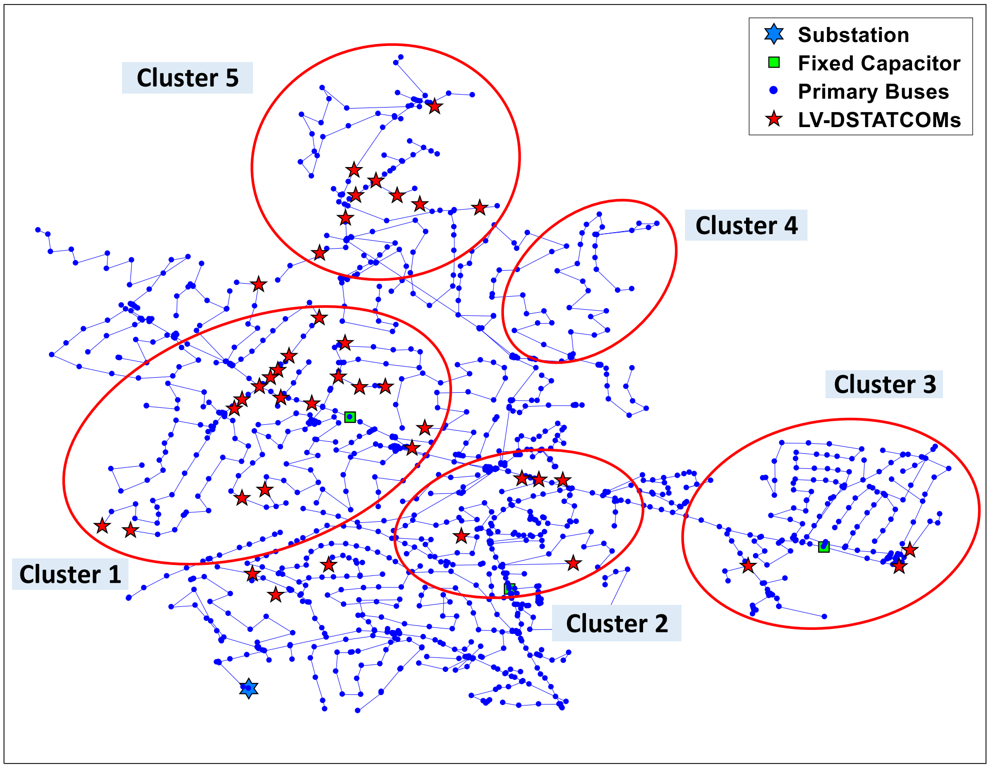

Figure 6.6: LV-DSTATCOM locations in Circuit 24.

The PV hosting analysis is performed with 40 LV-DSTATCOMs in the circuit and the results are shown in Fig. 6.7. It can be observed that none of the PV deployment scenarios have overvoltage violations. The total reactive power output from all devices in all scenarios is shown in Fig. 6.8. In most of the scenarios having low PV penetration levels, the total reactive power absorbed is less than the total rating of the devices which is −400 kvar (the negative sign represents reactive power absorption). In these scenarios, the devices are absorbing only the required amount of reactive power so as to regulate the voltage at their terminal at the voltage setpoint. As the PV penetration level increases, more reactive power is absorbed to regulate the node voltages to the given setpoint (1 pu). In almost all scenarios above 10 MW PV penetration level, full capacity of all LV-DSTATCOMs is utilized for voltage regulation.

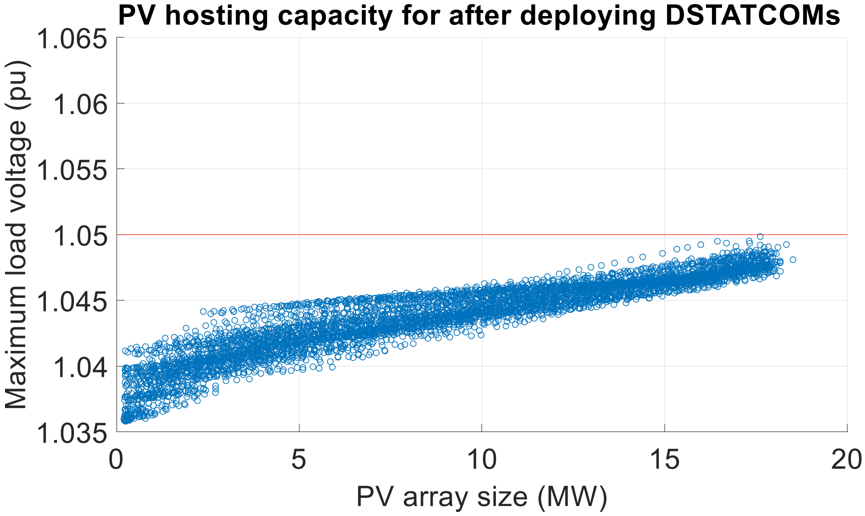

Figure 6.7: Maximum load voltage for varying levels of PV penetration, with 40 LV-DSTATCOMs in service.

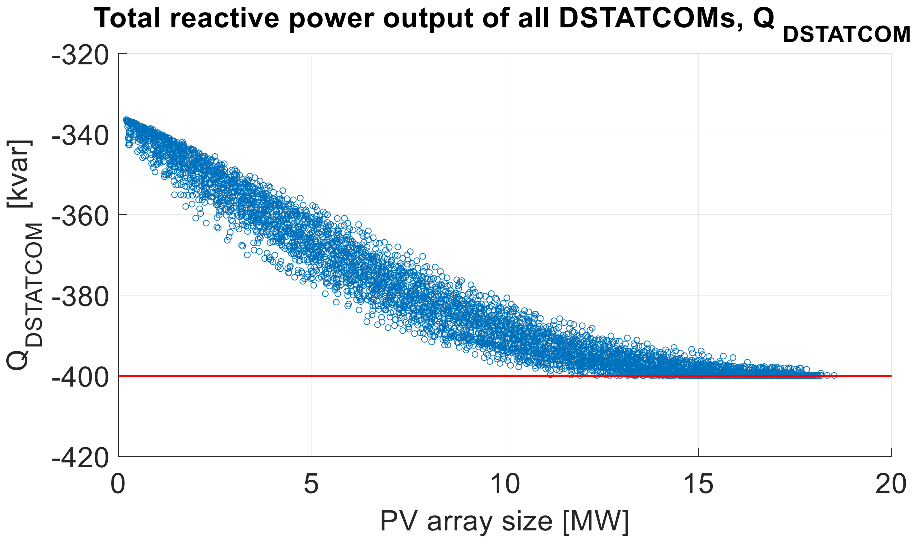

Figure 6.8: Total reactive power output of all LV-DSTATCOMs for varying levels of PV penetration.

6.4.3 Sensitivity Analysis

In this section, results of sensitivity analysis performed with respect to device sizes, voltage setting, and increase in PV hosting capacity are discussed. In Section 6.4.2, a device rating of 10 kvar with a voltage setting of 1 pu is considered. In this section, first the device size is increased in steps of 5 kvar while keeping the same voltage setpoint, the resulting number of devices required to increase PV hosting capacity up to 100% of the median day time peak load is shown in Fig. 6.9. As the device rating increases, the number of devices that are required to achieve 100% customer penetration decreases, but the number of devices remains constant when the rating reaches 25 kvar. This is because as the rating increases, each device is able to provide more reactive power to regulate the node voltages, thus less devices are required to provide the same level of reactive power support. Upon providing the sufficient number of devices with appropriate sizes at the effective locations, increasing the rating does not impact the number of devices, as increased available reactive power will not be utilized fully utilized.

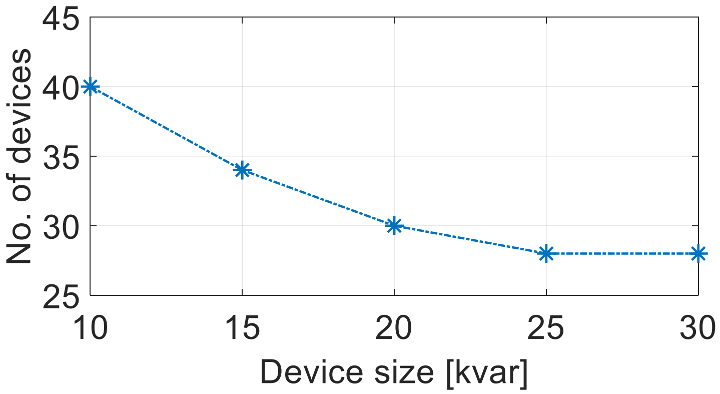

Figure 6.9: Number of devices needed as the device rating increases.

The improvement in the PV hosting capacity of the circuit for different LV-DSTATCOM ratings is also analyzed in this work. The PV hosting capacity results when 10 kvar and 25 kvar devices are installed, with 1 pu voltage setpoint, are shown in Fig. 6.10. It is observed that, when the devices of higher rating (25 kvar) are installed, the PV hosting capacity improves more rapidly compared to the case when the devices of lower rating (10 kvar) are employed. Thus, the desired PV hosting capacity is reached with a low number of devices.

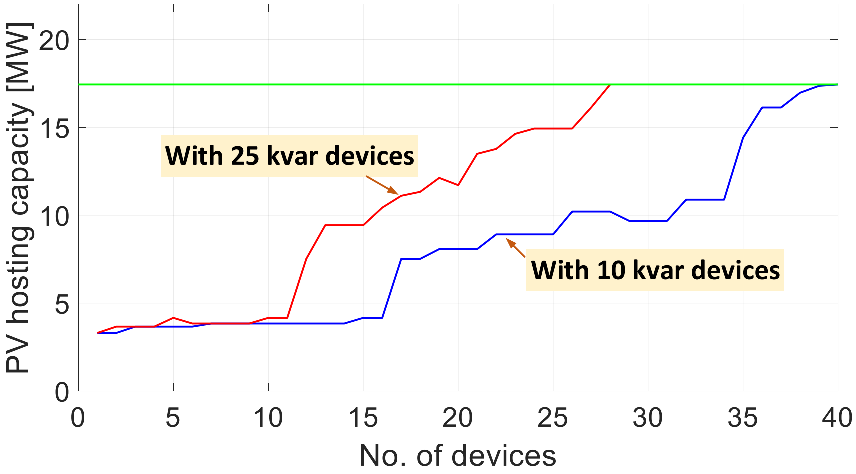

Figure 6.10: Comparison of increase in PV hosting capacities.

The next step consists in the following: the device rating is selected as 25 kvar (observed to be the optimal rating for this circuit from Fig. 6.9) and the devices are installed using the iterative placement method for varying device voltage regulation setpoints. The results are shown in Fig. 6.11. It is observed that, for lower device voltage regulation setpoints, a lower number of devices is needed to achieve 100% of median day time peak load. This is because as the voltage regulation setpoint is lowered, more inductive reactive power is obtained from the existing LV-DSTATCOMs, and therefore less devices are needed.

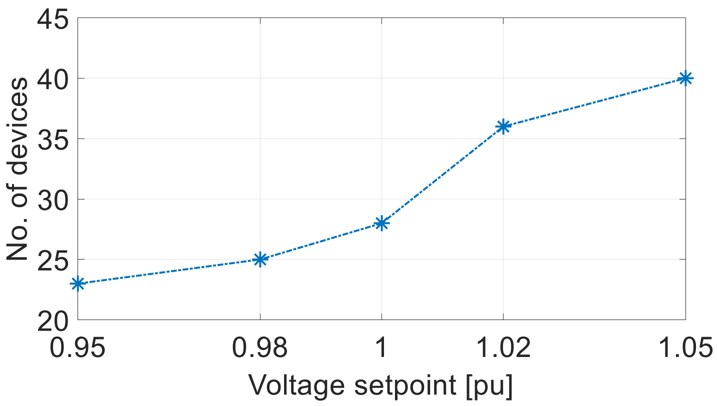

Figure 6.11: Number of LV-DSTATCOMs required as the device voltage setpoint varies.

6.5 Summary

In this chapter, the application of low-voltage DSTATCOMs to increase the PV hosting capacity of large distribution circuits is proposed. Iterative placement method is used to select the effective locations of these devices. Sensitivity analysis is performed with respect to the device numbers, sizes, and voltage setpoints. The results show that, low-voltage DSTATCOMs are effective in increasing the PV hosting capacity. Furthermore, less devices with higher rating and low voltage setpoints can be used to achieve a desired PV hosting capacity.

Chapter 7

Analytical Approach to Estimate Feeder Hosting Capacity based on Protection Criteria

Widespread deployment of distributed energy resources (DERs) such as photovoltaics (PV) and energy storage systems (ESS) in distribution networks is necessitating the development of methods to assess their possible system impacts. Among the key concerns is the impact of these DERs on the system protection. Before integrating DER, system studies need to be performed to assess associated impacts on the existing protection schemes [64]. However, such studies require considerable time and effort [35]. [1]This chapter develops a scalable analysis-based method to conservatively estimate large-scale PV and ESS hosting capacities of a distribution feeder. Typically, the DER impact studies require the development of detailed distribution system models using distribution system simulation tools [34]. Then the developed model is validated using suitable methods such as comparing power flow results with actual field measurements. Once the validated model is available, simulation

---

[1] Parts of this chapter appear in the published paper, 'H. V. Padullaparti, P. Chirapongsananurak, M. E. Hernandez, and S. Santoso, "Analytical Approach to Estimate Feeder Accommodation Limits Based on Protection Criteria," *IEEE Access*, vol. 4, pp. 4066-4081, 2016'. The author of this dissertation contributed all the sections in this paper as first author.

studies are performed to assess the impact of DER integration on protection schemes with numerous scenarios, often in thousands. Additionally, this process can also pose several complications of scalability such as power flow solution convergence problems, the complexity of analysis and visualization of results considering a large number of fuses, huge time requirement to study all possible combinations of PV sizes, and fault locations [11].

In the absence of insights into the relationship between various system parameters causing the operational issues with DER integration, the utility planners are usually forced to apply conservative rules of thumb penetration levels to accept DER interconnection requests. For PV integration, the penetration level is limited to 15% of the maximum feeder load on a line section to avoid any adverse impacts [10]. Alternatively, system studies need to be performed with all possible combinations of fault types, fault locations, PV size and locations which are time consuming posing scalability challenges and resulting in circuit specific outcomes. In this context, this chapter develops a scalable analysis-based method to conservatively estimate large-scale PV and ESS hosting capacities of a distribution feeder without causing relay insensitivity and sympathetic tripping problems. The objective is to simplify the estimation process with reasonable approximations under conservative settings without requiring to carry out complex simulations. Furthermore, insights into the overcurrent relay settings are provided when large-scale PV and ESS are present. The analysis presented considers 'low voltage ride through' (LVRT) or 'fault ride through' (FRT) requirements of PV and ESS which stipulates the PV and ESS to remain connected to the system during fault conditions. The battery energy storage system is assumed for the ESS.

7.1 Analysis of Relay Reach and Sympathetic Tripping with PV and ESS

7.1.1 Reduction of Relay Reach

The fault current contributions from DER such as PV and ESS reduce the reach of the overcurrent relays installed upstream. To analyze reduction of relay reach, consider the distribution circuit shown in Fig. 7.1a where a large-scale PV system is planned to be connected to a bus in the middle of the feeder. The upstream transmission system of the substation including the substation transformer is represented by a Thevenin equivalent circuit with impedance Z_{eq}. Phase overcurrent relay ‘R’ is installed at the substation. A remote end fault with resistance R_f is assumed for conservative study. The impedances of the feeder sections upstream and downstream of the PV location are represented by Z_{Line1} and Z_{Line2}, respectively.

Analysis for symmetrical faults: Consider the fault in Fig. 7.1a is a three-phase fault. The equivalent circuit of the system when the PV is not connected is shown in Figure 7.1b. Using Kirchoff’s voltage law (KVL), the fault current seen by the relay is given by:

$$I_{R,noPV} = \frac{V_{sg}}{(Z_{eq} + Z_{Line1} + Z_{Line2} + R_f)} \tag{7.1}$$

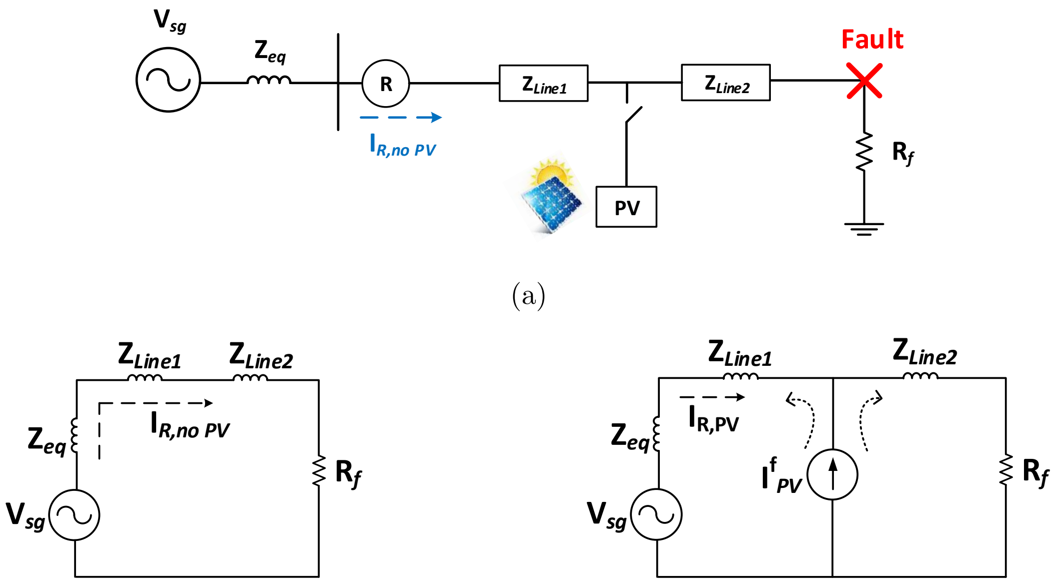

(a)

(b)

(c)

Figure 7.1: (a) Distribution system with a fault (b) Equivalent circuit without PV (c) Equivalent circuit with PV.

where V_{sg} and $I_{R,noPV}$ are the line-to-ground pre-fault voltage at the substation bus and fault current through the relay without PV, respectively.

When the large-scale PV system is connected which injects fault current I_{PV}^{f} during the three-phase fault, the equivalent circuit of the distribution system is shown in Fig. 7.1c. Then the fault current through the relay with the large-scale PV connected can be obtained by applying superposition in Fig. 7.1c as

$$I_{R,PV} = I_{R,noPV} - \frac{(Z_{Line2} + R_f)}{(Z_{eq} + Z_{Line1} + Z_{Line2} + R_f)} I_{PV}^{f} \tag{7.2}$$

Following conclusions can be drawn from (7.2):

1. The fault current through the relay is reduced due to the fault current contribution from the PV during a three-phase fault. This current seen by the relay is also influenced by the available short-circuit capacity at the substation.
2. The location of PV alters the fault current distribution. When the PV is located close to the substation, Z_{Line2} is maximum causing more reduction in the fault current seen by the relay at the substation. For the worst case scenario, the PV is located close to the substation and the fault occurs at the remote end of the feeder. In such a scenario, when the three-phase fault resistance is sufficiently high, the fault current seen by the relay goes below its phase overcurrent pickup value, making the relay insensitive to the fault. This is called relay insensitivity.
3. When relay becomes insensitive to a fault of a given fault resistance, any additional fault current contribution from the PV would further reduce the fault current seen by the relay, making it insensitive to the faults with lesser fault resistance.

Assuming the fault current contribution from the large-scale PV is twice the PV rated current [16, 17], the fault current through the phase overcurrent relay from (7.2) can be expressed in terms of the PV size as (7.3).

$$I_{R,PV} = I_{R,noPV} - Z' \left\{ \frac{2 \times \text{PV rating}}{\sqrt{3} \times \text{PV bus voltage}} \right\} \tag{7.3}$$

where $Z' = \dfrac{(Z_{Line2} + R_f)}{(Z_{eq} + Z_{Line1} + Z_{Line2} + R_f)}$

When the ESS is also present in the system in discharging mode, (7.2) can be modified as:

$$I_{R,PV+ESS} = I_{R,noPV} - Z'(I^f_{PV} + I^f_{ESS})$$

where I^f_{ESS} is the fault current contribution from the ESS.

It is observed from Z' that the maximum reach reduction occurs when Z_{Line2} is maximum, i.e., when the PV or ESS is installed close to the substation and the fault is at the remote end. Under this condition, if the grid impedance Z_{eq} is neglected as it is typically much smaller than the feeder impedance, then $Z' = 1$. This implies that the reduction in phase overcurrent relay current is exactly equal to the fault current injection from the PV or ESS.

Analysis for unsymmetrical faults: Considering the fault at the remote end of the feeder as SLG, the analysis has been extended in [65] using sequence networks and maximum unbalance fault current injection from PV as shown in Fig. 7.2. Noting that the positive and negative sequence impedances of distribution lines are equal, corresponding impedances of feeder sections upstream and downstream of the PV location are denoted as Z_{Line1} and Z_{Line2} respectively in this figure. Zero sequence impedances of the feeder sections are denoted by Z^0_{Line1} and Z^0_{Line2}.

The sequence components of fault currents injected by the PV for maximum unbalance shown in Fig. 7.2c is given by:

$$[I^f_{PV}]_{012} = [A]^{-1} \begin{bmatrix} 2I_{PVa} \\ I_{PVb} \\ I_{PVc} \end{bmatrix} = \frac{1}{3} \begin{bmatrix} I_{PV}\angle 0^\circ \\ 4I_{PV}\angle 0^\circ \\ I_{PV}\angle 0^\circ \end{bmatrix} \tag{7.4}$$

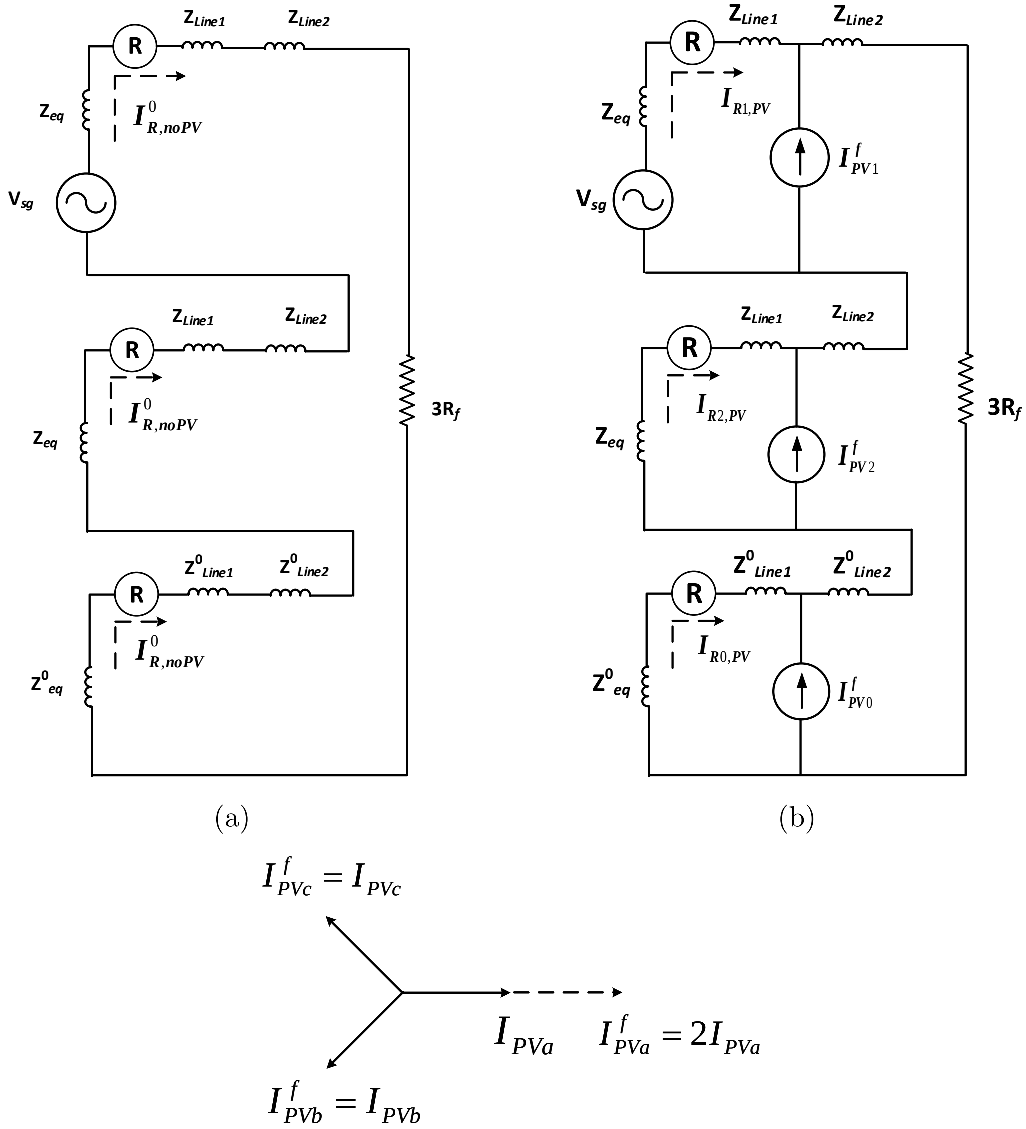

(a) (b)

(c)

Figure 7.2: Equivalent circuit of distribution system with SLG fault a) without PV and b) with PV c) Fault current injections by PV systems for maximum unbalance during the SLG fault.

The impact of fault current contribution from a large-scale PV on the ground overcurrent relay reach can be expressed as:

$$I_{RN,PV} = I_{RN,noPV} - Z'' \times I_{PV} \tag{7.5}$$

$$I_{RN,PV} = I_{RN,noPV} - Z'' \left\{ \frac{\text{PV rating}}{\sqrt{3} \times \text{PV bus voltage}} \right\} \tag{7.6}$$

where $I_{RN,PV}$ is the ground fault current seen by relay with PV and $Z'' = \dfrac{1}{Z_{TS}}[2Z_{Line2} + Z^0_{Line2} + 3R_f - 3(Z_{Line1} + Z_{eq})]$.

Equations (7.5) and (7.6) indicate that the ground fault current reduction depends on PV rated current (PV size), fault resistance, PV location and available short-circuit capacity at the substation. For the worst case scenario, PV is installed close to the substation and SLG fault occurs at feeder's farthest end for maximum reach reduction of the ground overcurrent relay.

From the parameters of Z'', it is observed that the maximum reach reduction occurs when Z_{Line2} is maximum, i.e., when the PV is installed close to the substation and the fault is at remote end. In this scenario, if Z_{eq} is neglected, then $Z'' = 1$. This implies that the reduction in ground overcurrent relay current is exactly equal to the rated PV current which is less than PV fault current contribution. As such, the reduction in ground fault current seen by feeder head-end relay is less than the phase overcurrent relay current reduction in case of three-phase faults.

When the ESS is also present, analysis can be done along the same lines and the ground fault current seen by the upstream relay can be obtained from (7.5) as

$$I_{RN,PV+ESS} = I_{RN,noPV} - Z''(I_{PV} + I_{ESS}) \tag{7.7}$$

For conservative estimation, (7.7) considers that both ESS and PV fault currents are in phase with each other. Then, the PV rating in (7.6) includes both PV and ESS ratings, when ESS is also present.

7.1.2 Sympathetic Tripping

Sympathetic tripping occurs when the fault current from the PV causes relays on the healthy feeder to pick up for faults on the adjacent feeders resulting in an unnecessary outage of the healthy feeder. To analyze the sympathetic tripping, consider the system shown in Fig. 7.3a where a large-scale PV system is connected in Feeder 1 and a three-phase fault is assumed on adjacent Feeder 2. Its equivalent circuit is shown in Fig. 7.3b. During the fault, if the PV system remains in the circuit, it feeds the fault back through the relay ‘R’ at the substation. When the large-scale PV is of considerable size, the fault current from the PV can go above the pickup setting of the overcurrent relay at the substation causing unwanted tripping of the Feeder 1.

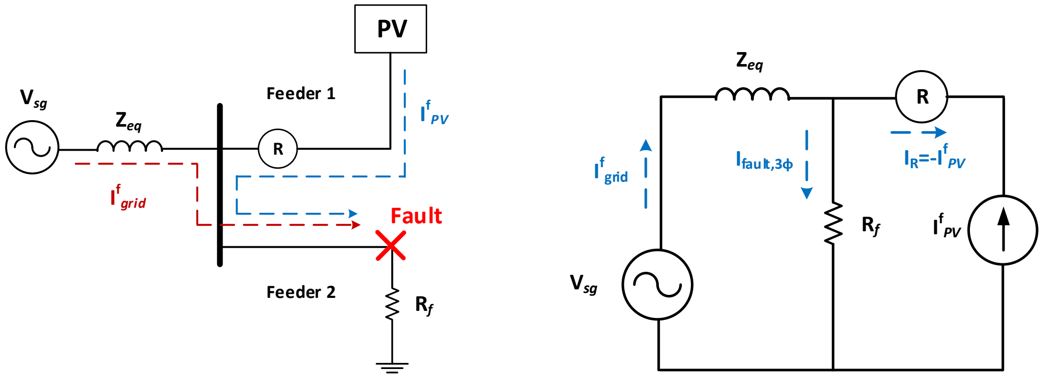

(a) (b)

Figure 7.3: a) Illustration of sympathetic tripping b) Equivalent circuit.

Analysis for symmetrical faults: From Fig. 7.3b, the fault current through the relay in Feeder 1 is

$$I_R = -I^f_{PV}$$

It indicates that the current through the relay solely depends on the fault current from the large-scale PV system and flows in the reverse direction. Therefore, as the PV size increases, its fault current contribution also increases and eventually trips the relay when the current from the PV goes above the phase overcurrent relay pickup current setting.

Considering that I^f_{PV} is twice the I_{PV} for the conservative estimate, the magnitude of the fault current flowing through the relay can be expressed in terms of the PV rating as:

$$|I_R| = |I^f_{PV}| = \left| \frac{2 \times \text{PV rating}}{\sqrt{3} \times \text{PV bus voltage}} \right| \tag{7.8}$$

If the ESS is also present in the system, we need to consider its fault current contribution also for the sympathetic tripping study. Assuming the ESS is connected to the same bus to which the large-scale PV is connected and is injecting fault current in phase with the PV fault current, the fault current seen by relay becomes $|I_R| = |I^f_{PV} + I^f_{ESS}|$ and the PV rating in (7.8) includes the ESS rating also.

Analysis for unsymmetrical faults: In the case of SLG faults, the ground overcurrent relay of the feeder shall detect the ground fault current and trip. The ground fault current or residual current through the relay is the sum of the fault currents being injected by the PV system in all the three phases and can be expressed as:

$$I_{RN,PV} = -(I^f_{PVa} + I^f_{PVb} + I^f_{PVc}) = -3I^f_{PV0} \tag{7.9}$$

From (7.4) and (7.9), the current seen by the ground overcurrent relay under maximum unbalance condition is $|I_{RN,PV}| = |I_{PV}|$. In terms of PV rating, this can be expressed as

$$|I_{RN,PV}| = |I_{PV}| = \left|\frac{\text{PV rating}}{\sqrt{3} \times \text{PV bus voltage}}\right| \tag{7.10}$$

When the ESS is also present, the total ground fault current through the relay would be the vectorial sum of both the ground fault currents from the PV and the ESS which is given by

$$\begin{aligned} I_{RN,PV+ESS} &= -\,(I^f_{PVa} + I^f_{PVb} + I^f_{PVc}) - (I^f_{ESSa} + I^f_{ESSb} + I^f_{ESSc}) \\ &= -\,3(I^f_{PV0} + I^f_{ESS0}) \end{aligned} \tag{7.11}$$

where I_{PV0}^{f} and I_{ESS0}^{f} are the zero sequence current injections from PV and ESS respectively.

If we conservatively assume that ESS is injecting fault currents in phase with PV fault currents, the PV rating in (7.10) gives combined PV and ESS rating.

7.2 Validation of the Analysis using a Utility Distribution Feeder Model

The analysis presented in the previous section is validated through the simulation studies on a utility distribution feeder model in OpenDSS.

7.2.1 System Description

For simulation studies, a detailed distribution circuit model has been developed in OpenDSS using the data obtained from a utility. The data comprises of the transformer, line data, load profiles, capacitors, regulator data etc. The system has a 24 MVA transformer at the substation. The three-phase and single-phase short-circuit MVA of transmission system upstream of the substation transformer are 562 MVA and 93 MVA respectively. A 1.6 mi long 12.47 kV level primary distribution feeder is supplied by this transformer. Maximum loading in the feeder is 15.77 MW and the corresponding load current is 730 A. Minimum loading is 6 MW. This detailed distribution model is used for simulations.

Figure 7.4 shows the single-line diagram of the distribution system used for theoretical calculations. The sequence impedances of the system are obtained from the short-circuit study which are given in Table 7.1.

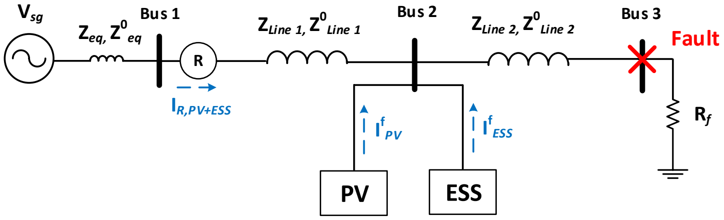

Figure 7.4: Single-line diagram of utility distribution feeder with fault.

Table 7.1: Sequence impedances of different sections of the utility distribution feeder

Feeder Section	**Sequence Impedance (Ω)**
Substation	$Z_{eq} = 0.1016\angle 72.4°$ $Z^0_{eq} = 0.312\angle 74.1°$
Upstream of PV & ESS	$Z_{Line1} = 1.389\angle 55.4°$ $Z^0_{Line1} = 2.193\angle 55.56°$
Downstream of PV & ESS	$Z_{Line2} = 0.538\angle 59.45°$ $Z^0_{Line2} = 1.678\angle 60.97°$

Following circuit conditions are considered for this study:

a) The breaker installed at the feeder head is controlled by both phase and ground overcurrent relays. The pickup setting for the phase overcurrent relay is considered as 200% of the maximum load current plus some margin that is 1500 A. For ground overcurrent relays, the pickup current setting is chosen as 100% of the maximum load current plus some margin that is 750 A.

b) The PV and ESS are connected to a bus approximately 0.83 mi away from the substation (Bus 2) and the fault is simulated at the remote bus (Bus 3) as shown in Fig. 7.4.

7.2.2 Reduction of Relay Reach

The utility distribution feeder model is simulated initially with a bolted three-phase fault at bus 3 without the large-scale PV and ESS in the system. The fault resistance is increased and the phase-A current through the relay at the substation is monitored. Next, a large-scale PV system is connected to bus 2 and the study is repeated. The fault current profiles seen by the phase overcurrent relay for varied fault resistance as the PV size is increased from 1 MW to 8 MW are shown in Fig. 7.5b. It is observed that when the PV is not connected, the relay at the substation is insensitive to the three-phase faults with $R_f > 3.8\ \Omega$. In other words, the phase overcurrent relay cannot detect the three-phase remote end faults having fault resistance higher than 3.8 Ω. As the PV size is increased, the corresponding PV fault current contribution I_{PV}^f is increased resulting in relay insensitivity at lower fault resistances. For the large-scale PV size of 8 MW, the phase overcurrent relay is insensitive to the remote end three-phase fault with resistance above 2.5 Ω. In the simulation, the PV fault current under this condition is observed as 550 A which is 1.5 times the rated PV current $I_{PV} = 370$ A.

The simulation results can be compared with theoretical relay currents predicted using (7.2) to validate the analysis. The pre-fault voltage of Bus 3 is obtained from the load flow program as $V_{sg} = 7279\angle -33.7^\circ$. Using the system parameters given in Table 7.1, (7.2) can be written in terms of the PV rating as

$$I_{R,PV} = \frac{7279\angle -33.7^\circ}{(2.024\angle 57.32^\circ + R_f)} - \frac{(0.538\angle 59.45^\circ + R_f)}{(2.024\angle 57.32^\circ + R_f)} \left\{ \frac{1.5 \times \text{PV rating}}{\sqrt{3} \times 12.47 \text{ kV}} \right\} \tag{7.12}$$

Figure 7.5a shows the predicted fault currents seen by phase overcurrent relay at the substation using (7.12) for various PV ratings and R_f. The theoretical predictions shown in Fig. 7.5a closely match with the results obtained using circuit simulations shown in the Fig. 7.5b, confirming the validity of the analysis. In particular, the PV size to cause relay insensitivity for a remote end three-phase fault resistance of $R_f = 2.5\ \Omega$ is 8 MW in both the figures.

The impact of ESS on the fault current seen by the upstream phase overcurrent relay is studied by connecting a three-phase ESS of rating 3 MW to Bus 2 along with the large-scale PV of rating 1 MW. The variation of fault currents seen by the phase overcurrent relay when there is no PV, when the PV is connected to Bus 2, and when both PV and ESS are connected to Bus 2 is shown in Fig. 7.6a. It is observed that when the large-scale PV is not connected, the phase overcurrent relay is insensitive to the three-phase faults with $R_f > 3.8\ \Omega$ as in the previous case. When the 1 MW PV is connected, the relay is insensitive to the three-phase faults with $R_f > 3.6\ \Omega$ due to the fault current injection of $I_{PV}^{f} = 63$ A by the PV. And when the 3 MW ESS is also connected, the relay insensitivity occurs at a further lower value of

$R_f > 3.1\ \Omega$ due to the additional fault current contribution of $I_{ESS}^{f} = 179.6$ A by the ESS. The results show that the effect of ESS is similar to that of the large-scale PV for protection studies. As such, the ESS of higher ratings can reduce the overcurrent seen by the upstream phase overcurrent relays and can interfere with the feeder overcurrent protection.

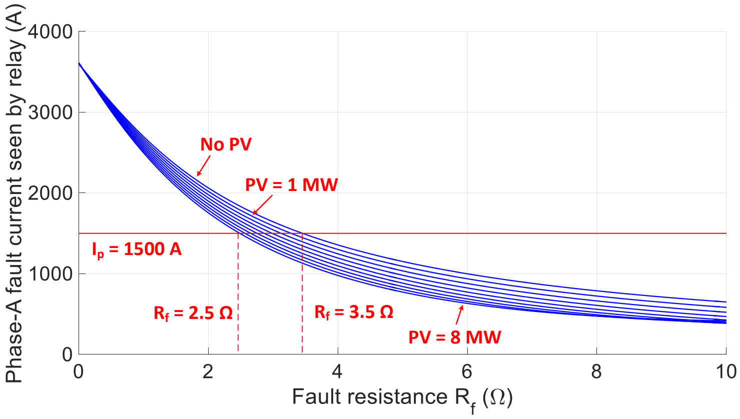

(a)

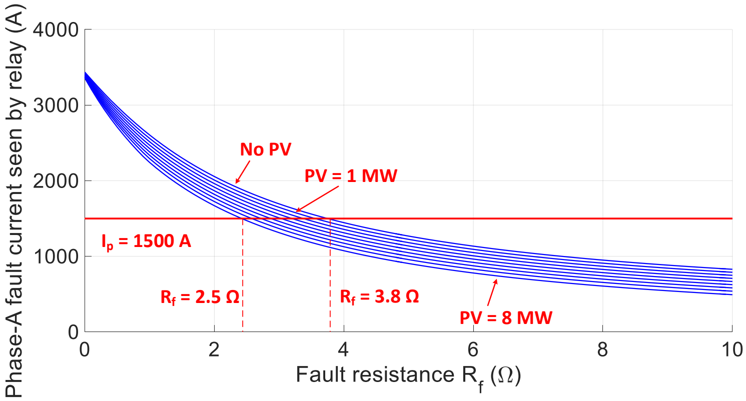

(b)

Figure 7.5: (a) Predicted current seen by the relay for various PV ratings and R_f using (7.12) (b) Fault current seen by phase overcurrent relay with large-scale PV and varied remote end three-phase fault resistance using circuit simulations.

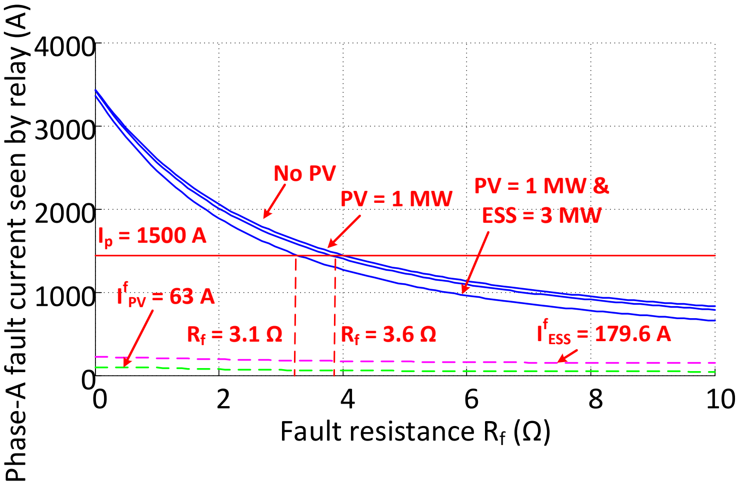

(a)

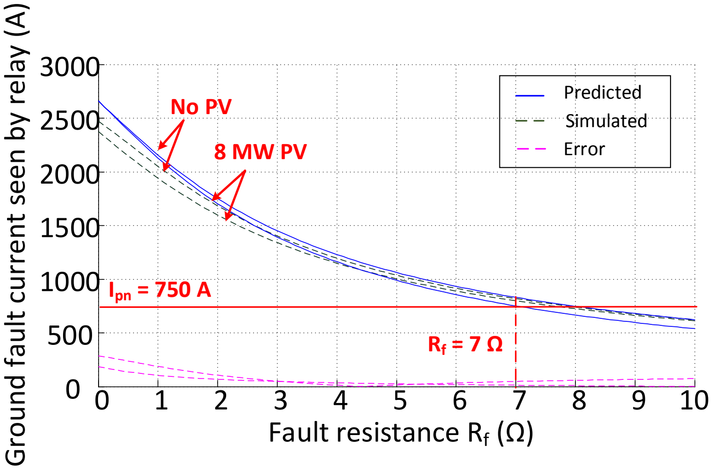

(b)

Figure 7.6: (a) Fault current seen by the phase overcurrent relay installed at the substation for various PV ratings and three-phase fault resistance when a 3 MW ESS is present (b) Comparison of predicted ground fault current seen by relay using (7.5) and simulated values without PV and with 8 MW PV for varied R_f.

The impact of ground fault current contribution from the large-scale PV on the fault current seen by the ground overcurrent relay can be predicted using (7.6) for the system parameters in Table 7.1. The predicted ground overcurrent results when the large-scale PV ratings are 1 MW and 8 MW are shown in Fig. 7.6b. For ease of comparison, the ground overcurrent results obtained from the SLG fault simulation using the detailed distribution system model are also shown in the same figure. From both theoretical predictions and simulation results, it is observed that the reduction in the ground fault current seen by the upstream relay increases as the large-scale PV size increases. Note that (7.6) gives most conservative predictions by considering maximum unbalance in the PV fault current injection. It is observed that the error between the predicted and simulated fault current results in the region of interest where the relay insenstivity of ground overcurrent relay occurs that is at $R_f = 7\ \Omega$ is very less, thus validates the analysis.

7.2.3 Sympathetic Tripping with PV and ESS

Figure 7.7 shows the single-line diagram of the utility distribution feeder including an adjacent feeder. In the OpenDSS, the adjacent feeder is modeled as an aggregated load equal to the yearly demand of the main feeder which is 4726 kW. For sympathetic tripping simulation study, initially a large-scale PV system is connected to the Bus 1 and a bolted three-phase fault is simulated at a bus on the adjacent feeder. Both the buses are closest to the substation on the respective feeders.

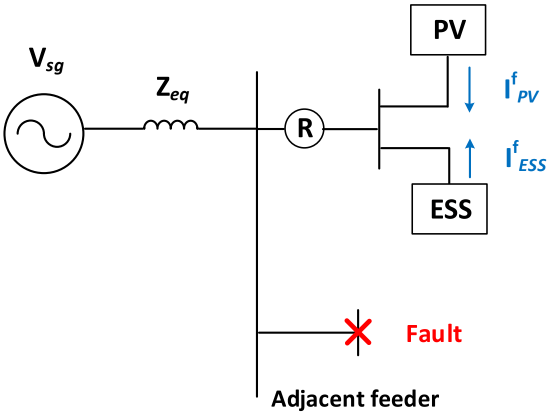

Figure 7.7: Utility distribution system with the adjacent feeder.

Figure 7.8a shows the fault current through the phase overcurrent relay as the large-scale PV size is increased from 0 MW to 20 MW. The figure also shows the effect of ESS on the fault current seen by the relay. It is observed that, when the ESS is not connected, the fault current through the phase overcurrent relay is increased as the PV size is increased and reached the pickup value of 1500 A at 16.2 MW of PV size. The large-scale PV size for causing sympathetic tripping can also be estimated from (7.8) as 16.2 MW, matching with the simulation results.

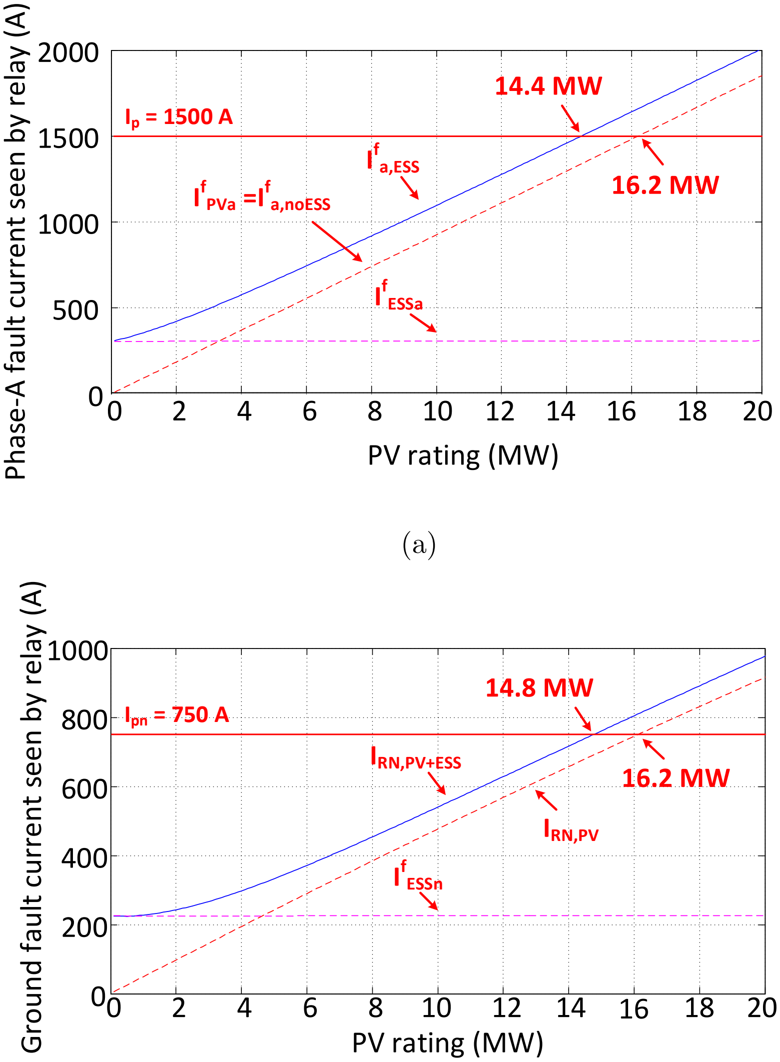

(a)

(b)

Figure 7.8: (a) Fault current seen by phase overcurrent relay without and with ESS as the PV size is increased (b) Fault current seen by ground overcurrent relay as the PV size is increased.

The effect of the fault current contribution from the ESS is studied by connecting an ESS of size 3 MW to Bus 1 along with the large-scale PV. The simulation results are shown in Fig. 7.8a. When the ESS is also connected to the system along with PV, it is observed that the sympathetic tripping occurs at 14.4 MW of large-scale PV rating which is less compared to the case without ESS. This is due to the additional fault current contribution from the ESS. At this point, total 17.4 MW of PV and ESS present in the system. The fault current contributions from the large-scale PV and the ESS in the phase-A are noted as: $I^f_{PVa} = 1333.4\angle 155.9°$ A and $I^f_{ESSa} = 321.03\angle 92.2°$ A, respectively. The fault current in the phase-A of the feeder is $I^f_a = I^f_{PVa} + I^f_{ESSa} = 1503.6\angle - 35.1°$ A. We can make a conservative estimate of the combined PV and ESS rating for the possibility of sympathetic tripping using (7.8) also which is 16.2 MW. Note that the conservative estimate of the PV and ESS rating for the likelihood of sympathetic tripping is slightly lower than the simulated result. This is due to the fact that the fault current injections from the PV and the ESS in the simulation are out of phase.

For unsymmetrical fault analysis, the sympathetic tripping study is done by simulating an SLG fault on the adjacent feeder as shown in Fig. 7.7. The ground fault current seen by the ground overcurrent relay as the large-scale PV size is increased from 0 to 20 MW is shown in Fig. 7.8b. It is observed that as the PV size is increasing, its ground fault current contribution is also increasing, going above the ground overcurrent pickup value of 750 A at a PV size of 16.2 MW. At this point, the feeder currents in all the three phases are $I^f_a = 1500.3\angle - 24.5°$ A, $I^f_b = 848.49\angle 40.4°$ A, $I^f_c = 889.76\angle - 88.7°$ A, and the residual current seen by the relay is $I_{RN,PV} = I^f_a + I^f_b + I^f_c = 753.83\angle - 22°$

A. The large-scale PV rating to cause sympathetic tripping can be estimated from (7.10), i.e., 16.2 MW.

Figure 7.8b shows the simulation results when three single-phase ESS of 1 MW rating each are also connected to Bus 1 along with the PV. It can be observed that the sympathetic tripping now occurs at a large-scale PV size of 14.8 MW which is lower than the previous case due to the additional fault current contribution from the ESS. When the ground fault current through the feeder goes above the pickup value, the ground fault current contributions from the PV and the ESS are $I^f_{PVn} = 718\angle-16.8^\circ$ A and $I^f_{ESSn} = 226.1\angle-111.46^\circ$ A, respectively. The residual current seen by the relay is $I_{RN,PV+ESS} = I^f_a + I^f_b + I^f_c = 751\angle-39^\circ$ A. The PV and ESS combined size in the simulation for the sympathetic tripping to occur is 17.8 MW. The PV and ESS size conservative estimate from (7.10) is 16.2 MW. The conservative estimate is slightly lower than the simulated result because the ground fault current injections by the PV and ESS are out of phase. However, the deviation of estimated PV and ESS size from the simulated size in this case is less than 7%.

7.3 Summary

In this chapter, a comprehensive analysis of relay insensitivity and sympathetic tripping problems in a utility distribution feeder is provided with an aim to conservatively estimate the large-scale PV and ESS hosting capacities of the distribution feeder. Based on the analysis, the factors influencing the impact of large-scale PV and ESS on the overcurrent protection schemes are discussed. The proposed analysis-based approach is scalable and thus can be applied to large distribution circuits also. The analytical conclusions are validated by simulation results using a detailed distribution circuit model of a utility in OpenDSS. Normally, in addition to the breaker at the substation, the distribution circuits can have few reclosers placed along the feeder. In such cases, the expected fault current can be computed at each recloser using the proposed method. Once we have the expected fault currents with large-scale PV and ESS, the possibility of relay/recloser insensitivity can be checked quickly by comparing with the pickup current setting.

Chapter 8

Conclusions

This dissertation aims to develop methods and algorithms to improve voltage regulation and system protection for modern grids. For voltage regulation, edge-of-grid voltage control devices are modeled and algorithms for deploying them are developed to remove voltage violations, perform voltage smoothing, lower energy losses, and increase the feeder PV hosting capacity through grid edge voltage control. To assess the PV and ESS hosting capacities of a distribution feeder with respect to overcurrent protection criteria and to provide insights into the relay settings, an analytical approach is developed. Detailed distribution circuit models are developed using the data from utilities to evaluate the efficacy of the proposed algorithms. In this final chapter, the key results and contributions are summarized.

Chapter 2 investigates the effectiveness of the edge-of-grid voltage control devices in removing the low-voltage violations in distribution circuits. First, the modeling and characteristics of low-voltage universal power flow controller (UPFC) and static var compensator (SVC) are discussed. It is concluded that, the UPFC regulates the load voltage through series voltage injection (in voltage regulation mode) and the SVC performs voltage regulation using reactive power injection. Both these devices are operated using local autonomous voltage-based controllers. Next, an algorithm based on undervoltage area criterion for effective placement of these devices is proposed. A set of 1 UPFC and 15 SVCs are deployed in an actual distribution circuit of a utility using the proposed algorithm. The results show that, the edge-of-grid devices augment the traditional primary side voltage controls in regulating the load voltages in distribution networks.

Chapter 3 presents a multi-objective optimization approach for placement of edge-of-grid SVCs considering voltage violations, energy losses, and traditional voltage regulation equipment switching operations. The goal is to minimize these parameters while placing the minimum number of SVCs operating on local voltage-based controllers. The binary particle swarm optimization (BPSO) is used to solve the proposed binary optimization formulation. The results show that, the placement of edge-of-grid SVCs using the proposed approach helped lowering the energy losses, switching operations while improving the voltage regulation in a utility distribution circuit.

In chapter 4, a two-stage optimization framework based on AC optimal power flow (ACOPF) for optimal placement and real-time centralized control of edge-of-grid low-voltage SVCs (LV-SVCs) is proposed to minimize the energy losses while maintaining the load voltages within acceptable limits. In the first stage, the objective is to minimize the investment cost per day of the LV-SVCs. Based on the optimal dispatch of capacitors, which is the solution of the first stage, the optimal locations of LV-SVCs are determined. These locations are the input to the second stage, in which the ACOPF is run again to determine the real-time secondary-side reactive power injections in the circuit by LV-SVCs to minimize the active power losses. The distribution circuit's performance using the proposed real-time centralized control of LV-SVCs is compared with that of the LV-SVC operation using local voltage-based controllers. A 3% reduction in the energy losses is observed in the study when the real-time control using the proposed approach is applied compared to the base case when LV-SVCs are not present.

As the determination of effective smart inverter settings for photovoltaic (PV) systems is a complex process, chapter 5 proposes a simplified tuning procedure for the PV smart inverter control parameters for voltage regulation and smoothing. Defining the voltage range and voltage variability index metrics, the proposed approach quantifies the steady-stage voltage variation and voltage fluctuations in the PV terminal voltages from peak day quasi-static time-series (QSTS) simulation. Then the effective PV smart inverter control settings are identified as those resulting in the low voltage range and voltage variability indexes. The results show that, when the tuned settings using the proposed approach are used, the voltage range is reduced by 64% and the variability index is reduced by 82.5% compared to the unity power factor operation of PV in the studied circuit.

Motivated by the benefits of edge-of-grid devices, chapter 6 proposes the application of low-voltage DSTATCOMs (LV-DSTATCOMs) to increase the PV hosting capacity of distribution feeders. The LV-DSTATCOMs absorb the reactive power to regulate the rising bus voltages resulting from excessive PV generation. Stochastic analysis framework is used to determine the PV hosting capacity while an iterative placement technique is used to place the LV-DSTATCOMs. Additionally, sensitivity analysis is carried out to provide insights on the optimal device size, number, and control settings. The results show that, the PV hosting capacity can be significantly increased by installing a few LV-DSTATCOMs a key locations for reactive power absorption. For the circuit used in this study, a set of 23 devices has increased the PV hosting capacity from 15% to 100% of the feeder's median day time peak load.

In chapter 7, an analytical approach is presented to estimate the PV and energy storage system (ESS) hosting capacities of distribution feeders based on overcurrrent protection as impact criterion. As the existing simulation-based estimation approaches require considerable time needing to develop detailed circuit models and numerous simulations to run, the proposed approach is useful in providing preliminary PV and ESS hosting capacity estimates without requiring to perform any simulations. Sympathetic tripping and relay insensitivity problems are considered in this chapter under both symmetrical and unsymmetrical fault conditions. Using the analysis presented, the factors influencing these protection problems are determined to provide insights into relay settings. The hosting capacities obtained using the proposed analytical approach are compared with those obtained using simulations of an actual distribution circuit model. The findings show that the proposed approach is accurate in estimating the feeder's PV and ESS hosting capacities.

In summary, this dissertation presents our key contributions as follows:

- Provided insights into the operational characteristics of edge-of-grid low-voltage UPFC and SVCs while proposing an effective algorithm for deploying them in distribution circuits.
- A multi-objective optimization formulation is proposed to determine the optimal locations of edge-of-grid SVCs operating on local controllers.
- A two-stage optimization framework based on AC optimal power flow is proposed for placement and centralized real-time control of edge-of-grid LV-SVCs to minimize energy losses while providing voltage regulation.
- A simplified procedure to tune the smart inverter control setting parameters of PVs present in the feeder neighborhoods experiencing voltage regulation problems is proposed.
- Proposed and examined the application of edge-of-grid LV-DSTATCOMs to mitigate the voltage rise due to PV generation, thereby increasing the distribution feeder's PV hosting capacity.
- An analytical approach is proposed to conservatively estimate the PV and ESS hosting capacity of distribution feeders based on overcurrent protection impact criteria while providing the insights into the overcurrent relay settings when high levels of PV and ESS are present.

Bibliography

[1] Roger C Dugan. Reference guide: The open distribution system simulator (opendss). *Electric Power Research Institute, Inc*, 7, 2012.

[2] M. Rylander, J. Smith, and W. Sunderman. Streamlined method for determining distribution system hosting capacity. *IEEE Transactions on Industry Applications*, 52(1):105–111, Jan 2016.

[3] *ANSI C84.1: American National Standard for Electric Power Systems and Equipment-Voltage Ratings (60 Hertz).* National Electrical Manufacturers Association, 2016.

[4] D. Divan, R. Moghe, and A. Prasai. Power electronics at the grid edge : The key to unlocking value from the smart grid. *IEEE Power Electronics Magazine*, 1(4):16–22, Dec 2014.

[5] H. V. Padullaparti, Q. Nguyen, and S. Santoso. Advances in volt-var control approaches in utility distribution systems. In *2016 IEEE Power & Energy Society General Meeting (PESGM)*, pages 1–5, July 2016.

[6] B. McMillan, P. Guido, O. Leitermann, V. Martinelli, A. Gonzaga, and R. McFetridge. Application of power electronics lv power regulators in a utility distribution system. In *2015 IEEE Rural Electric Power Conference*, pages 43–47, April 2015.

[7] SVC20: Low voltage pole-mounted 20 kVA static VAR compensator.

[8] Thomas Allen Short. *Electric power distribution handbook.* CRC press, 2014.

[9] A. Dubey, S. Santoso, and A. Maitra. Understanding photovoltaic hosting capacity of distribution circuits. In *IEEE Power & Energy Society General Meeting*, pages 1–5, July 2015.

[10] Dao Van Tu, S. Chaitusaney, and A. Yokoyama. Maximum-allowable distributed generation considering fault ride-through requirement and reach reduction of utility relay. *IEEE Transactions on Power Delivery*, 29(2):534–541, April 2014.

[11] John Seuss, Matthew J. Reno, Robert J. Broderick, and Santiago Grijalva. Maximum PV size limited by the impact to distribution protection. In *IEEE 42nd Photovoltaic Specialist Conference*, pages 1–6, 2015.

[12] Vince Scaini. Whitepaper: Grid support stability for reliable, renewable power, 2012.

[13] IEEE guide for conducting distribution impact studies for distributed resource interconnection. *IEEE Std 1547.7-2013*, pages 1–137, Feb 2014.

[14] H. Yazdanpanahi, Wilsun Xu, and Yun Wei Li. A novel fault current control scheme to reduce synchronous DG's impact on protection coordination. *IEEE Trans. on Power Delivery*, 29(2):542–551, April 2014.

[15] H. Yazdanpanahi and W. Xu. Contribution of induction-machine distributed generators to fault current and assessing their impact on overcurrent protection. In *26th Annual IEEE Canadian Conference on Electrical and Computer Engineering*, pages 1–4, May 2013.

[16] Surya Bhattacharya, Tapan Saha, and Md Jahangir Hossain. Fault current contribution from photovoltaic systems in residential power networks. In *IEEE Australasian Universities Power Engg Conf.*, pages 1–6, 2013.

[17] J Keller and B Kroposki. Understanding fault characteristics of inverter-based distributed energy resources. Technical report, National Renewable Energy Laboratory, January 2010.

[18] T.S. Sidhu and D. Bejmert. Short-circuit current contribution from large scale PV power plant in the context of distribution power system protection performance. In *IET Conference on Renewable Power Generation*, pages 1–6, Sept 2011.

[19] M. E. Baran and I. El-Markaby. Fault analysis on distribution feeders with distributed generators. *IEEE Transactions on Power Systems*, 20(4):1757–1764, 2005.

[20] H. V. Padullaparti, P. Chirapongsananurak, S. Santoso, and J. Taylor. Edge-of-grid voltage control: Device modeling, strategic placement, and application considerations. *IEEE Power and Energy Technology Systems Journal*, PP(99):1–1, 2017.

[21] H. V. Padullaparti, M. Lwin, and S. Santoso. Optimal placement of edge-of-grid low-voltage SVCs in real-world distribution circuits. In *IEEE Workshop on Power Electronics and Power Quality Applications (PEPQA)*, pages 1–6, May 2017.

[22] Rohit Moghe, Deepak Divan, Dexter Lewis, and Joe Schatz. Turning distribution feeders into STATCOMs. *IEEE Transactions on Industry Applications*, 53(2):1372–1380, 2017.

[23] D. Divan and P. Kandula. Distributed power electronics: An enabler for the future grid. *CPSS Transactions on Power Electronics and Applications*, 1(1):57–65, Dec 2016.

[24] Ramyar Rashed Mohassel, Alan Fung, Farah Mohammadi, and Kaamran Raahemifar. A survey on advanced metering infrastructure. *International Journal of Electrical Power & Energy Systems*, 63:473 – 484, 2014.

[25] H. R. Chi, K. F. Tsang, K. T. Chui, H. S. H. Chung, B. W. K. Ling, and L. L. Lai. Interference-mitigated zigbee-based advanced metering infrastructure. *IEEE Transactions on Industrial Informatics*, 12(2):672–684, April 2016.

[26] Z. Hu, S. Mohagheghi, and M. Sartipi. Efficient data acquisition in advanced metering infrastructure. In *2015 IEEE Power Energy Society General Meeting*, pages 1–5, July 2015.

[27] H. V. Padullaparti, Quan Nguyen, and S. Santoso. Optimal placement and dispatch of LV-SVCs to improve distribution circuit performance. *submitted to IEEE Transactions on Power Systems.*

[28] *Advanced Power Engineering.* Book chapter accepted in CRC Press, 2018.

[29] IEEE standard for interconnecting distributed resources with electric power systems - amendment 1. *IEEE Std 1547a-2014 (Amendment to IEEE Std 1547-2003)*, pages 1–16, May 2014.

[30] M. Rylander, Huijuan Li, J. Smith, and W. Sunderman. Default volt-var inverter settings to improve distribution system performance. In *2016 IEEE PES General Meeting*, pages 1–5, July 2016.

[31] H. V. Padullaparti, N. Ganta, and S. Santoso. Voltage regulation at grid edge: Tuning of PV smart inverter control. In *IEEE PES T&D Conference & Expo*, April 2018.

[32] IEEE draft standard for interconnection and interoperability of distributed energy resources with associated electric power systems interfaces. *IEEE P1547/D6.7.2, May 2017*, pages 1–116, Jan 2017.

[33] H. V. Padullaparti, Suma Jothibasu, S. Santoso, and G. Todeschini. Increasing feeder PV hosting capacity by regulating secondary circuit voltages. In *IEEE Power & Energy Society General Meeting*, August 2018.

[34] Barry Mather et al. Southern California Edison high-penetration photovoltaic project–year 1. Technical report, 2011.

[35] Anderson Hoke, Rebecca Butler Joshua Hambrick, and Benjamin Kroposki. Maximum photovoltaic penetration levels on typical distribution feeders. Technical report, 2012.

[36] H. V. Padullaparti, P. Chirapongsananurak, M. E. Hernandez, and S. Santoso. Analytical approach to estimate feeder accommodation limits based on protection criteria. *IEEE Access*, 4:4066–4081, 2016.

[37] A. A. Abou El-Ela, R. A. El-Sehiemy, A. M. Kinawy, and M. T. Mouwafi. Optimal capacitor placement in distribution systems for power loss reduction and voltage profile improvement. *IET Generation, Transmission Distribution*, 10(5):1209–1221, 2016.

[38] A. Askarzadeh. Capacitor placement in distribution systems for power loss reduction and voltage improvement: a new methodology. *IET Generation, Transmission Distribution*, 10(14):3631–3638, 2016.

[39] X. Su, M. A. S. Masoum, and P. J. Wolfs. PSO and improved BSFS based sequential comprehensive placement and real-time multi-objective control of delta-connected switched capacitors in unbalanced radial MV distribution networks. *IEEE Transactions on Power Systems*, 31(1):612–622, Jan 2016.

[40] B. McMillan, P. Guido, O. Leitermann, V. Martinelli, A. Gonzaga, and R. McFetridge. Application of power electronics LV power regulators in a utility distribution system. In *2015 IEEE Rural Electric Power Conference*, pages 43–47, April 2015.

[41] M. A. Tabrizi, M. Sahni, N. Prakash, V. Martinelli, and J. Simonelli. Utilization of low voltage in-line power regulator for reliable integration & performance of DER technologies. In *2015 IEEE Power Energy Society General Meeting*, pages 1–5, July 2015.

[42] Montengegro Davis. UPFC model documentation.

[43] D. Montenegro, J. Taylor, and R. Dugan. Open source unified power flow controller model for quasi-static time series simulation. In *2016 CIGRE international colloquium*, Nov 2016.

[44] P. Chirapongsananurak, N. Ganta, H. V. Padullaparti, S. Santoso, J. Taylor, M. Simms, and A. Vukojevic. Strategic placement of low voltage connected voltage regulation devices. In *2016 CIGRE international colloquium*, Nov 2016.

[45] H. Afaghzadeh, S. Sarkhani, H. Aghazadeh, and Y. Salami. Loss reduction and voltage improvement of Meshkinshahr distribution network with optimal capacitor placement using BPSO algorithm. In *2012 Proceedings of 17th Conference on Electrical Power Distribution*, pages 1–6, May 2012.

[46] John Seuss, Matthew J Reno, Robert J Broderick, and Santiago Grijalva. Analysis of PV advanced inverter functions and setpoints under time series simulation. Technical Report SAND2016-4856, Sandia National Laboratories, 2016.

[47] Matthew J Reno and Kyle Coogan. Grid integrated distributed PV (GridPV). *Sandia National Laboratories SAND2013-6733*, 2013.

[48] J. Kennedy and R. Eberhart. Particle swarm optimization. In *Neural Networks, 1995. Proceedings., IEEE International Conference on*, volume 4, pages 1942–1948 vol.4, Nov 1995.

[49] J. Kennedy and R. C. Eberhart. A discrete binary version of the particle swarm algorithm. In *1997 IEEE International Conference on Systems, Man, and Cybernetics. Computational Cybernetics and Simulation*, volume 5, pages 4104–4108 vol.5, Oct 1997.

[50] M. B. Liu, C. A. Canizares, and W. Huang. Reactive power and voltage control in distribution systems with limited switching operations. *IEEE Transactions on Power Systems*, 24(2):889–899, May 2009.

[51] Sanjay Mehrotra. On the implementation of a primal-dual interior point method. *SIAM Journal on Optimization*, 2(4):575–601, 1992.

[52] G. L. Torres and V. H. Quintana. An interior-point method for nonlinear optimal power flow using voltage rectangular coordinates. *IEEE Transactions on Power Systems*, 13(4), Nov 1998.

[53] Sultan S Alkaabi, HH Zeineldin, and Vinod Khadkikar. Short-term reactive power planning to minimize cost of energy losses considering PV systems. *IEEE Transactions on Smart Grid*, 2018.

[54] M Rylander, J Smith, and H Li. Determination of advanced inverter settings to improve distribution system performance. In *Solar Integration Workshop, Berlin, Germany*, 2014.

[55] William H Kersting. *Distribution system modeling and analysis*. CRC press, 2012.

[56] Alan Goodrich, Ted James, and Michael Woodhouse. Residential, commercial, and utilityscale photovoltaic (pv) system prices in the united states: current drivers and cost-reduction opportunities. *Contract*, 303(2012):275–3000, 2012.

[57] Joshua S Stein, Clifford W Hansen, and Matthew J Reno. The variability index: A new and novel metric for quantifying irradiance and PV output variability. In *World Renewable Energy Forum*, pages 13–17, 2012.

[58] B. Mather and R. Neal. Integrating high penetrations of PV into southern california: Year 2 project update. In *38th IEEE Photovoltaic Specialists Conference*, pages 000737–000741, June 2012.

[59] D. Narang and J. Hambrick. High penetration PV deployment in the arizona public service system. In *37th IEEE Photovoltaic Specialists Conference*, pages 002402–002405, June 2011.

[60] OpenDSS. [Accessed: Nov. 2, 2017].

[61] S. Jothibasu, S. Santoso, and A. Dubey. Determining PV hosting capacity without incurring grid integration cost. In *North American Power Symposium (NAPS)*, pages 1–5, Sept 2016.

[62] A. Dubey, S. Santoso, and A. Maitra. Understanding photovoltaic hosting capacity of distribution circuits. In *2015 IEEE Power Energy Society General Meeting*, pages 1–5, July 2015.

[63] California Solar Statistics. [Accessed: Nov. 2, 2017].

[64] IEEE standard for interconnecting distributed resources with electric power systems. *IEEE Std 1547-2003*, pages 1–28, July 2003.

[65] H. V. Padullaparti, P. Chirapongsananurak, M. E. Hernandez, and S. Santoso. Analytical approach to estimate feeder accommodation limits based on protection criteria. *IEEE Access*, 4:4066–4081, 2016.

Vita

Harsha Vardhana Padullaparti was born in Machilipatnam, Andhra Pradesh, India on April 10, 1986. He received the B.Tech. degree in Electrical & Electronics Engineering from Jawaharlal Nehru Technological University, Hyderabad, India, in 2007, and the M.S. (by Research) degree in Electrical Engineering from Indian Institute of Technology Madras, Chennai, India, in 2010. He was a Senior Engineer with Power Grid Corporation of India Limited, Kolkata, India, where he worked for five years. His research interests include power transmission and distribution, renewable energy integration, power system protection, and microgrids.

Permanent address: harshap@utexas.edu